# Reliability of Mooring Systems for Floating Production Systems

by

Young Jae Choi and Prof. Robert B. Gilbert
The University of Texas at Austin

Yu Ding and Prof. Jun Zhang
Texas A&M University

**Final Project Report Prepared for**
**Minerals Management Service**
**Under the MMS/OTRC Cooperative Research Agreement**
**1435-01-99-CA-31003**
**Task Order 18203**
**1435-01-04-CA-35515**
**Task Order 35990**
**MMS Project Number 423**

**and**

**OTRC Industry Consortium**

**April, 2006**

OTRC Library Number: 1/06C166

*For more information contact:*

**Offshore Technology Research Center**
Texas A&M University
1200 Mariner Drive
College Station, Texas 77845-3400
(979) 845-6000

or

**Offshore Technology Research Center**
The University of Texas at Austin
1 University Station C3700
Austin, Texas 78712-0318
(512) 471-6989

*A National Science Foundation Graduated Engineering Research Center*

# TABLE OF CONTENTS

# LIST OF TABLES AND FIGURES

## Tables

## Figures

## Executive Summary

Mooring systems for floating production systems are currently designed on the basis of individual components (lines and anchors). A spar design originally developed by an industry consortium was chosen as the study spar. The mooring system was designed for three different water depths: 3,000, 6,000 and 10,000 feet. A numerical model was employed to compute global motions and tensions in the mooring lines given met-ocean conditions. Component and system reliability analyses were conducted using representative probabilistic descriptions of the extreme met-ocean conditions (hurricanes and loop currents) in the Gulf of Mexico.

Based on a detailed analysis of component and system reliability for spar mooring systems in water depths from 3,000 to 10,000 feet, the following major conclusions have been drawn:

1. Existing design guidelines provide for levels of system and component reliability against extreme loading that are above typical target levels that have been proposed by industry.
2. Levels of reliability between mooring lines and anchors are not necessarily consistent; anchors have failure probabilities that are more than an order of magnitude smaller than those for lines under extreme loading.
3. Mooring systems exhibit redundancy in that failure of the most heavily-loaded component during an extreme event does not necessarily lead to failure of the system. The redundancy is greater for the taut versus semi-taut systems and is greater during loop current events versus hurricane events.
4. The reliability for the taut systems is higher than that for the semi-taut system due to the relatively small contribution of environmental loading versus pre-tension for the taut systems.
5. The reliability for a design that is governed by loop current events is greater than one that is governed by hurricane events due to smaller uncertainty in the environmental loading conditions during loop currents compared to hurricanes.

Although this project is based on the analysis of the mooring system for a specific spar design and design environment, the procedures for reliability analyses produced in this project and the major conclusions are intended to provide general tools and guidance that will be useful for the design of mooring systems for floating production systems in deep water.

# Reliability of Mooring Systems for Floating Production Systems

## 1. Introduction

Mooring systems for floating production systems, consisting of individual mooring lines and anchors, are currently designed on the basis of individual components. The most heavily loaded line and anchor are checked under extreme loading conditions (hurricane and loop current) with the system of lines intact and with one line removed. However, the performance of the floating production system depends more directly on the performance of the system of lines and anchors rather than on the performance of a single line or anchor. The objective of this project was to assess and study the component and system reliabilities for the mooring system of a spar that is representative of existing practical technology in the Gulf of Mexico.

A spar design originally developed by the industry consortium, DeepStar, was chosen as the study spar. The mooring system was designed for these different water depths: 3,000, 6,000 and 10,000 feet. It is a classic spar with steel mooring lines in 3,000 feet of water and polyester mooring lines in deeper depths.

The hurricane and loop current environments used in this study were also developed by DeepStar as a basis for research studies deepwater structures, moorings, and risers (e.g., see papers OTC 16582 and 16583). They represented a consensus view of simple but realistic criteria that would be useful for research and engineering studies, but were not intended to be a basis for individual, actual designs. These wind and wave criteria were similar to that in API RP2A, and the loop current criteria were based on an industry consensus of data available at the time.

A numerical model was employed to compute global motions and tensions in the mooring lines given met-ocean conditions. The computation was performed in two coupled steps; the first step was to compute loads on the hull due to waves, currents and winds; the second step was to compute the loads and dynamics of the mooring/tendon/riser system. These two independent steps are coupled together by matching the forces and displacements of a mooring/tendon/riser system and the hull at their joints following prescribed connection conditions. The code for computing dynamics of the mooring/tendon/riser system is based on a slender-body assumption and employs a nonlinear Finite Element Method (FEM). For this study, the original code was extended to accommodate for large elongations in polyester lines and to model the scenario where an anchor pulls out and the line remains intact.

The reliability analyses were conducted using representative probabilistic descriptions of the extreme met-ocean conditions (hurricanes and loop currents) in the Gulf of Mexico. Probabilities of failure during a 20-year design life were calculated for individual components and for the mooring system. A simplified semi-analytical method was used to calculate failure probability. The advantages of this method, particularly in comparison to Monte Carlo simulation, are that it is efficient and general in that relationships between input and output are expressed directly in mathematical equations and graphical depictions. A system failure is the failure of two or more lines. A line (or leg) failure includes line component failures (chains, polyester or wire line, connectors, and anchors) plus, in the case of the second line, overload due to failure of the first line.

## 2. Description of Study Spar and Mooring System

The main characteristics of the hull are given in Table 2.1. The mooring systems deployed in all water depths consist of fourteen spread mooring lines as depicted in Figure 2.1. The differences between the three mooring systems are mainly the length and material of mooring lines. The mooring lines in 3,000 ft water are the traditional combination of steel chain-wire-chain, while those in 6,000 and 10,000 ft water are the integration of steel chain-polyester rope-steel chain. Their characteristics are given in Table 2.2.

**Table 2.1**. Hull specification.

| | |
|---|---|
| Displacement | 53600 metric ton |
| Total displacement | 220640 metric ton |
| Diameter | 122 ft |
| Length | 705 ft |
| Draft | 650 ft |
| Hard tank depth | 220 ft |
| KB | 540 ft |
| KG | 462 ft |
| KG (based on total displacement) | 314 ft |
| Radius of gyration | Pitch=221ft, yaw=28.5 ft |
| Drag force coefficient | 1.16 |
| Wind force coefficient | 0.0558 (kips/(ft/sec)$^2$) |
| Center of pressure | 722 ft ABL |

**Table 2.2**. Mooring system specifications.

| Water depth | 3000 ft | 6000 ft | 10000 ft |
|---|---|---|---|
| Mooring type | Steel semi taut | Poly taut | Poly taut |
| Mooring pattern | 14 point taut-leg omni-directional spread | 14 point taut-leg omni-directional spread | 14 point taut-leg omni-directional spread |
| Mooring line composition | Platform section 250’x5-1/4” K4 Studless chain | Platform section 300’x4.625” K4 Studless chain | Platform section 300’x5-1/8” K4 Studless chain |
| | Riser section 3,200’x5-3/8” Sheathed Wire | Middle section 7,800’x8.27” Polyester | Middle section 13,300’x9.06” Polyester |
| | Ground section 1150’x5-1/4” K4 Studless chain | Ground section 400’x4.625” K4 Studless chain | Ground section 400’x5-1/8” K4 Studless chain |
| Fairlead location | 300 ft ABL | 300 ft ABL | 300 ft ABL |
| Pretension | 680 kips | 530 kips | 650 kips |

Table 2.3. Design information for Hurricane and current dominant conditions

| | Hurricane Dominant | Current Dominant |
|---|---|---|
| Significant wave height ($H_s$) | 40 ft | 20 ft |
| Peak spectral period ($T_p$) | 14 sec | 11 sec |
| Wave spectra | Jonswap ( $\gamma = 2.5$) | Jonswap ( $\gamma = 2$) |
| Wave direction | 270˚ (West) | 90˚ L of Loop current |
| Current direction | 30˚ R of waves | 90˚ (East) |
| Wind direction | 30˚ L of waves | collinear with waves |
| Wind speed (1-hr) | 92 mph @10m | 50 mph @10m |
| Wind spectra | refer to API RP 2A-WSD, paragraph 2.3.2b | |
| Wind profile | refer to API RP 2A-WSD, paragraph 2.3.2b | |
| Storm surge & tide | 0 ft | 0 ft |
| Current speed (below surface) | | |
| 0 | 3.5 ft/sec | 7.0 ft/sec |
| 200 ft | 3.5 ft/sec | 7.0 ft/sec |
| 300 ft | 0.3 ft/sec | 7.0 ft/sec |
| 800 ft | 0.3 ft/sec | 3.0 ft/sec |
| Seabed | 0.3 ft/sec | 0 ft/sec |

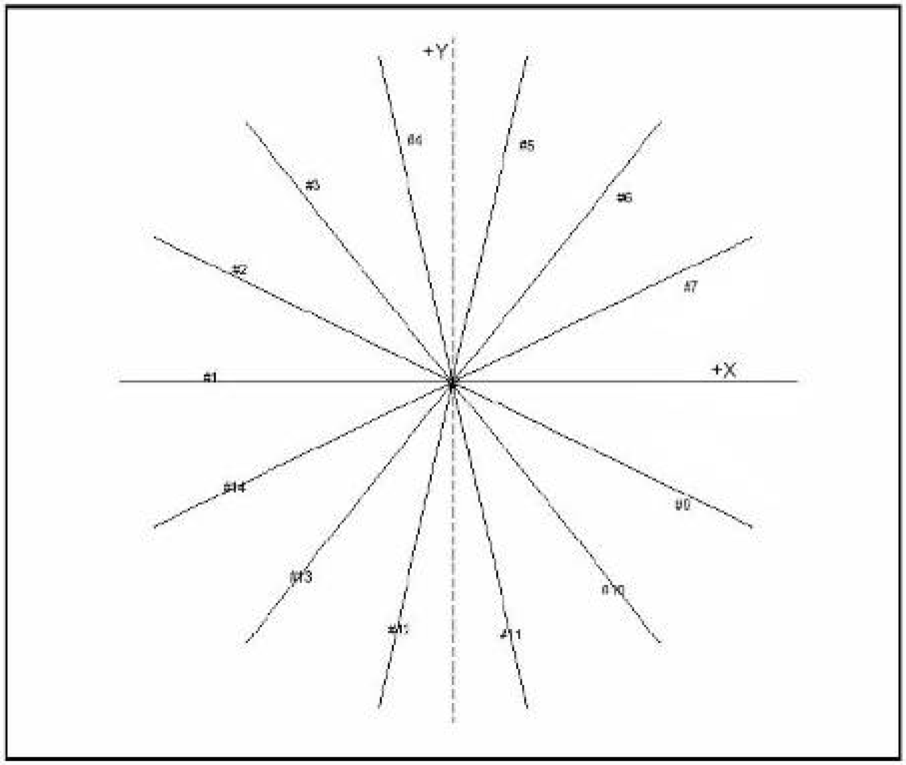

**Figure 2.1**: Spread mooring system

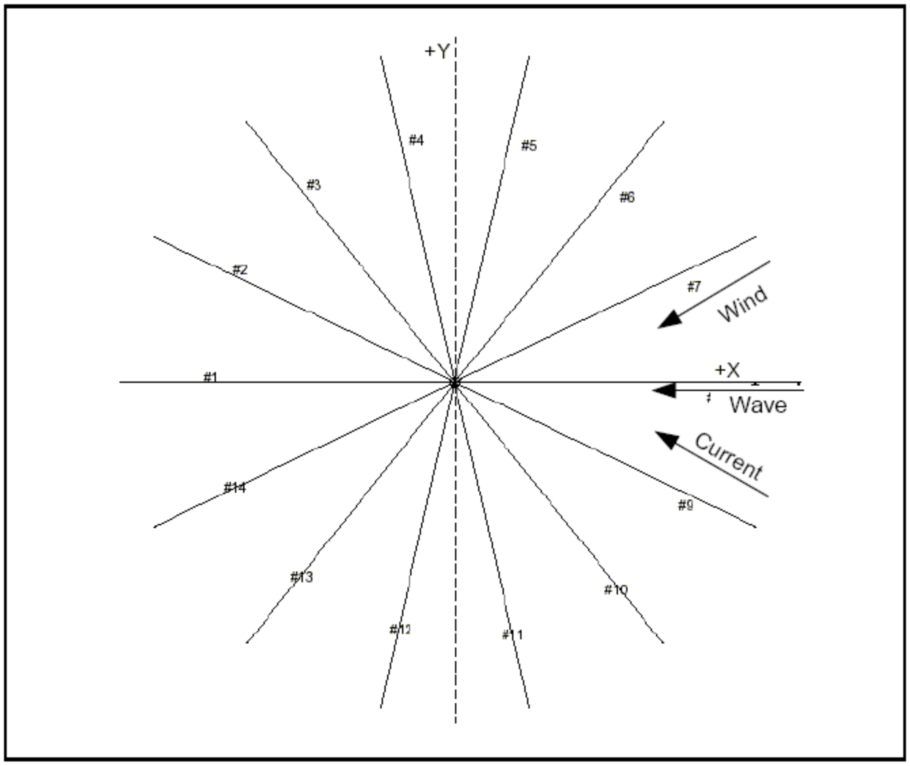

**Figure 2.2**: Relative directions among a loop current, wave and wind under a loop current condition

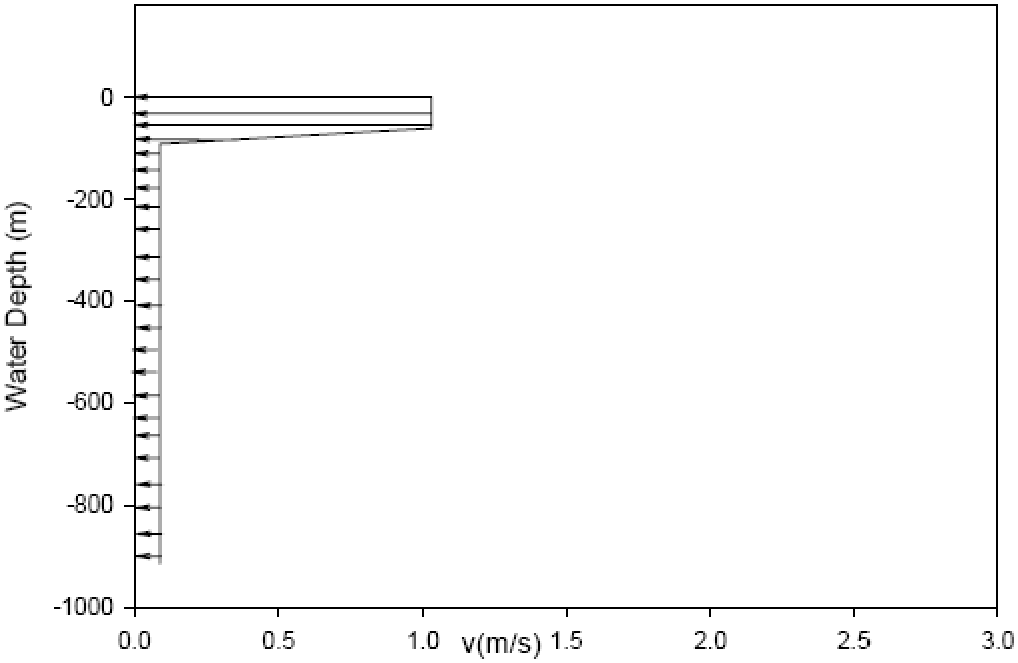

**Figure 2.3:** The profile of current velocity during a hurricane

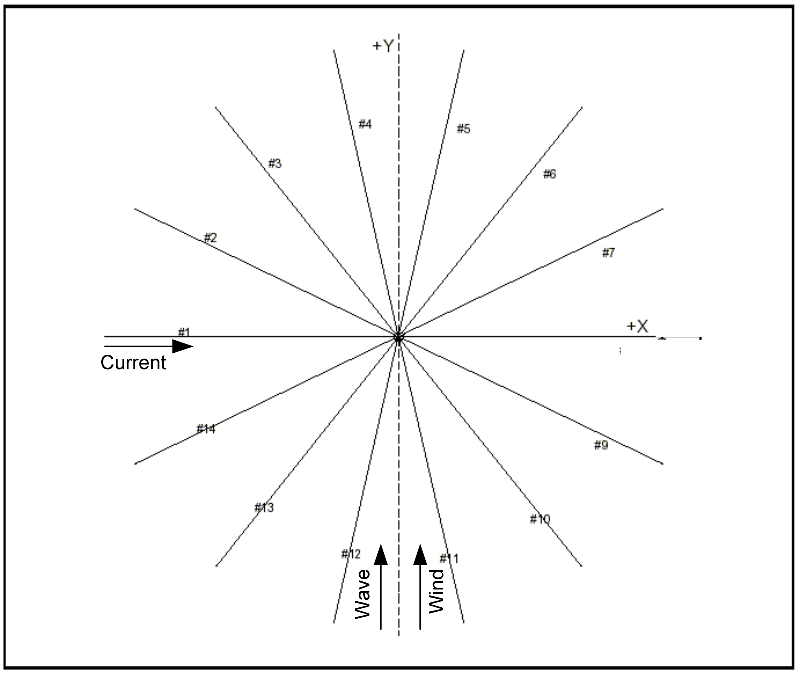

**Figure 2.4**: Relative directions among a loop current, wave and wind under a loop current condition

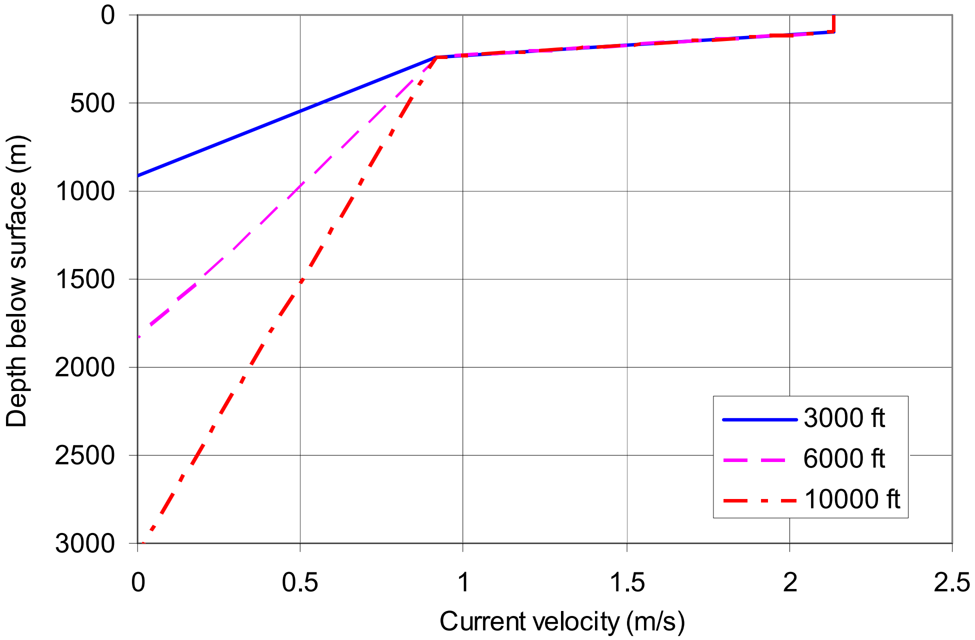

**Figure 2.5:** The profile of current velocity during a loop current

## 3. Coupled Analysis for the Interaction between a Floating Structure (Hull) and Its Mooring System: COUPLE

A numerical code developed recently, known as COUPLE (Ding et al. 2003), is especially effective and relatively simple in predicting dynamic interactions between a spar and its mooring/riser systems. Initially, it was developed for computing the 3-DOF (Degree-Of-Freedom) motions of a spar positioned by taut mooring lines using a quasi-static analysis (Cao and Zhang 1997) and later extended to allow for dynamical interaction between a spar and its mooring system to quantify the damping effects of a mooring system on the slow-drift motion of a spar (Chen et. al. 2001). More recently, it was extended to allow for 6-DOF motions of a moored floating structure.

COUPLE consists of two basic computational parts: one for computing the dynamics of a mooring/tendon/riser system and the other for the wave/current/wind loads on a moored floating structure (hull). The two independent codes are coupled by matching the forces and displacements of a mooring/tendon/riser system and the hull at their joints following prescribed connection conditions. The code for computing dynamics of the mooring/riser system is based on a slender-body assumption and employs a nonlinear Finite Element Method (FEM), known as CABLE3D (Ma and Webster, 1994). The computation in the original CABLE3D assumes infinitesimal elongation of a slender rod. Because large elongation slender components, such as springs and polyester ropes are often, respectively, used in a model test and a prototype mooring system, CABLE3D was extended to allow for large elongation in a mooring line to achieve accurate simulation (Chen et al. 2002). The computation of nonlinear wave forces on a floating structure is accomplished by using either a second-order diffraction wave theory (such as WAMIT) and/or the Morison Equation. In the case of a spar, the diameter of its hull is much smaller than the typical incident wavelength and hence both potential and drag wave loads on the spar are computed using the Morison equation.

### 3.1 Wave, current and wind loads on hull

The total met-ocean environmental loads on an offshore structure can be divided into three major parts according to their origins which are denoted by the subscripts.

$$\mathbf{F} = \mathbf{F}_{Wave} + \mathbf{F}_{Current} + \mathbf{F}_{Wind}$$

The hull of a classical spar or the upper portion of a truss spar is virtually a cylinder. In using the Morison equation to compute wave and current loads, the normal force per unit length on a cylinder of uniform diameter D is given by,

$$\begin{aligned} d\mathbf{F}_n &= (1+C_m)\rho_f \frac{\pi}{4} D^2 (\mathbf{a}_f)_n - C_m \rho_f \frac{\pi}{4} D^2 \mathbf{a}_n \\ &+ \frac{1}{2}\rho_f C_D D \left|(\mathbf{v}_f)_n - \mathbf{v}_n\right| \left[(\mathbf{v}_f)_n - \mathbf{v}_n\right], \end{aligned} \tag{3.1}$$

where $C_m$ is the added mass coefficient, $C_D$ the drag coefficient, $\rho_f$ the density of water, $\mathbf{v}_f$ and $\mathbf{a}_f$ water particle velocity and acceleration, and $\mathbf{v}$ and $\mathbf{a}$ the velocity and acceleration of the cylinder. The subscript 'n' denotes the component of the related vector in the direction normal to the axis of the cylinder. Water particle velocity and acceleration are the superposition of those of currents and waves. In the presence of ocean currents, wave frequencies may be shifted due to the Doppler Effect, which is neglected in our computation because it is assumed that current velocity is small in comparison with the phase velocity of incident waves.

Forces applied on the truncated bottom of a cylinder in the axial direction include the integration of wave pressure over the bottom, $S_B$, and drag and added-mass forces which are equivalent to an half of a thin circular disk of the same diameter of the cylinder in heave motion (Sarpkaya and Isaacson, 1981).

$$\begin{aligned} F_t &= \rho_f \iint_{s_B} \left( \frac{\partial(\phi^{(1)} + \phi^{(2)})}{\partial t} + \frac{1}{2} \left| \nabla \phi^{(1)} \right|^2 \right) ds \\ &+ C_{mt} \rho_f \frac{4}{3} \left( \frac{D}{2} \right)^3 \left[ (a_f)_t - a_t \right] \\ &+ \frac{1}{2} \rho_f C_{Dt} \frac{\pi D^2}{4} \left| (v_f)_t - v_t \right| \left[ (v_f)_t - v_t \right] \end{aligned} \tag{3.2}$$

where $\phi^{(1)}$ and $\phi^{(2)}$ are first- and second-order potential of incident waves, and $C_{mt}$ and $C_{Dt}$ are the added-mass and drag coefficient of the truncated cylinder bottom, respectively. $(v_f)_t - v_t$ and $(a_f)_t - a_t$ are the relative velocity and acceleration of the cylinder bottom to ambient fluid in the axial direction, respectively. Wave kinematics and first- and second-order incident wave potential used in the above equations are computed using a nonlinear Hybrid Wave Model (HWM) (Zhang et al., 1996).

In order to account for Vortex Induced Motion (VIM) of a spar in the presence of strong currents, such as loop currents in the Gulf of Mexico, an additional term representing the lifting force (or transverse force) applied on per unit length on the cylinder is added into the Morison equation.

$$d\mathbf{F}_l = \frac{1}{2} \rho_f C_L D v_c^2 \cos(2\pi f \cdot t) \vec{e}_t \times \vec{e}_c, \tag{3.3}$$

where $\vec{e}_c$ and $\vec{e}_t$ are the unit vectors in the current direction and the axial direction, respectively, $C_L$ the lifting coefficient, and $f$ the vortex shedding frequency. It is related to the Strouhal Number, $S_o$, defined by,

$$S_0 = \frac{fD}{v_n}. \tag{3.4}$$

The Strouhal number and lifting coefficient in the context of a spar equipped with helical strakes on its surface and constrained by its mooring/riser systems are not well documented. In our computation, they were calibrated by fitting the mean, and the average 1/3rd and 1/5th amplitude and period of the simulated and measured LF sway of a spar model. In the case of the study spar, the fitting yields $S_o = 0.25$ and $C_L = 0.45$. The procedure for determining the lifting coefficient is illustrated in Figure 3.1.

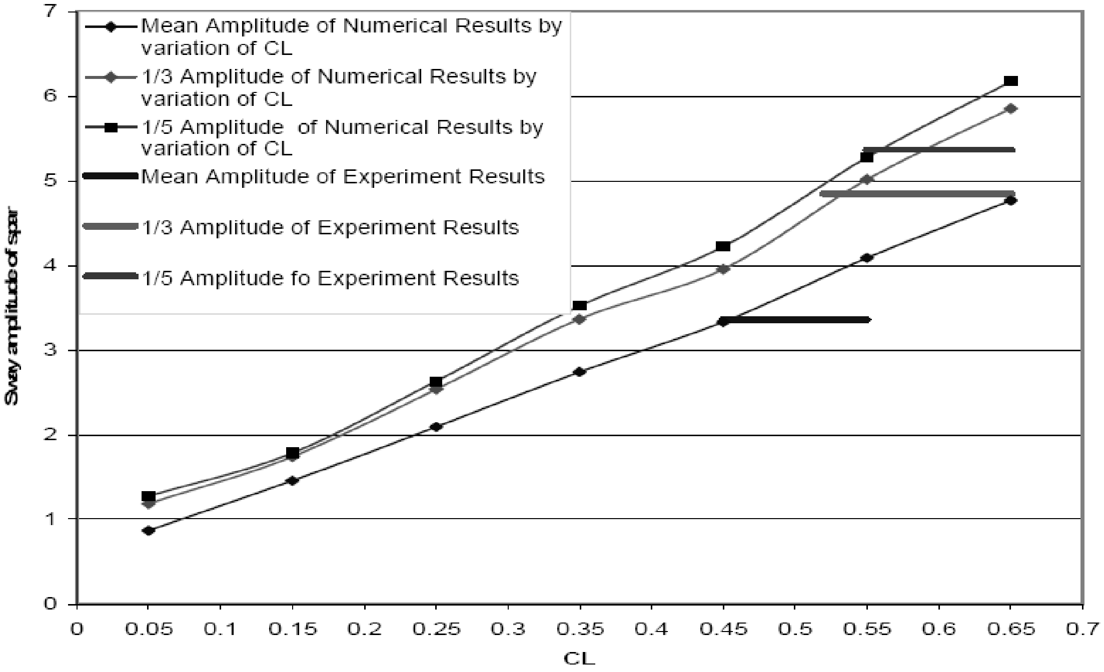

**Figure 3.1**: The value of $C_L$ vs. sway amplitude

Considering that the diameter of a spar, the velocities of currents and waves may change along its axis, the total wave and current loads on the spar are computed through the numerical integration of the corresponding loads over a number of segments along its longitudinal axis.

The computation of wind force is based on the empirical formula recommended by API (RP-2A),

$$F_{wind} = \frac{1}{2} C_s \rho_a V_a^2 A \tag{3.5}$$

where $\rho_a$ is the density of air, $C_s$ the shape coefficient depending on the shape of superstructure of a spar and wind direction, $V_a$, the total wind velocity and $A$ the projected area of a spar above the sea level. The shape coefficient and the location of center of wind pressure were determined based on the corresponding wind-tunnel tests, which were provided by the Deepstar project.

### 3.2 Dynamic equations for the hull

The equations of linear motion of a rigid body expressed in the $\hat{o}\hat{x}\hat{y}\hat{z}$ (fixed in space) coordinates and its rotational motion in the *oxyz* (fixed on the hull) coordinates are:

$$m\frac{d^2\boldsymbol{\xi}}{dt^2} + m\mathbf{T}^t(\frac{d\boldsymbol{\omega}}{dt}\times\mathbf{r}_g) + m\mathbf{T}^t(\boldsymbol{\omega}\times(\boldsymbol{\omega}\times\mathbf{r}_g)) = \mathbf{F}_t \ , \tag{3.6}$$

$$\mathbf{I}_o\frac{d\boldsymbol{\omega}}{dt} + \boldsymbol{\omega}\times\mathbf{I}_o\boldsymbol{\omega} + m\mathbf{r}_g\times(\mathbf{T}\frac{d^2\boldsymbol{\xi}}{dt^2}) = \mathbf{M}_o, \tag{3.7}$$

where $\boldsymbol{\xi} = (\xi_1, \xi_2, \xi_3)^t$ is the coordinates of the origin of the *oxyz* in the $\hat{o}\hat{x}\hat{y}\hat{z}$ coordinates and $\frac{d^2\boldsymbol{\xi}}{dt^2}$ is its acceleration. $\boldsymbol{\omega} = (\omega_1, \omega_2, \omega_3)^t$ is the angular velocity of the hull, $\mathbf{r}_g = (x_g, y_g, z_g)^t$, the vector from the origin of the *oxyz* coordinates to the gravitational center of the hull, and $\mathbf{I}_o$ the moment of inertia of the hull defined in the *oxyz* coordinates. $\mathbf{F}_t$ is the total force applied on the hull and expressed in the $\hat{o}\hat{x}\hat{y}\hat{z}$ coordinates, which includes wave, wind, current loads, hydrostatic restoring force, and restraining force from mooring lines and risers. $\mathbf{M}_o$ is the total moment and expressed in the *oxyz* coordinates. **T** is a transfer matrix between the hull-fixed coordinates (*oxyz*) and the space-fixed coordinates ($\hat{o}\hat{x}\hat{y}\hat{z}$). It is an orthogonal matrix with the property that $\mathbf{T}^t=\mathbf{T}^{-1}$.

### 3.3 Dynamics of a flexible slender rod with relatively large elongation

Our computation of the motion and tension of a flexible slender rod (mooring lines or risers) mainly follows Garrett (1982). To allow for large extension elements, such as springs or polyester ropes, Chen et al. (2002) extended his formulation, which is briefly described below. The instantaneous configuration of a rod is denoted by a vector, $\mathbf{r}(s,t)$, a function of time and the arc length along the rod. The dynamic and constrain equations of a rod of infinitesimal extension were given by

$$-(B\mathbf{r}'')'' + (\lambda\mathbf{r}')' + \mathbf{q} = \rho\ddot{\mathbf{r}}, \quad \lambda = T - Bk^2, \tag{3.8}$$

$$\mathbf{r}'\cdot\mathbf{r}' = (1+\varepsilon)^2, \tag{3.9}$$

where $B$ is the bending stiffness, $T$ the tension and $k$ the curvature of the rod. **q** is the external force applied on the rod per unit length and $\rho$ the mass per unit length. The prime and overhead dots stand for the partial derivatives with respect to $s$ and time, respectively. $\varepsilon$ denotes the strain of the rod, which is equal to $T/EA$ where $E$ is the

Young's modulus and $A$ the cross section area of the rod. It is noted that the strain of the rod is explicitly considered in (3.9) but not consistently dealt with in (3.8). For the elements in a mooring line with large extension, such as a spring or polyester rope, their bending stiffness is small and can be neglected for simplicity. Dropping the term involving the bending stiffness, the equation corresponding to Equation (3.8) is derived, which considers relative large elongation ($\varepsilon$).

$$\left(\frac{\lambda}{1+\varepsilon}\mathbf{r}'\right)' + \mathbf{q}(1+\varepsilon) = \rho\ddot{\mathbf{r}}. \tag{3.10}$$

In using a finite element method to solve the above equations, the shape and tension of each element are, respectively, approximated by a cubic and quadratic Spline function. A Newton method is used to solve static equations and a Newmark-$\beta$ method used to solve dynamic equations in the time domain (Chen 2002).

Because the modulus of a polyester rope depends on the tension, empirical formula given by Del Vecchio (1992) is employed.

$$E = \alpha + \beta L_m - \gamma L_a - \delta Log(T), \tag{3.11}$$

where $\alpha$, $\beta$, $\gamma$ and $\delta$ are constants, related to the main characteristics of a polyester rope. $L_m$ is the mean tension, and $L_a$ and $T$ are the amplitude and period of dynamic tension, respectively. In COUPLE, $\delta$ is set to zero because the dependence of the modulus on the period of a dynamic load is insignificant (Bosman and Hooker 1999).

Even at the mean position of a spar experiencing steady wind, current and wave loads, the modulus of polyester ropes in different mooring lines of an integrated mooring system is different because of different mean tensions. To determine the modulus of each mooring line, we first let $L_a = 0$ and calculate the modulus and tension of each polyester rope through iteration. Our calculations indicates that the mean (static) tension and modulus of each mooring line converge rapidly just after two to three iterations. Based on the updated modulus of each rope, the simulation of the motion of a moored spar and the tension in mooring lines is made given the met-ocean conditions. Since the dominant responses of a spar are its Low Frequency (LF) motions, the amplitude of dynamic tension in a polyester mooring line is also dominated by the corresponding LF tension. Using a low-pass filter, the average amplitude of dynamic tension in a polyester rope can be determined as sketched in Figure 3.2. Knowing the approximate $L_a$, the modulus of each polyester line is updated and the dynamic simulation of a spar positioned by an integrated polyester mooring system is repeated. The iteration terminates if the relative difference in the modulus of two consecutive iterations is smaller than a prescribed error tolerance. More detailed description of the iterative procedure for determining the modulus of polyester mooring lines was given by Kim et al. (2003).

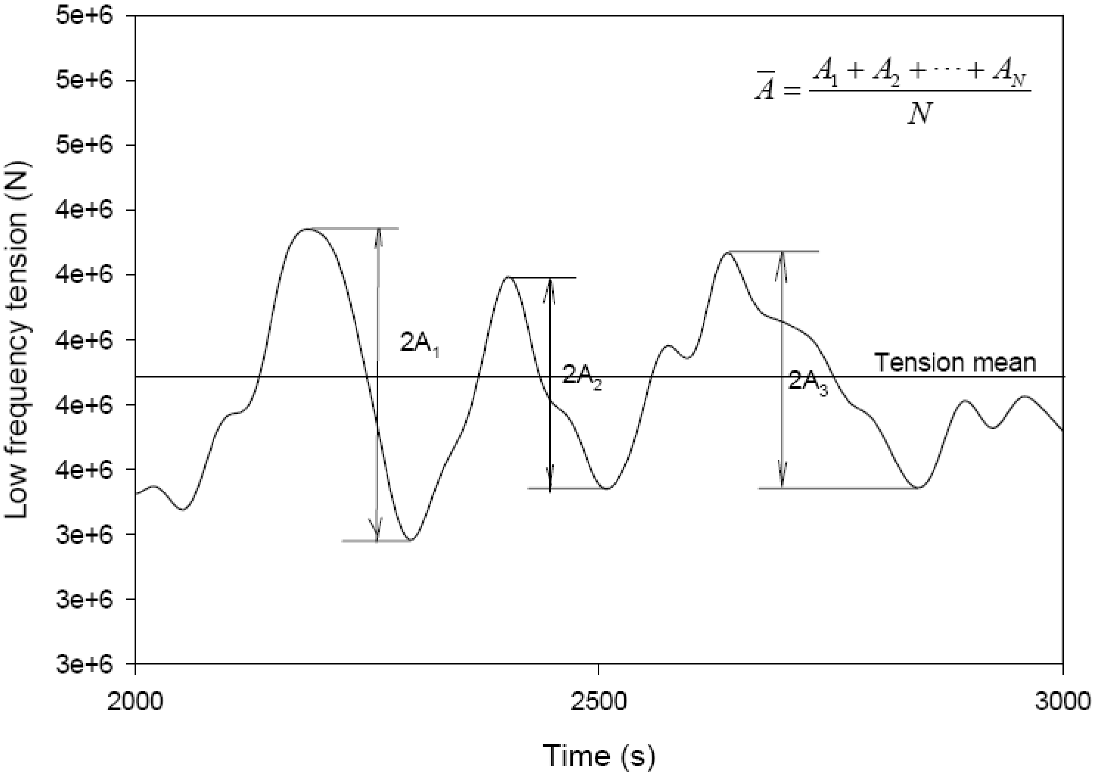

**Figure 3.2**: Sketch for computing the average amplitude of dynamic tension

### 3.4 Coupling between a hull and its mooring/riser systems

Dynamic equations for a hull and its mooring and riser systems are coupled by imposing prescribed conditions at their connections (fairleads or porches). For example, if a hinge connection is imposed between the hull and its mooring lines, then the forces and displacements of the hull and a mooring line at its fairlead are the same and no moment is applied there. More complicated connection conditions can be simulated by appropriately imposing force, moment, and relative displacement on the hull and its mooring/riser systems at their connections. The coupled equations for the hull and its mooring and riser systems are then solved simultaneously in the time domain using a Newmark-$\beta$ method. At each time step, the velocities and positions of the hull and all mooring lines/risers are first predicted based on the velocities, positions and accelerations at previous step. Then the correctors for positions, velocities and accelerations are calculated based upon the dynamic equations. If the difference between the two correctors of consecutive iterations is less than a prescribed error tolerance, the simulation moves forward to the next step. Details of the related numerical procedures were given by Chen (2002).

## 4. Numerical Simulation of Met-Ocean Conditions

The numerical simulation of met-ocean conditions was aimed at representing two different types of extreme events in the Gulf of Mexico: hurricanes (storms) and loop currents. Conventional practice for deepwater mooring systems deployed in the Gulf of Mexico is to design them to be able to accommodate the impact of a 100-year hurricane or/and loop current.

The occurrence of a significant storm near the location of the spar during its 20-year life span is modeled by a joint probability distribution of significant wave height ($H_s$) and peak period ($T_P$). The magnitude of velocities of related wind and current induced by the storm is assumed to be a function of $H_S$. However, for simplicity it is assumed that the relative directions of wave, wind and current in all simulated events remain the same, as depicted in Figures 2.2 or 2.4.

In using COUPLE to simulate incident waves, the input can be either measured wave elevation or a free (linear) wave spectrum. For the comparison of simulated motion and forces of a floating structure with the corresponding measurements in the field or laboratories, measured wave elevations are often used as the input. The amplitude and initial phase of free waves in a measured irregular long-crested wave train are calculated as a function of frequency using the decomposition part of a HWM. The amplitude and initial phase of free waves are then used in the prediction part of the same HWM for computing wave kinematics along the longitudinal axis of a spar as a function of time (Zhang et. al. 1996, Cao and Zhang 1997). In the absence of measured waves, a typical wave spectrum, such as a JONSWAP spectrum with a prescribed $H_s$ and $T_P$, is used as the input. The related free wave spectrum is obtained by match its resultant spectrum (including bound waves) with a given analytic wave spectrum selected for the simulation. The initial phases of free waves (and their amplitude) are obtained using a random phase method or random Fourier Coefficient method (Tuah and Hudspeth 1982) based on a free-wave amplitude or energy spectrum. In this study, random long-crested waves were generated according to JONSWAP spectra.

Given one-hour average wind velocity, the gustiness of wind is simulated based on a spectral energy density recommended by API (RP-2A).

$$\frac{fS(f)}{\sigma^2(z)} = \frac{f / f_\rho}{(1 + 1.5 f / f_\rho)^{5/3}} \ , \tag{4.1}$$

where $S(f)$ is the spectral energy density, $z_a$ the vertical coordinate of the wind pressure center of a floating structure, $f$ the frequency, $\sigma(z)$ the standard deviation of wind speed. The values of $\sigma(z)$ and $f_\rho$ depends on the average wind velocity and the vertical coordinate of wind pressure center level, which were described in API (RP-2A) and omitted here for brevity. Based on a wind spectral density function, the total wind velocity is calculated following the procedures similar to those for simulating random water waves.

In the current version of COUPLE, both magnitude and direction of current velocity are the input and assumed to be steady. The magnitude of current velocity decays with the increase in depth. However, the extension to allow for unsteady currents can be made without principle difficulties. The decay of the current velocity with the increase in water depth is depicted in Figures 2.3 and 2.5.

## 5. Motions of the Spar and Tensions in Mooring Lines

The added-mass, drag and lifting coefficients of the hull and Strouhal number are summarized in Table 5.1. These coefficients were used in the Morison equation for computing wave and current loads on the hull. Also included in Table 5.1 are the added-mass and drag coefficients of steel chains and polyester ropes used in integrated mooring lines. In the case of the spar design with a steel mooring system in 3,000 ft water, the predictions given by COUPLE were compared with the corresponding measurements of model tests, and satisfactory agreement was observed (Ding et al. 2003). For each set of met-ocean conditions representing a scenario of certain percentile of the occurrence of a hurricane or a loop-current event in the Gulf of Mexico, a three-hour numerical simulation was conducted using COUPLE. The results of the simulation are the global motions of the hull and the profile and tension of each individual mooring line. As an example, the simulated results of the spar in 3,000 ft water under the impact of a hurricane (*Hs*=12m, *Tp*=14s) are described below.

**Table 5.1**. Hydrodynamic force coefficients

| | Normal drag coefficient | Added-mass Coef. | Viv Lifting force Coef | Strouhal number |
|---|---|---|---|---|
| Spar | 1.16 | 1.00 | 0.45 | 0.2 |
| Chain | 2.45 | 1.40 | N/A | N/A |
| Rope | 1.20 | 1.00 | N/A | N/A |

The numerical results were examined against the corresponding laboratory measurements and satisfactory consistency between them was observed (Chen et al. 2001, Chen et al. 2006). In this project, COUPLE is used to simulate the global motions of a classical spar and tensions of its mooring lines deployed in 3,000, 6,000 and 10,000 ft water, respectively. The characteristics of the spar studied here are virtually the same as those of the DeepStar spar. The static offset curves of three mooring systems are respectively plotted in Figures 5.1a, 5.1b and 5.1c. To demonstrating the necessity of using the extended CABLE3D based on the large elongation formulation, also plotted in the figures is the corresponding curve computed using the similar code but based on the small elongation assumption. It is observed in Figure 5.1a that the difference between the two offset curves of the steel mooring system deployed in 3,000 ft water is insignificant, which is expected because of relatively small elongation of steel chains and wires. However, the difference between the related offset curves of the integrated polyester mooring system is significant as observed in both Figures 5.1b and 5.1c, and the difference is larger in the case of the mooring system deployed in 10,000 ft water. This is mainly because the deeper water depth results in a longer polyester rope in an integrated mooring line. Near the mean position (~ 17.5m) of the spar experiencing a 100-year hurricane in the Gulf of Mexico, Figure 5.1c shows that the restraining force of the mooring system is reduced by 16 to 20 % when the elongation is accounted for in the polyester ropes.

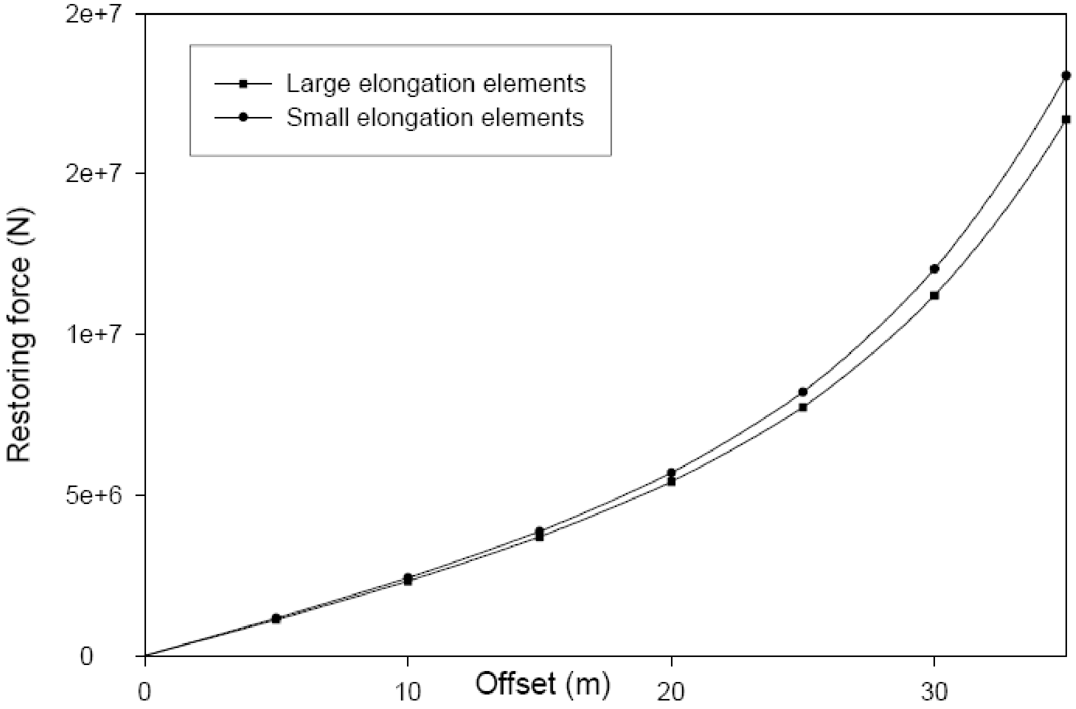

**Figure 5.1a:** Comparison of related static offset curves (water depth 3,000ft, steel)

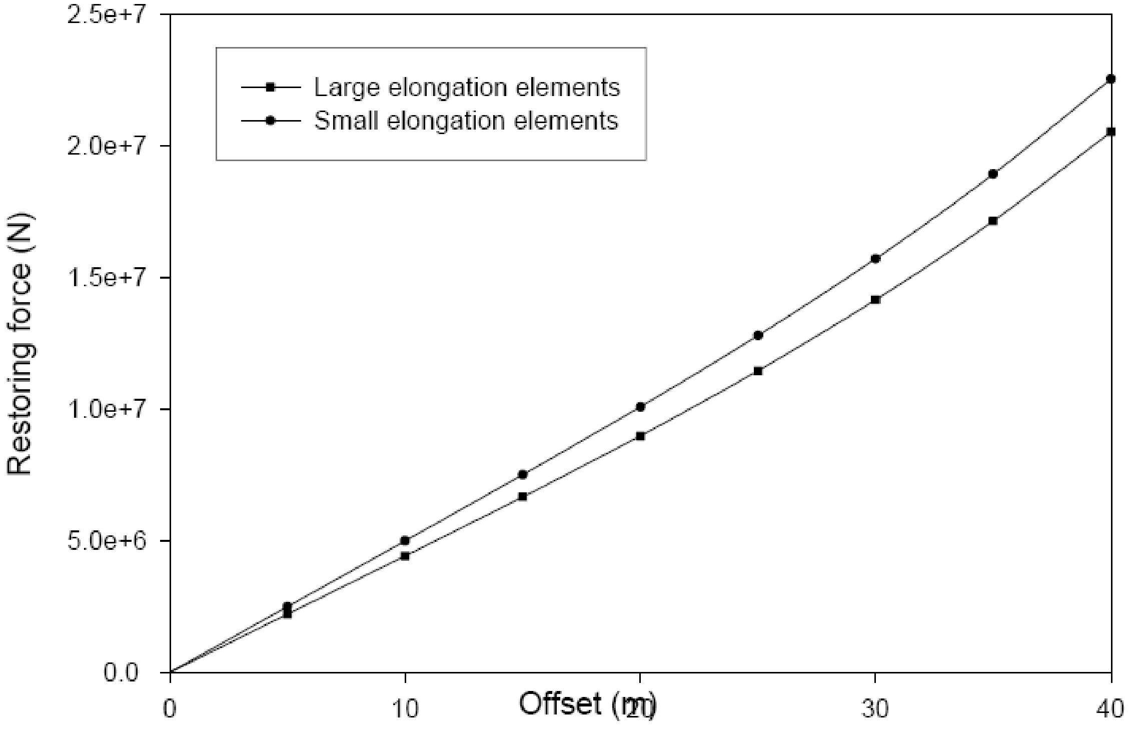

**Figure 5.1b:** Comparison of related static offset curves (water depth 6,000ft)

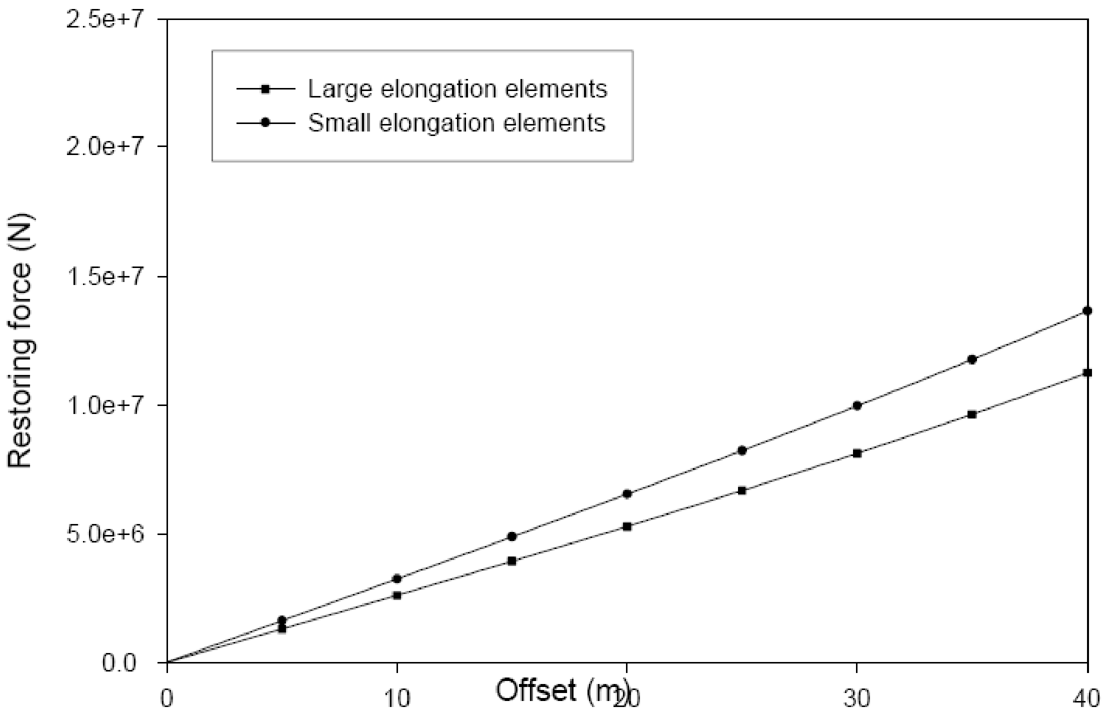

**Figure 5.1c:** Comparison of related static offset curves (water depth 10,000ft)

## 5.1 Global motions of the hull

The amplitude spectra of surge, sway and heave of the hull are shown in Figures 5.2 to 5.4. The surge and sway are dominated by the slow-drift motion. Typical amplitudes of the slow-drift surge range from 4 m to 8.5 m and those of sway from 2 m to 4 m. The amplitudes of the heave range from 1 m to 2 m. The average periods of the slow-drift surge and sway are similar, about 190 s, and that of the heave is about 30 s, which are all close to the corresponding natural periods determined by numerical simulation of free decay tests on the spar.

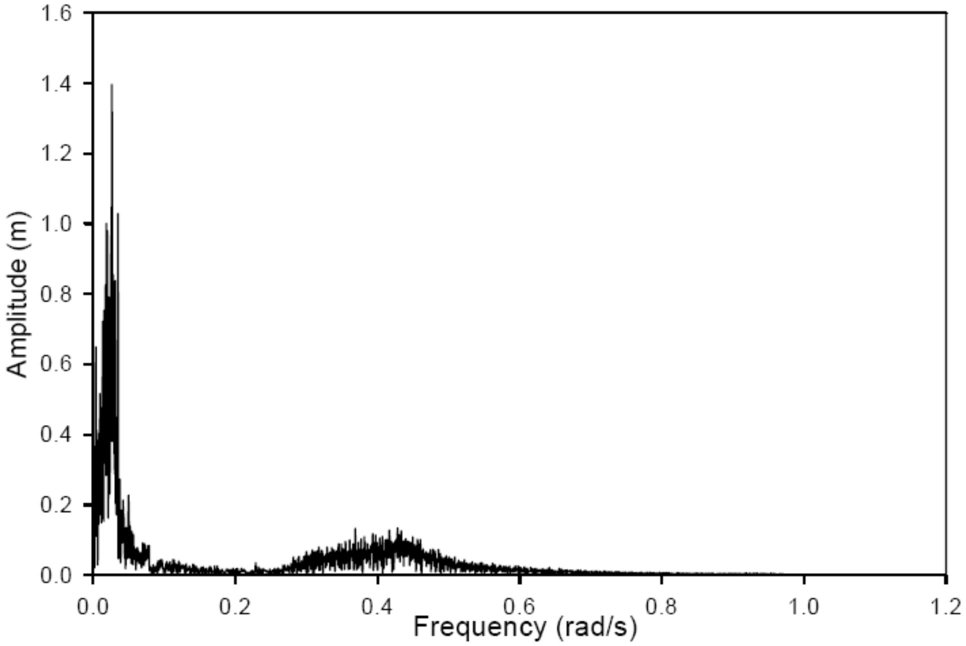

**Figure 5.2:** Surge amplitude spectrum

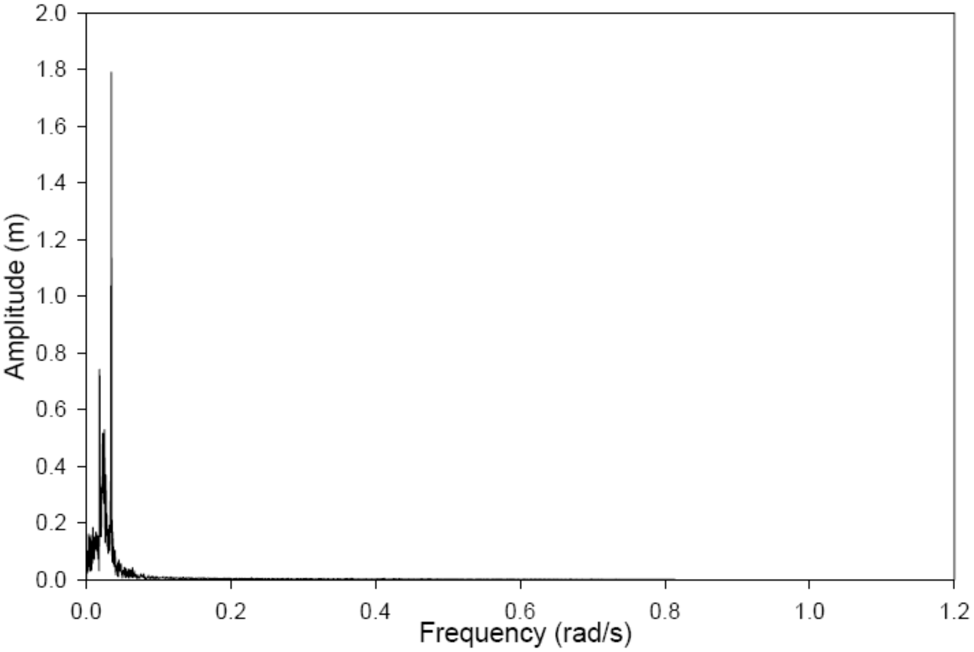

**Figure 5.3:** Sway amplitude spectrum

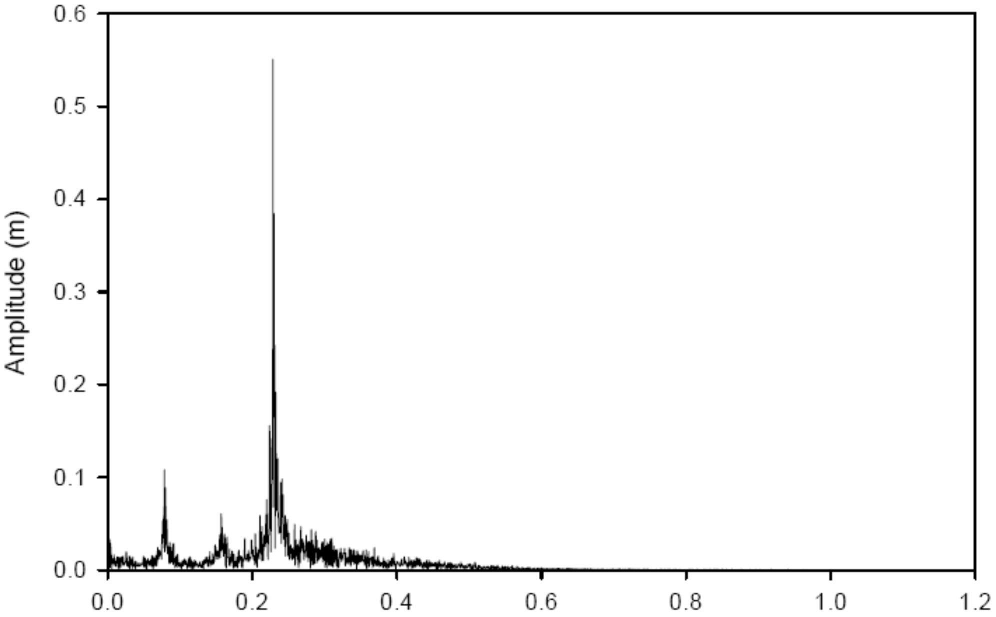

**Figure 5.4:** Heave amplitude spectrum

To provide an overall picture of a three-hour simulation, the statistics of the global motions of the hull are summarized in Table 5.2.

**Table 5.2.** Statistics of the global motions of the hull in 3000ft water

| | Mean | Standard Deviation | Max |
|---|---|---|---|
| Surge (m) | -1.78E+01 | 2.43E+00 | 2.57E+01 |
| Sway (m) | -2.44E+00 | 1.81E+00 | 6.86E+00 |
| Heave (m) | -1.19E-01 | 5.59E-01 | 2.46E+00 |
| Roll (degree) | 9.63E-01 | 8.11E-01 | 3.53E+00 |
| Pitch (degree) | -3.29E+00 | 1.73E+00 | 1.17E+01 |
| Yaw (degree) | -2.10E-02 | 1.155E-01 | 7.0E-02 |

### 5.2 Profiles and tensions of individual mooring lines

The maximum tension of each individual mooring line occurs at its fairlead. Considering that the most heavily loaded mooring line is #8 (weather side) and the least loaded one is #1 (leeward side), we present the amplitude spectra of their maximum tensions in Figures 5.5 and 5.6. The maximum tension in both lines seems dominated by the slow-drift surge and sway of the hull. However, the tension caused by the heave of the hull is also significant.

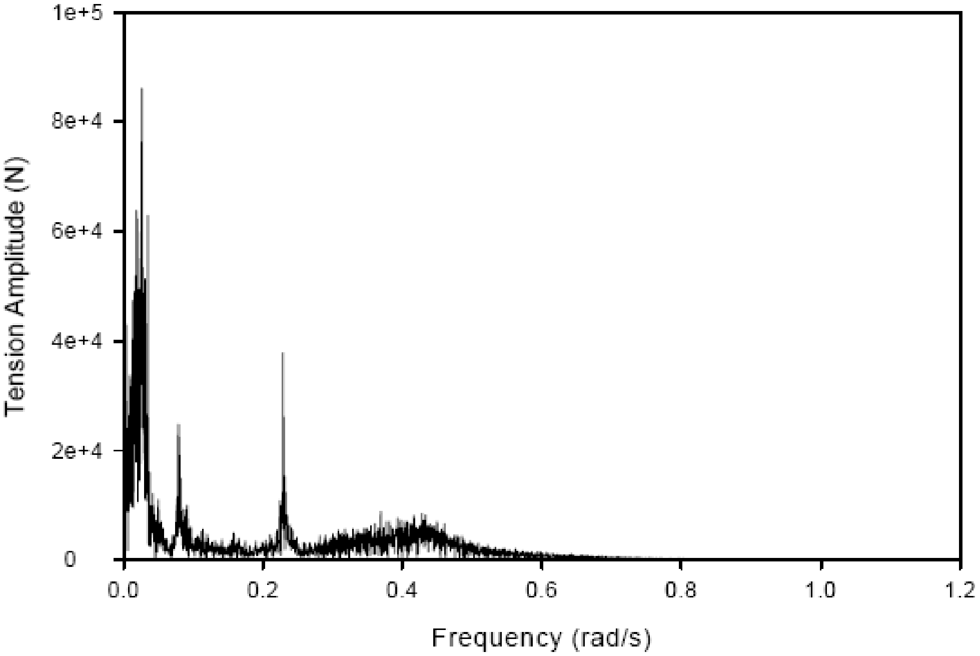

**Figure 5.5:** Line # 8 (weather side) tension amplitude spectrum

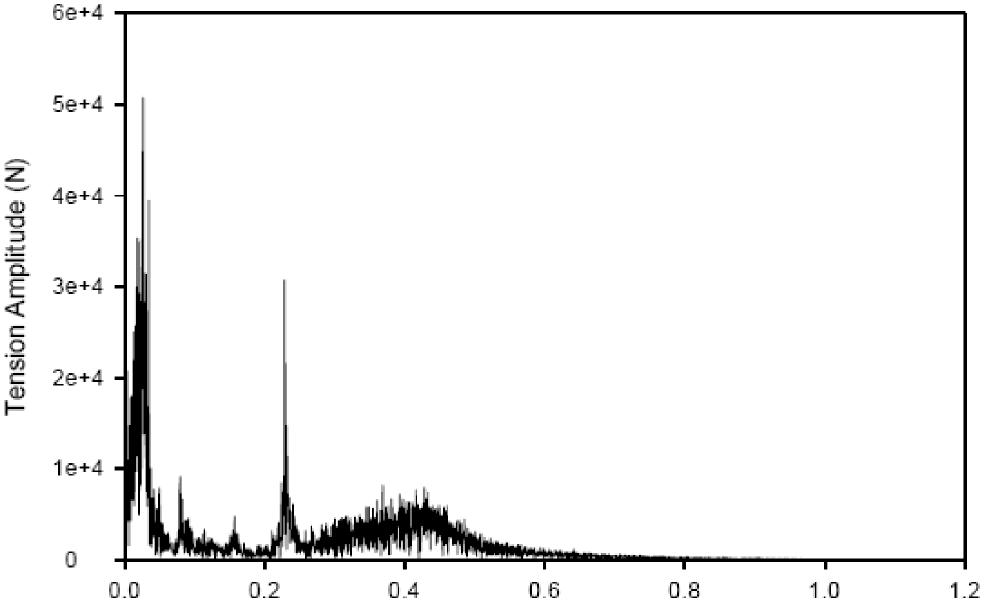

**Figure 5.6:** Line # 1 (leeward side) tension amplitude spectrum

For estimating the total forces applied to the suction anchors at depth below the mudline, the tension in each mooring line at the mudline and its angle with respect to the seabed are needed. Example results of lines #8 and #1 in 3,000 ft water are shown as function of time in Figures 5.7 to 5.10. Consistent with the tensions at the fairlead, the tension of line #8 at the mudline is significantly greater than that of line #1. In addition, the angle of line #8 is much greater than that of line #1.

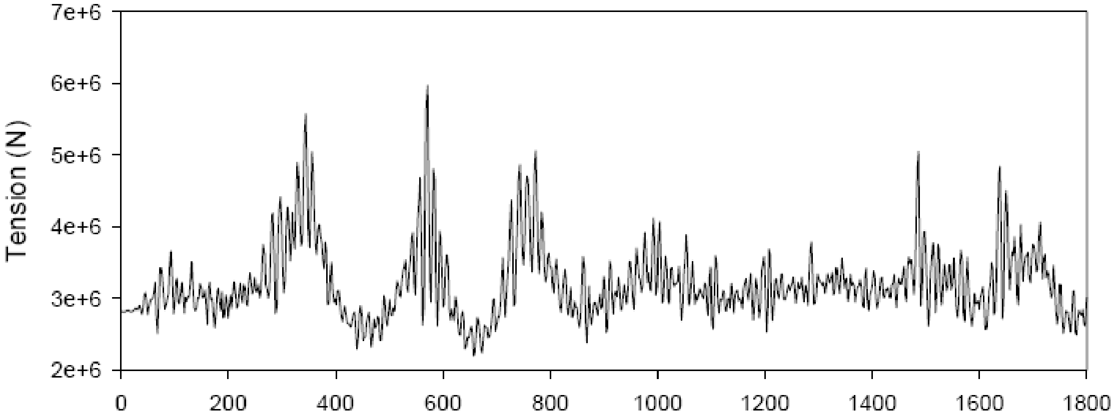

**Figure 5.7:** Tension of Line #8 (Weather side) at the mud line

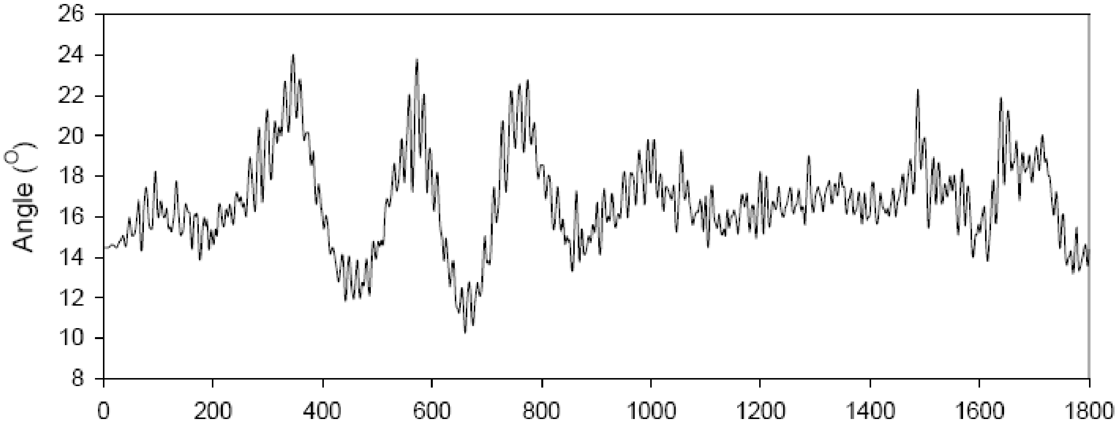

**Figure 5.8:** Angle of Line #8 (Weather side) with the seabed at the mudline

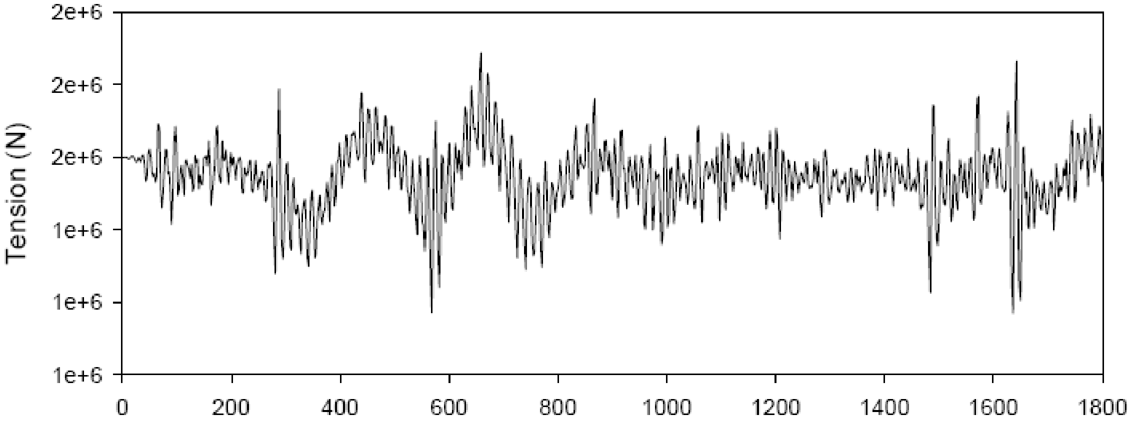

**Figure 5.9:** Tension of Line #1 (Leeward side) at the mudline

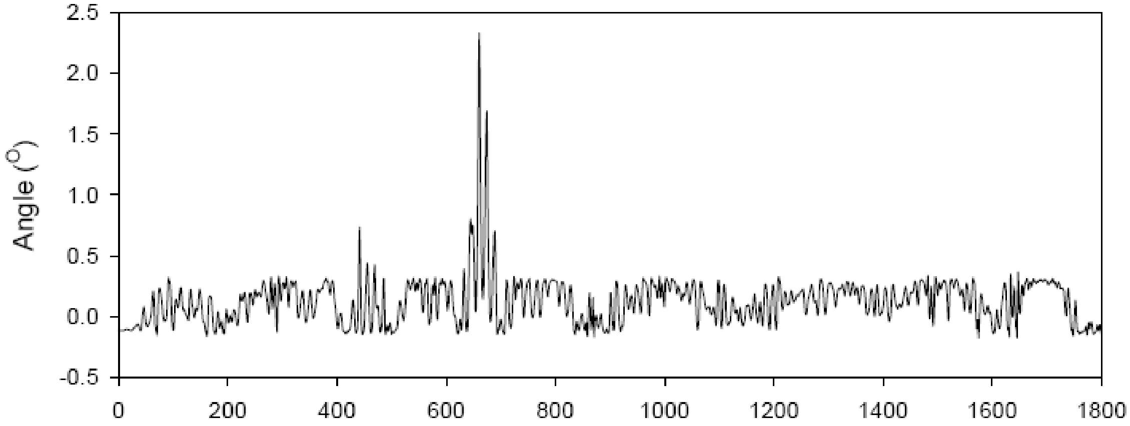

**Figure 5.10:** Angle of Line #1 (Leeward side) with the seabed at the mudline

To examine the dependence of the tension of mooring lines at the mud line on water depth, we present the tension spectra of line #8 at the mudline in three different water depths in Figures 5.11 to 5.13. These figures show that the tension of mooring lines at the mud line is dominated by the slow-drift surge, sway and heave motions of the hull. The comparison of the corresponding spectra also reveals that the tension in the wave frequency reduces with the increase in water depth.

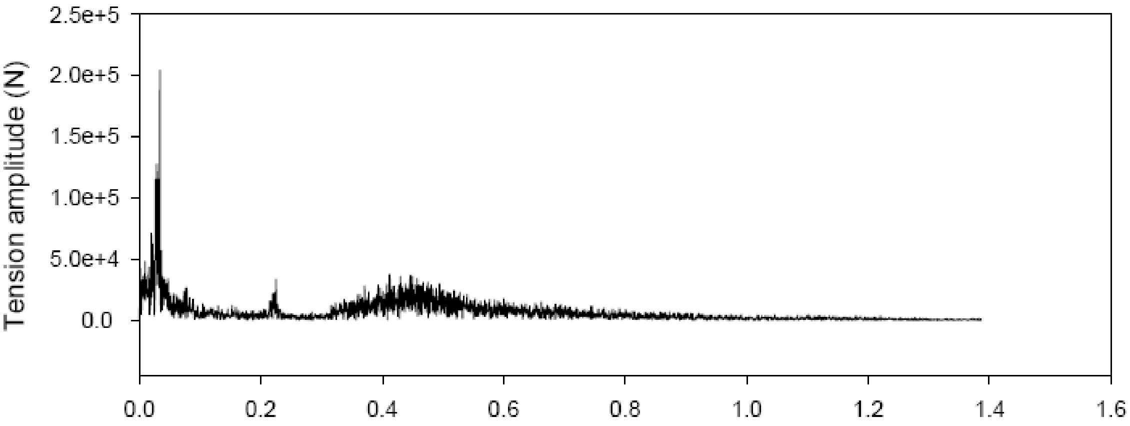

**Figure 5.11:** Tension amplitude spectrum of Line #8 at the mud line in 3,000ft water

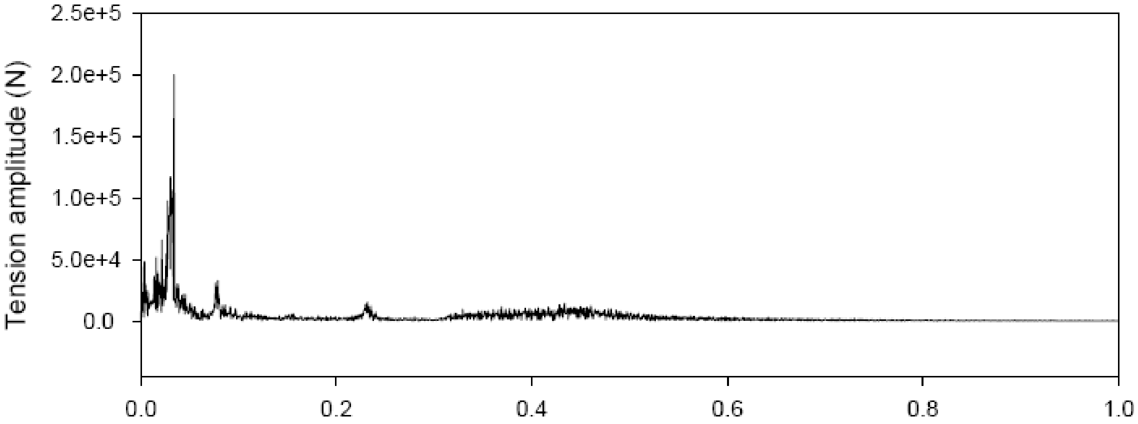

**Figure 5.12:** Tension amplitude spectrum of Line #8 at the mud line in 6,000ft water

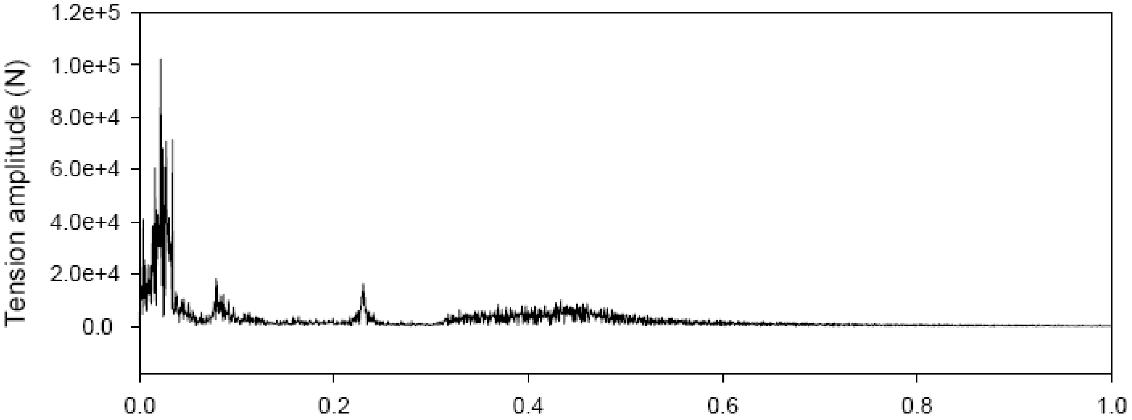

**Figure 5.13:** Tension amplitude spectrum of Line #8 at the mud line in 10,000ft water

## 6. Probability Distributions for Maximum Line Loads During Extreme Environmental Events

In this section, the methodology used to establish a probability distribution for the environmental conditions during a hurricane or loop current event is presented. This methodology consists of the following steps:

1. Determining the probability distribution of the maximum line load in a given sea state;
2. Determining the uncertainty in mean maximum line load due to uncertainty in the sea states that the spar is subjected to in its lifetime; and
3. Determining the uncertainty in the mean maximum line load due to uncertainty in the model parameters that are used in the COUPLE model.

These steps are described below using the load at the fairlead for a single line in the mooring system in the case that the mooring system is intact. However, the methodology is general and is used to determine the probability distribution for the maximum load (and its corresponding angle) at the mudline or the padeye of the anchor and for different configurations, such as a damaged mooring system.

### 6.1 Maximum line load in a given sea state

The procedure used for estimating the maximum load during a given sea state is described in Dangayach (2004). Tension load simulations of the mooring anchor system were generated by the COUPLE program for a given sea state. These simulations were then processed as follows to estimate the expected maximum load value and its standard deviation in that sea state.

From a theoretical perspective, if the variation of line loads with time behaves according to a Gaussian process, then the maximum load of in a storm duration T, $S_{max,T}$, can be expressed as follows:

$$S_{max,T} = \mu_{S(t)} + Y(T)\sigma_{S(t)} \tag{6.1}$$

where Y(T) is a defined as a peaking factor and $\mu_{S(t)}$ and $\sigma_{S(t)}$ are the mean and standard deviation of the time-varying load. Furtheremore, the mean and the standard deviation of the peaking factor, Y(T), are given by (Vanmarcke, 1983):

$$\mu_{Y(T)} = \sqrt{2\ln \nu_o^+ T} + \frac{0.577}{\sqrt{2\ln \nu_o^+ T}} \tag{6.2}$$

$$\sigma_{Y(T)} = \frac{\pi}{6}\frac{1}{\sqrt{2\ln \nu_o^+ T}} \tag{6.3}$$

where $\nu_o^+$ is the mean up-crossing rate (related to the frequency of variations). Therefore, Equations 6.2 and 6.3 indicate that the mean and standard deviation for the maximum load will be related to the square root of the natural logarithm of the storm duration for a Gaussian process.

While the time series for tension loads are not strictly Gaussian, we explain the applicability of using the form of the relationship in Equations 6.2 and 6.3 in order to approximate moving. In order to apply this theory, the 3-hour storm simulations were divided into 5, 10, 15, 20, and 30 minute intervals. The maximum load values were then picked up from each interval and the sample mean and standard deviation were calculated for each set (e.g., the sample mean of the 36 maximum values corresponding to a 5-minute duration).

Figures 6.1 and 6.2 show the results of this processing on ten 3-hour storm simulations of the same sea state for mooring line #8 at the fairlead. As expected by the theory, the mean value for the maximum increases approximately proportionally to the square root of the natural logarithm of the storm duration (Equation 6.2 and Figure 6.1). This result is useful because a single 3-hour storm simulation, which is the industry standard, can be used to estimate the mean value for the maximum load in a 3-hour storm by processing the simulation in smaller intervals. Otherwise, it would be necessary to estimate the mean value from a single point (there is only one maximum in a 3-hour simulation), which would not be reliable. The expected maximum value of the storm loads for a three hour storm obtained by this approach is 5033000 N (Figure 6.1). The standard deviation for the maximum is seen to be more or less constant with time duration of the storms, and equal approximately to 250,000 N (Figure 6.2). Therefore, the coefficient of variation (standard deviation divided by mean) for the maximum load on line #8, which represents the variability between 3-hour storm events, is roughly 250,000 N/5,033,000 N or 0.05.

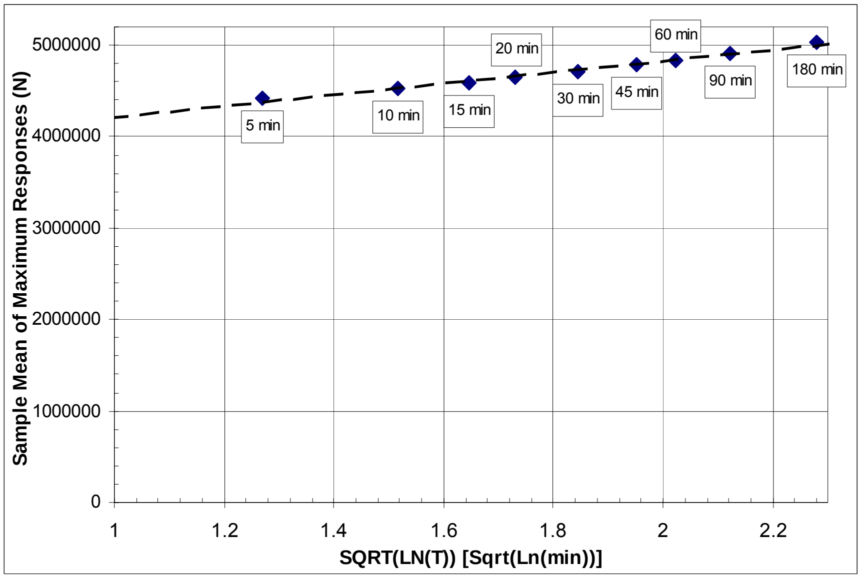

**Figure 6.1:** Expected values for the mean of the maximums for 5, 10, 15, 20, 30, 45, 60, 90, and 180 minute durations for ten separate three hour storms for mooring line #8 @ 3000 ft depth for a sea state with $H_S$= 9.32 m and $T_p$ = 12.64 s

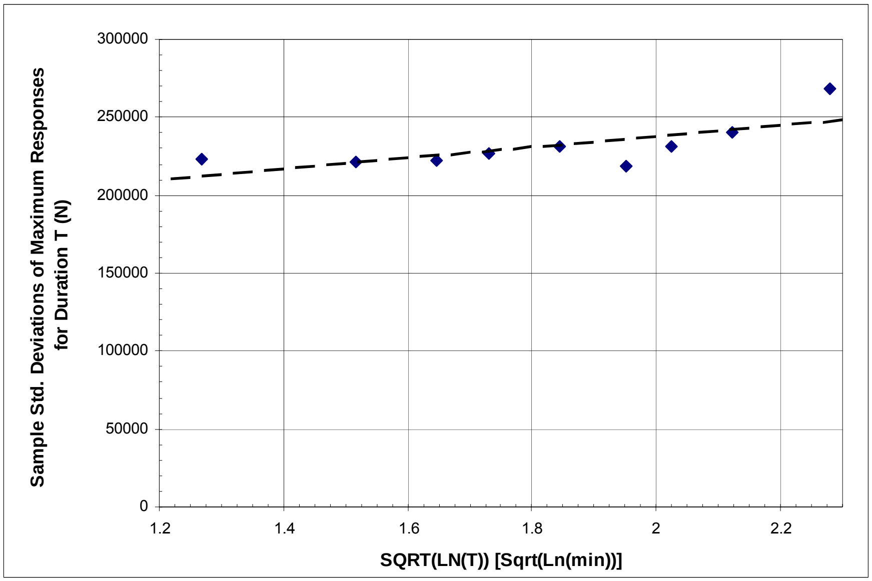

**Figure 6.2:** Standard deviation for the mean of the maximums for different durations for 10 three hour storms for mooring line #8 for the base storm event

## 6.2 Probability distribution of maximum line loads due to uncertain environmental conditions

In this section, the joint probability distributions representing environmental conditions during either a hurricane or a loop current are presented and the methodology used to develop the probability distribution of the maximum line load is described.

### 6.2.1 Probability distribution of maximum line loads due to hurricanes

A probabilistic distribution for the met-ocean parameters characterizing a storm in the Gulf of Mexico was adopted from Winterstein and Kumar (1995) and based on the GUMSHOE data base, which is an oceanographic database for Gulf of Mexico and comprises of hindcasts for 100 historical hurricane events in the Gulf of Mexico:

1. The *<u>significant wave height</u>* ($H_S$) has been modeled as a truncated Weibull distribution:

$$\Pr obability[H_S > h] = \exp\left[\left(\frac{h_{\min}}{h_0}\right)^{\gamma} - \left(\frac{h}{h_0}\right)^{\gamma}\right] \qquad (6.4)$$

where: $h_{min}$ =8.00 m, $h_0$ = 6.42 m, and $\gamma$ = 2.29.

2. The *<u>peak spectral period</u>* ($T_p$) is modeled as a conditional normal distribution with a c.o.v. of 0.06 and a mean value that depends on $H_s$:

$$E[T_p \mid H_S] = 5.39 * H_S{}^{0.382} \qquad (6.5)$$

where: $H_S$ is in meters and $T_p$ is in seconds.

3. The *<u>surface current velocity</u>* ($V_S$) is modeled as a linear function of $H_S$:

$$V_S\,(\text{fps}) = 0.056 * H_S\,(\text{ft}) + 1.0625 \qquad (6.6)$$

4. The *one hour mean wind speed* ($v_w$) is also modeled as a linear function of $H_S$:

$$V_w \text{ (mph)} = 1.895 * H_S \text{ (ft)} + 18.316 \qquad (6.7)$$

Therefore, the hurricane is characterized completely by two parameters: $H_S$ and $T_P$. In addition, hurricanes at the spar location in the Gulf of Mexico were assumed to occur independently with an annual rate of occurrence, $\nu$, of 0.1 per year.

Using this information, a joint probability distribution of $H_S$ and $T_P$ can be developed that includes both the likelihood of different combinations of $H_S$ and $T_P$ in a hurricane as well as the frequency of hurricanes (Winterstein and Kumar 1995). This joint probability distribution is expressed as a reliability contour on Figure 6.3. For each contour in this figure, the volume of the joint probability distribution outside of a tangent line to the contour has a constant value. For the 50-year contour, this volume of probability is 1/50 in a one-year period. For the 100-year contour, this probability is 1/100 in a one-year period. These contours, which will be referred to as annual reliability contours, are useful because they express the distribution for Hs and Tp in terms related to the return periods specified in the design guidelines.

One noteworthy aspect of the contours on Figure 6.3 is that the 100-year event with the maximum $H_s$ value corresponds to the 100-year $H_s$. Based on these contours, derived from the GUMSHOE data base (Winterstein and Kumar 1995 and Banon et al. 1990), the 100-year $H_s$ value is 38.4 ft. However, the typical 100-year value in the API code (Table 2.3) and the value used in the design of this spar is 40 ft. Therefore, either the value used in the code is a bit conservative or the probability distributions developed by Winterstein and Banon based on GUMSHOE are slightly unconservative.

For the reliability analysis, we are concerned about the response of the structure to storms occurring during its design life. The design life of the theme spar was assumed to be 20 years. Therefore, the annual reliability contours have been converted (assuming storm occurrences follow a Poisson process) into 20-year reliability contours on Figure 6.4. Here, the probability of being outside of a tangent line along the contour in a 20-year period corresponds to complement of the percentile. For example, this probability is 5 percent for the contour labeled 95th percentile.

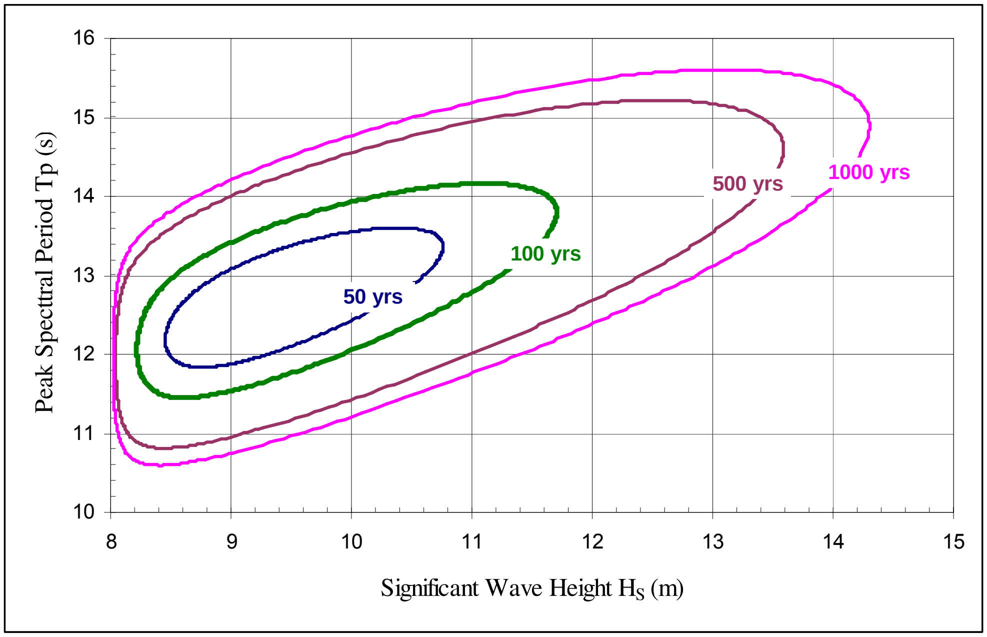

**Figure 6.3:** $H_S$-$T_p$ annual reliability contours due to hurricanes in Gulf of Mexico

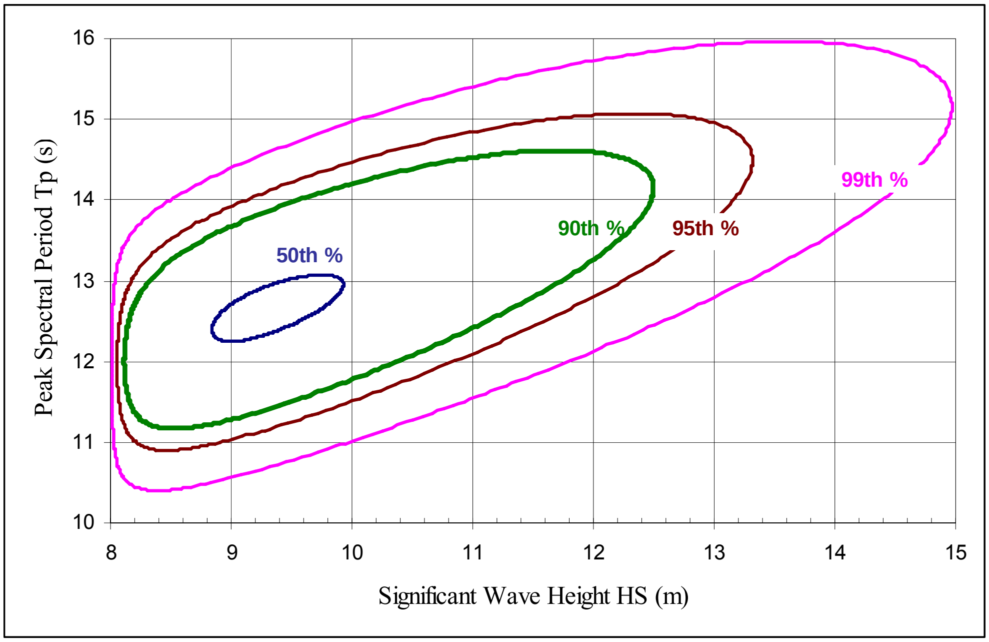

**Figure 6.4:** $H_S$-$T_P$ reliability contours due to hurricanes for a 20 year design life

A probability distribution for the maximum line loads in a 20-year design life can be obtained by combining the information on the maximum line load during a given 3-hour storm (Section 6.1) with the probability distribution for the occurrence of different storm events.

Three hour storm simulations (generating loading history of the structure) were carried out for a number of sea states and the expected maximum loads during a 3-hour storm were estimated using the approach depicted on Figure 6.1. Figure 6.5 shows an example of the results of this analysis. The expected maximum load contours on this plot have a nearly vertical trend, indicating that the loads on this structure during a storm event depend mostly on the significant wave height of the sea state.

Figure 6.6 combines Figures 6.4 and 6.5 and shows the load contours and the $H_S$-$T_p$ likelihood contours on the same graph. Figure 6.6 can then be used to establish the probability distribution for the expected maximum load: the 50th percentile value is 5,144 kN; the 90th percentile value is 7,158 kN; and the 95th percentile value is 7,512 kN. A lognormal distribution provides a reasonable and convenient fit to these percentiles: the median value for the mean maximum load is 5,144 kN and the coefficient of variation (c.o.v.) is 0.25. In comparison to the c.o.v. in the maximum in a given sea state, 0.05, the c.o.v. in the maximum due to uncertainty in the occurrence of different sea states, 0.25, is significantly larger and therefore dominant. Figure 6.8 combines Figures 6.4 and 6.7 and shows each of three percentile values for spar in 6,000 ft of water while Figure 6.10 combines Figures 6.4 and 6.9 and indicates them for spar in 10,000 ft of water.

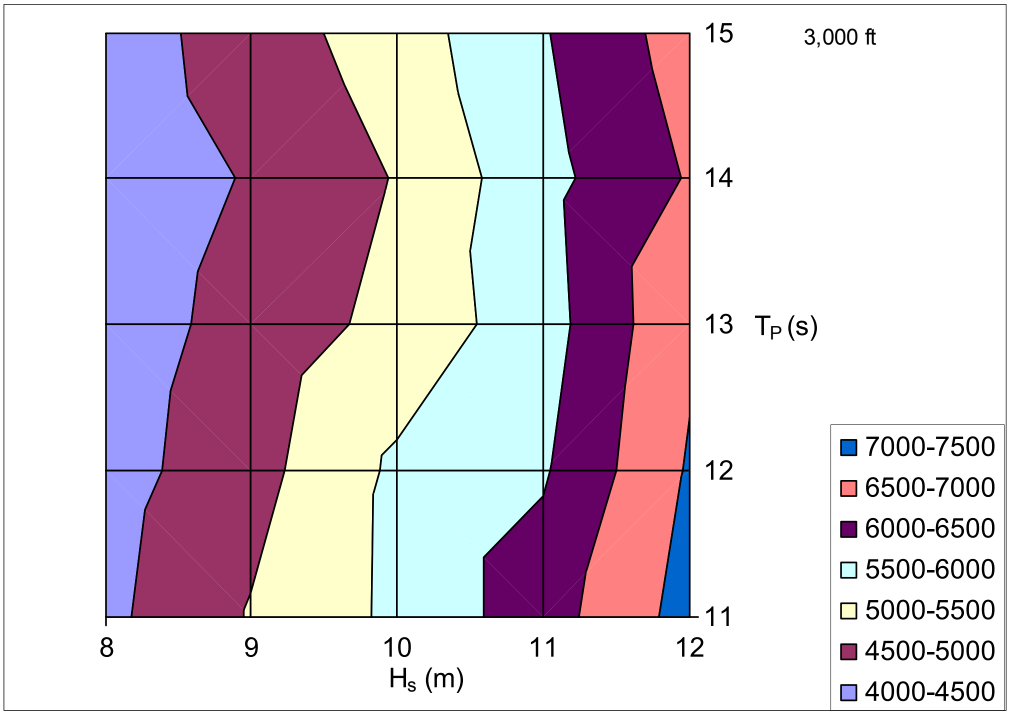

**Figure 6.5:** Expected maximum load (in kN) during a 3-hour storm for 3,000-ft water depth

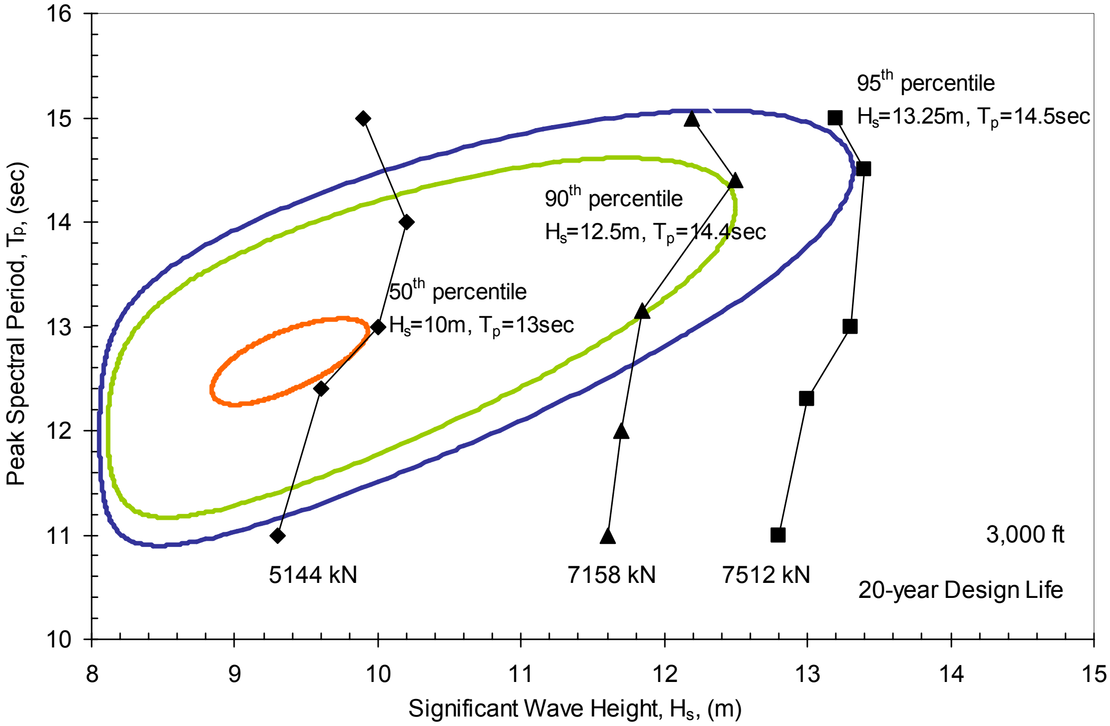

**Figure 6.6:** Superposition of Figures 6.4 and 6.5 for spar in 3,000 ft of water

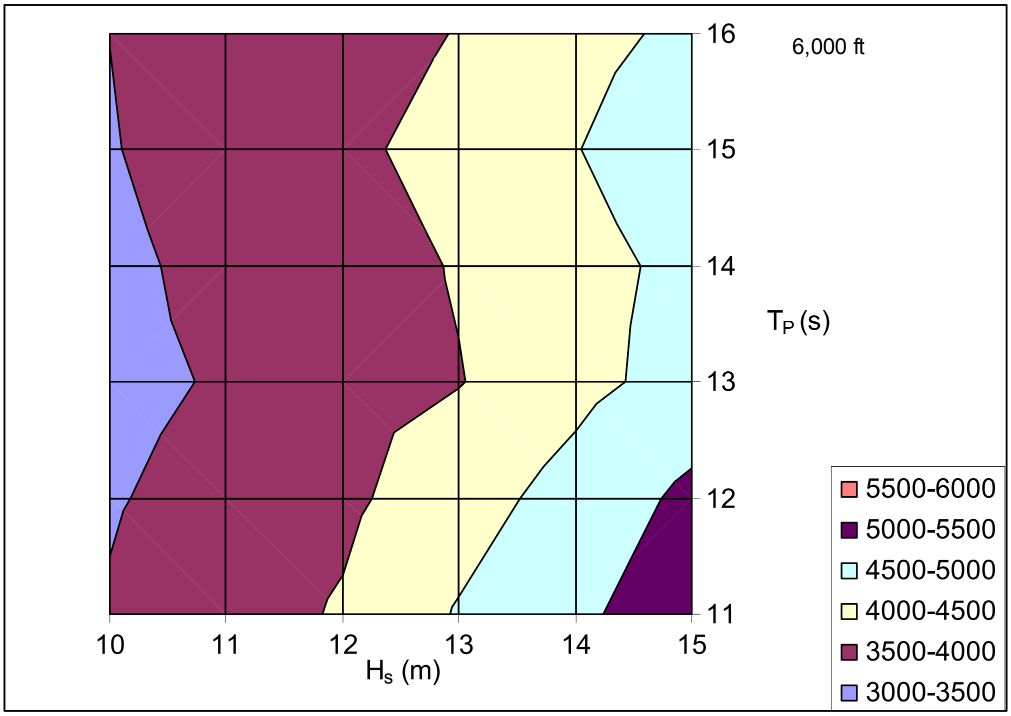

**Figure 6.7:** Expected maximum load (in kN) during a 3-hour storm for 6,000-ft water depth

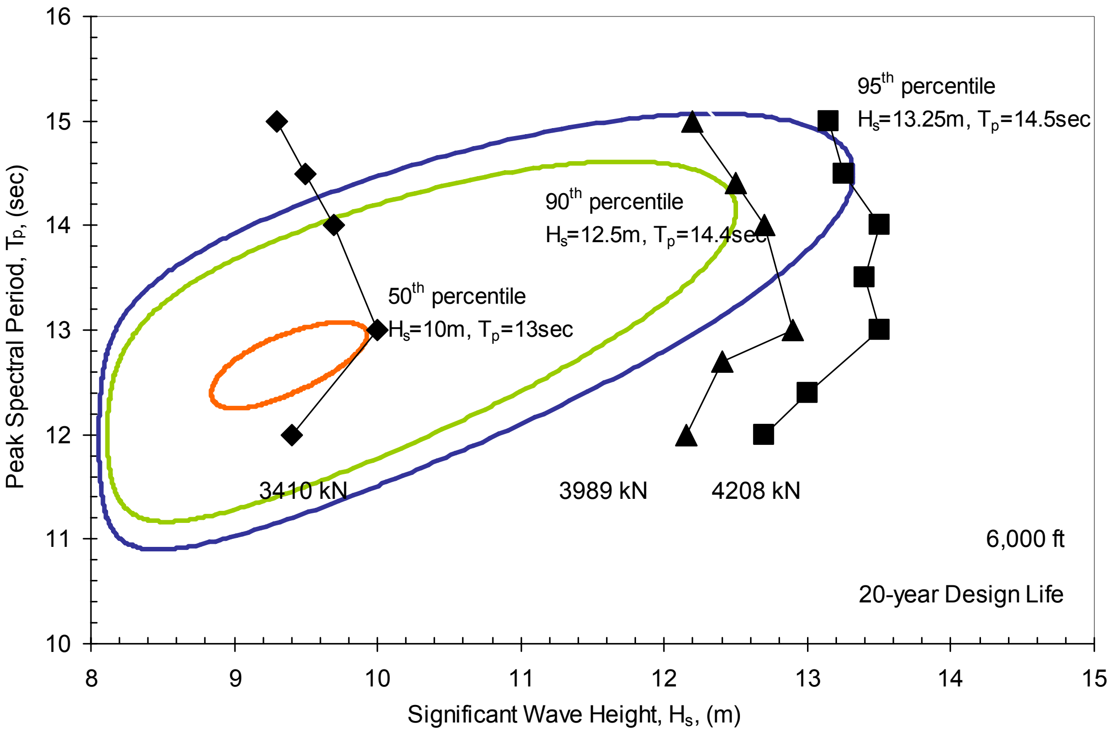

**Figure 6.8:** Superposition of Figures 6.4 and 6.7 for spar in 6,000 ft of water

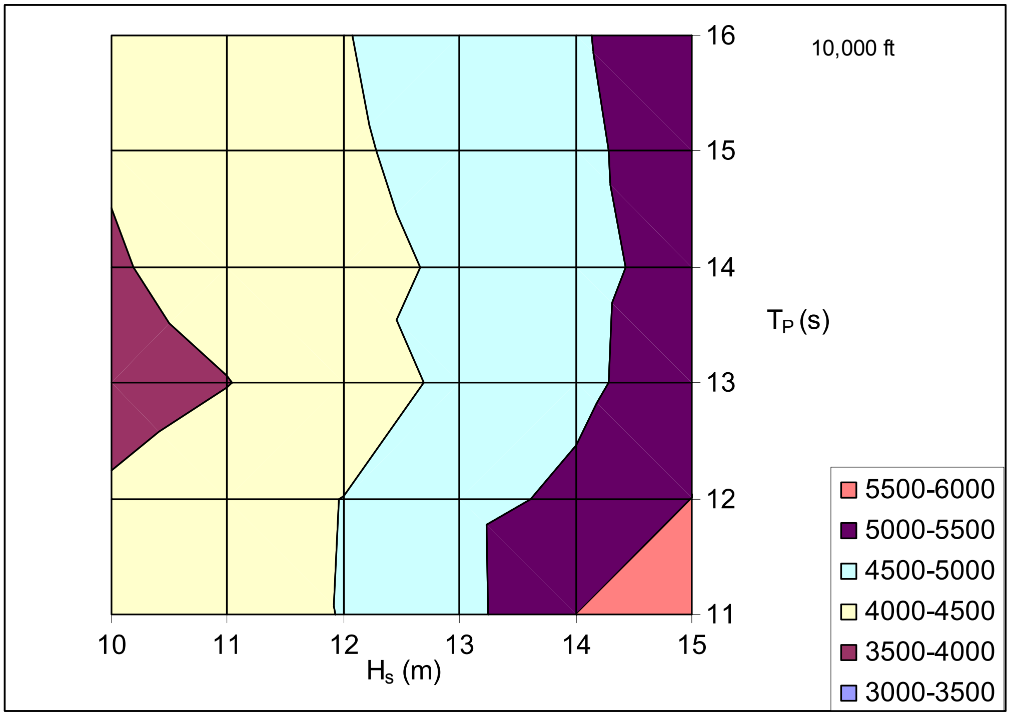

**Figure 6.9:** Expected maximum load (in kN) during a 3-hour storm for 10,000-ft water depth

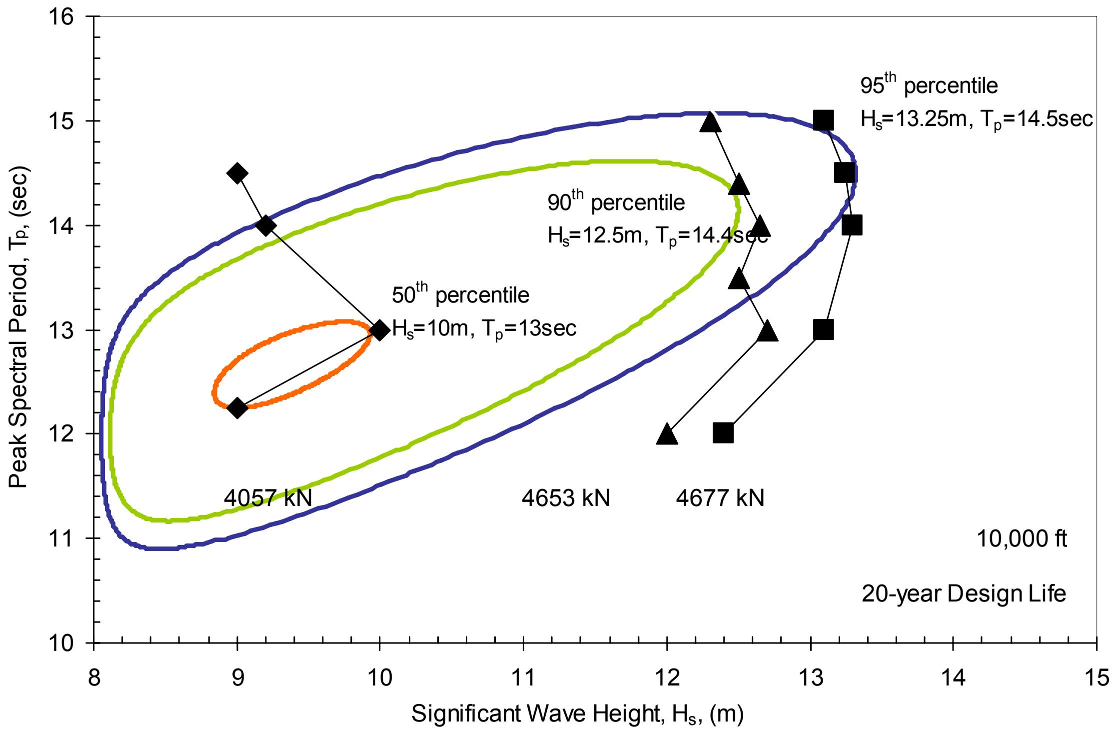

**Figure 6.10:** Superposition of Figures 6.4 and 6.9 for spar in 10,000 ft of water

### 6.2.2 Probability distribution of maximum line loads due to loop currents

The event that loop currents occur in the Gulf of Mexico is assumed to be independent of the winds and waves ($T_p$ and $H_s$). Therefore, the primary variable describing the loop current is the maximum velocity for the surface current. The probability distribution for the maximum velocity due to a loop current for an exposure time of 20 years is developed using the following information (Ward 2005, personal communication): (1) the 100-year current surface velocity is equal to 7 feet/sec (fps); (2) the 10-year current surface velocity is 6.3 fps; and (3) the occurrence frequencies for loop current events range from one per 6 to 17 months. With these assumptions, the CDF for the maximum current velocity in a 20 year design life can be derived as follows:

1. The maximum current velocity with a specified duration is assumed to follow either a Type II distribution or a Weibull distribution. Since no acceptable distribution about the maximum velocity is available in practice, both distributions have been used in this study.
2. Let F(y) be the probability that the maximum current velocity during an event is less than or equal to a specific current velocity value (y). Let G(y) be the probability that the maximum current velocity is greater than y. F(y) and G(y) for both Type II and Weibull distributions can be expressed as follows:

For Type II, $F_{II}(y) = P(V_{current} \le y) = \exp[-(u/y)^k]$

$G_{II}(y) = P(V_{current} > y) = 1 - \exp[-(u/y)^k]$

For Weibull, $F_{III}(y) = P(V_{current} \le y) = 1 - \exp[-(y/\alpha)^{\beta}]$

$G_{III}(y) = P(V_{current} > y) = \exp[-(y/\alpha)^{\beta}]$

where (u, k) and (α, β) are the parameters characterizing Type II and Weibull distributions, respectively, and $V_{current}$ is the maximum velocity of a current.

3. CDFs for the annual maximum current velocity can be estimated using G(y) combined with a Poisson process.

$$F_{II,\,T=1}(y) = P(\text{annual }\ V_{current} \le y) = \exp[-\nu G_{II}(y)] \quad \text{or}$$
$$F_{III,\,T=1}(y) = P(\text{annual }\ V_{current} \le y) = \exp[-\nu G_{III}(y)]$$

where ν is the occurrence frequency for loop current events.

With the given 100-year and 10-year current velocities, the parameters of (u, k) and (α, β) can be estimated as follows:

- A 100-year current velocity of 7 fps will not be exceeded with probability of 0.99 (=1-1/100) in any year (for Type II case).

$$F_{II,\,T=1}(7) = P(\text{annual }\ V_{current} \le 7) = 1 - 0.01 = 0.99$$
$$F_{II,\,T=1}(7) = 0.99 = \exp[-\nu(1 - \exp\{-(u/7)^k\})] \tag{6.1}$$

- Similarly, the likelihood that a 10-year current velocity will not be exceeded can be calculated as follows:

$$F_{II,\,T=1}(6.3) = 0.9\ (= 1 - 1/10) = \exp[-\nu(1 - \exp\{-(u/6.3)^k\})] \tag{6.2}$$

Using Equations 7.1 and 7.2, the Type II distribution parameters u and k can be calculated. Likewise, the Weibull distribution (Type III) parameters α and β can be calculated using Equations 6.3 and 6.4.

$$F_{III,\,T=1}(7) = 0.99 = \exp[-\nu \exp\{-(7/\alpha)^{\beta}\}] \tag{6.3}$$
$$F_{III,\,T=1}(6.3) = 0.90 = \exp[-\nu \exp\{-(6.3/\alpha)^{\beta}\}] \tag{6.4}$$

4. Lastly, the maximum current velocity distribution for an exposure of T=20 years can be described using the Poisson process.

$$F_{II,T=20}(y) = P(V_{current}\ \text{in 20 years} \le y) = \exp[-\nu T\{1\text{-}\exp(\text{-}(u/y)^k)\}] \tag{6.5}$$
$$F_{III,T=20}(y) = P(V_{current}\ \text{in 20 years} \le y) = \exp[-\nu T \exp\{\text{-}(y/\alpha)^{\beta}\}] \tag{6.6}$$

A range of parameters characterizing the cumulative distributions of the maximum current velocity are summarized in Table 6.1.

The resulting CDFs for different occurrence rates for loop currents are shown in Figure 6.11 and Figure 6.12. From the results in these figures, it is concluded that there is little effect of the occurrence frequency on the maximum current velocity distributions for both distributions over a wide range of current velocities. Accordingly, a typical frequency of 1 per year will be used hereafter. However, as expected from an extreme distribution, the data in Figure 6.8(c) indicates a more significant difference in behavior for the two distributions near the upper tail between Type II and Weibull distributions. In Figure 6.8, the inverse CDF values of 1 and 4 are equal to CDF values of about 0.8413 and 0.9997, respectively. Accordingly, the probability that the maximum current velocity is less than or equal to 7 fps in a 20-year design life has a CDF value of about 0.8413 for both cases. However, the maximum current velocities corresponding to a probability of 0.9997 are about 8.2 fps for the Weibull distribution and 10.3 fps for the Type II distribution, indicating a greater impact of the distribution choice at higher maximum current velocities. Due to uncertainty at present in the most appropriate distributional form for the current velocity, reliability analyses are conducted using both the Type II and Weibull distributions.

The associated winds and waves during a loop current event are assumed to be independent of the current velocity. We consulted a recent reliability study (Smith 2005), where the associated values of $H_s$ and $T_p$ during a loop current event were 9.84 feet and 7.9 seconds, respectively. As a check, we also obtained and analyzed data from a weather buoy in the Gulf of Mexico. The median values (the most likely associated sea state) for $H_s$ and $T_p$ were very similar to those above. Therefore, we used this pair of $H_s$ and $T_p$ to represent the sea state during the maximum loop current event in a 20-year time period (Table 6.2). Note that the design values for $H_s$ and $T_p$ are 20 feet and 11 seconds, respectively (Table 2.3). We also used the same expected current profile versus depth as that used by Smith (2005) in the reliability analyses (Table 6.2 and Figure 6.13).

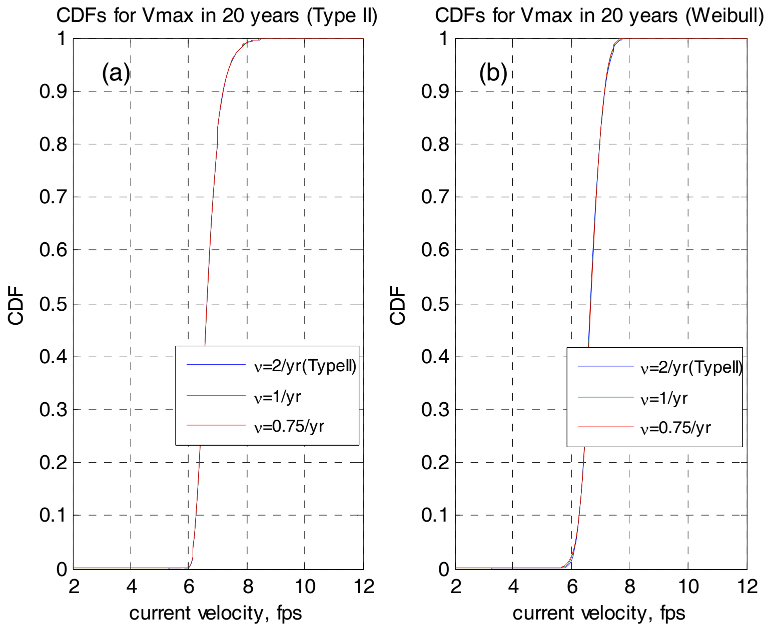

Figure 6.11: CDFs for the maximum current velocity with different return periods of 6, 12 and 16 months: (a) Type II distribution; (b) Weibull distribution

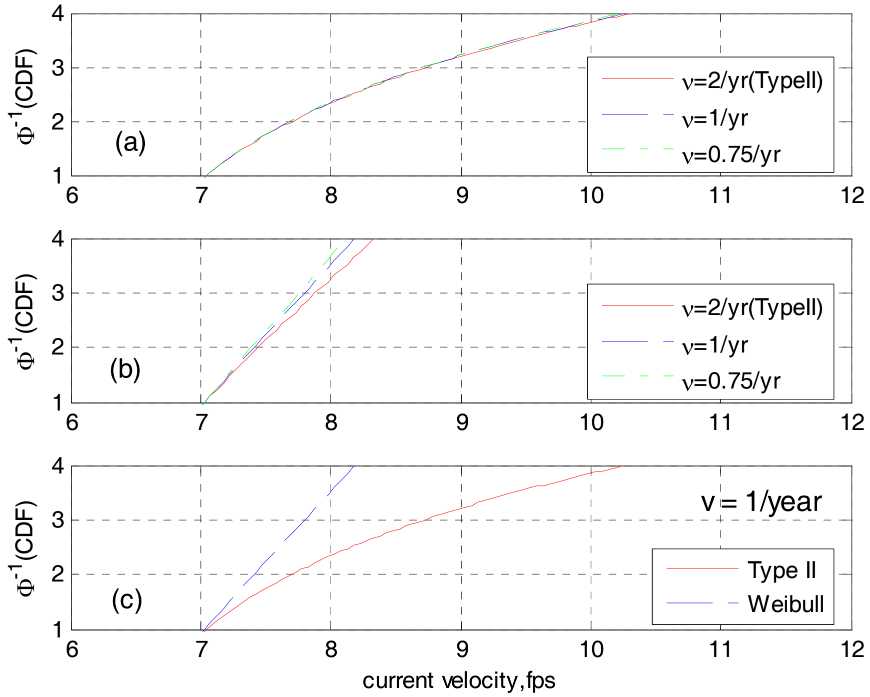

Figure 6.12: Comparison of inverse CDFs with different event occurrence frequencies: (a) Comparison of inverse CDFs for the Type II distribution; (b) Comparison of inverse CDFs for the Weibull distribution; (c) Comparison of the TypeII and Weibull distributions with ν=1 per years

Table 6.1: Parameters characterizing Type II and Weibull distributions depending on loop current frequencies

| | CDF for maximum current during event | | | |
|---|---|---|---|---|
| | Type II | | Weibull | |
| Loop Current Frequency, ν (times/year) | u | k | α | β |
| 2 | 5.54 | 22.53 | 5.19 | 5.57 |
| 1.5 | 5.61 | 22.61 | 5.36 | 6.02 |
| 1.2 | 5.67 | 22.70 | 5.48 | 6.42 |
| 1 | 5.72 | 22.78 | 5.59 | 6.79 |
| 0.86 | 5.76 | 22.86 | 5.68 | 7.14 |
| 0.75 | 5.80 | 22.95 | 5.76 | 7.47 |

Table 6.2: Sea states used in the numerical model for the case of loop current

| No. | $H_S$ (ft) | $T_P$ (sec) | $V_W$ (fps) | Jonswap (γ) | $V_{max}$ (fps) | Percentile (%) | Assumption |
|---|---|---|---|---|---|---|---|
| 1 | 9.84 | 7.9 | 32.8 | 2.75 | 6.68 | 50 | Weibull |
| 2 | 9.84 | 7.9 | 32.8 | 2.75 | 7.14 | 90 | |
| 3 | 9.84 | 7.9 | 32.8 | 2.75 | 7.28 | 95 | |
| 4 | 9.84 | 7.9 | 32.8 | 2.75 | 7.55 | 99 | |
| 5 | 9.84 | 7.9 | 32.8 | 2.75 | 7.85 | 99.9 | |
| 6 | 9.84 | 7.9 | 32.8 | 2.75 | 8.11 | 99.99 | |
| 7 | 9.84 | 7.9 | 32.8 | 2.75 | 8.32 | 99.999 | |
| 8 | 9.84 | 7.9 | 32.8 | 2.75 | 6.63 | 50 | Type II |
| 9 | 9.84 | 7.9 | 32.8 | 2.75 | 7.20 | 90 | |
| 10 | 9.84 | 7.9 | 32.8 | 2.75 | 7.43 | 95 | |
| 11 | 9.84 | 7.9 | 32.8 | 2.75 | 7.99 | 99 | |
| 12 | 9.84 | 7.9 | 32.8 | 2.75 | 8.84 | 99.9 | |
| 13 | 9.84 | 7.9 | 32.8 | 2.75 | 9.78 | 99.99 | |
| 14 | 9.84 | 7.9 | 32.8 | 2.75 | 10.83 | 99.999 | |

Notes: $V_W$ is the wind speed at 10 m above sea level; γ is the JONSWAP sharp factor; $V_{max}$ is the maximum current velocity.

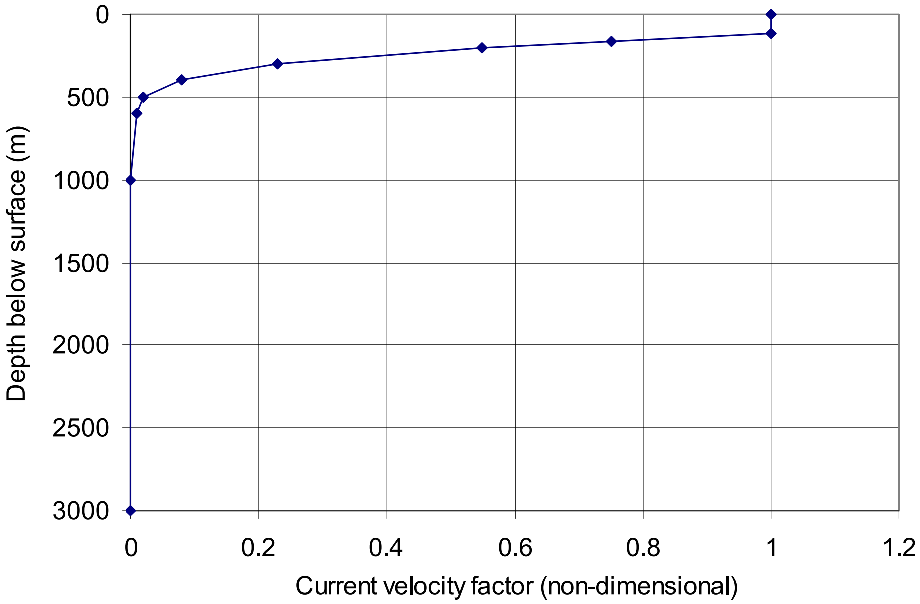

Figure 6.13: The profile of current velocity factor (non-dimensional) during a loop current

## 6.3 Uncertainty in model parameters

In addition to uncertainty in the environmental conditions, there is also uncertainty in the loads due to uncertainty in the COUPLE model used to predict loads. The five most significant model parameters affecting the response of the structure are the drag force coefficient, $C_D$, the added mass coefficient, $C_M$, the VIV lifting force coefficient, $C_L$, Strouhal number, St, and the shape coefficient due to wind loads, $C_S$. Since the exact values for these model parameters are not known for the theme spar, a first-order analysis was conducted to determine how significant this source of uncertainty is on the maximum line load. To study the effect of the parameters on the maximum load, each of these parameters was varied keeping the values of other parameters fixed. The storm simulations were carried out for the sea state: $H_S = 9.32$ m and $T_p = 12.64$ s. The sensitivity of the maximum load to each parameter was calculated as a percentage change in the maximum load due to a percentage change in the model parameter. The results are shown on Figure 6.14.

In order to study the effect of the model parameters on the predicted loads, separate storm simulations were run with each of the physical parameters being varied, one at a time, keeping the other parameters unchanged. The storm simulations were carried out for the base storm event ($H_S = 9.32$ m and $T_p = 12.64$ s). Table 6.3 provides a summary of the storm simulations and the resulting expected maximum load values for mooring line #8 at the fairlead for 3,000 ft water depth. A sensitivity factor, Si, was calculated for each parameter i using the following equation:

$$\Delta\mu_{Xi} = \frac{\mu_{Xi+D} - \mu_{Xi-D}}{\mu_X}\% \qquad (6.7)$$

where: $\Delta\mu_{Xi}$ is the percentage change in the maximum load value in a three hour storm due to variation in the physical parameter I; D is an amount of change in % in each parameter; $\mu_{Xi+D}$ is the maximum load at the fairlead on mooring line #8 when the value of parameter i is increased by D%; $\mu_{Xi-D}$ is the maximum load at the fairlead on mooring line #8 when the value of parameter i is decreased by D%; and $\mu_X$ is the maximum load at the fairlead on mooring line #8 when none of the parameter values are changed.

$$S_i(\%) = \Delta\mu_{Xi} \Big/ 2D \tag{6.8}$$

In this analysis, the values of D were selected (Table 6.3) for each parameter in collaboration with the Ocean Engineering Program, Texas A&M University to be representative of a reasonable range of possible values for that parameter. Figure 5.1 shows a bar graph with sensitivities for all the model parameters.

The sensitivity results can be used in a first order approximation to estimate the magnitude of model uncertainty. If the model errors for each parameter are multiplicative and statistically independent (as a rough approximation), then the coefficient of variation (c.o.v.) in the predicted value of the expected maximum load can be estimated as follows:

$$\Omega_{\mu_X}{}^{2} \cong \sum_{\forall \, \mathrm{mod}\, el\_parameters} S_i^2 \Omega_i^2 \tag{6.9}$$

where: i is the c.o.v. for each model parameter.

The c.o.v. value for each individual parameter was conservatively assumed to be one half of the range that was selected to represent the possible values. For example, a ±10% range was used for $C_D$, so a c.o.v. of 0.05 was assumed for $C_D$.

The resulting c.o.v. in the load, $\Omega_{\mu x}$, was estimated to be 0.02 from Equation 6.9. Therefore, the predicted maximum loads in the mooring lines are relatively insensitive to the model parameters for the theme spar. The reason for this small model uncertainty is that the line loads are dominated by pre-tension versus environmental loads. In order to be conservative, a value of 0.05 was used to represent model uncertainty in the predicted loads for both hurricane and loop current events.

**Table 6.3:** Sensitivity of expected maximum load to model parameters – mooring line #8 , 1000 m water depth

| Case | Variation in the parameter(s) | Max load at fairlead for ML#8 (N) | Sensitivity of load to change in parameter |
|---|---|---|---|
| 1 | No variation in parameter values | 4840210 | -- |
| 2 | $C_D$ increased by 10 % | 4877470 | 6.8% |
| 3 | $C_D$ decreased by 10 % | 4811730 | |
| 4 | $C_M$ increased by 10 % | 4875330 | 6.9% |
| 5 | $C_M$ decreased by 10% | 4808660 | |

| | | | |
|---|---|---|---|
| 6 | $C_L$ increased by 25 % | 4876520 | 2.6% |
| 7 | $C_L$ decreased by 25 % | 4814550 | |
| 8 | $S_0$ increased by 10 % | 4784930 | -11% |
| 9 | $S_0$ decreased by 10 % | 4898350 | |
| 10 | $C_S$ increased by 20 % | 5001770 | 18% |
| 11 | $C_S$ decreased by 20 % | 4652030 | |

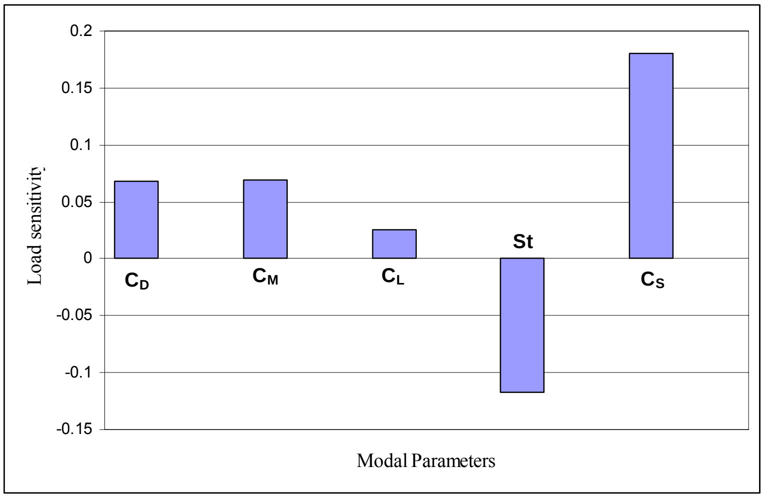

**Figure 6.14:** Sensitivity of the maximum load to the variation in model parameters for design spar in 3,000 feet of water under hurricane loading

## 6.4: Overall uncertainty in maximum line loads

The total uncertainty in the maximum line loads results from variations in maximum loads between individual 3-hour storm events (Section 6.1), variations in the mean maximum load due to variations in the metocean environment over a 20-year design life (Section 6.2), and uncertainty in the mean maximum load due to uncertainty in the response model (Section 6.3). These three sources of uncertainty are depicted in Figure 6.15; the uncertainty due to the metocean environment is the dominant source of uncertainty for this structure.

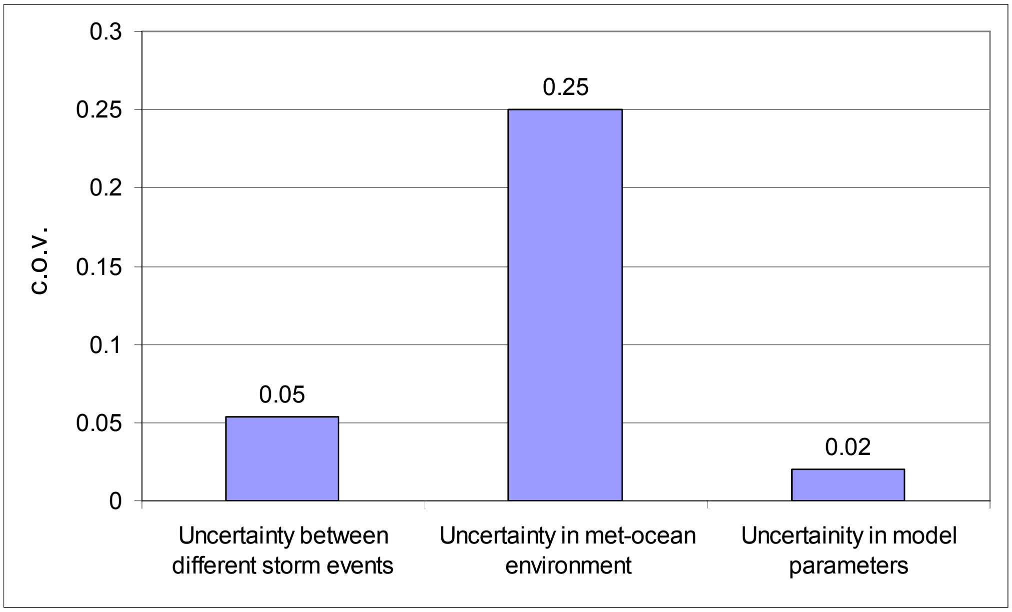

**Figure 6.15:** Comparison of coefficient of variation values for individual components of uncertainty in hurricane loads

# 7. Line and Foundation Loads

## 7.1 Line Load

The line loads at the fairlead are shown on Figure 7.1 and summarized in Table 7.1 for the design hurricane event. Both intact and damaged conditions in three different water depths are shown in Figure 7.1. The variation in the loads for both intact and damaged conditions is larger for the 3000-ft water depth than for the other water depths. The loads are shared more evenly between the lines in the taut mooring systems (6,000 and 10,000 ft water depths), particularly in the damage cases. This same information is shown on Figure 7.2 and in Table 7.2 for the design loop current event. Table 7.3 provides a summary of the nominal design loads for the most heavily loaded lines compared to the median loads in a 20-year design life due to hurricanes or loop currents.

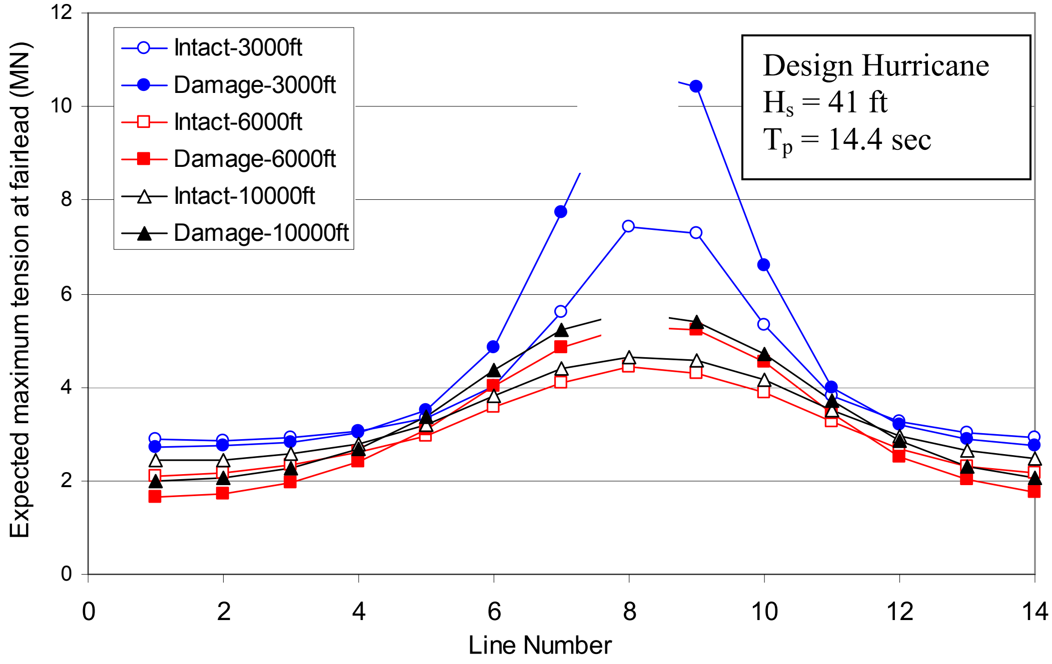

Figure 7.1: Expected maximum line loads in a 3-hour sea state versus line number for design hurricane event

Table 7.1: Nominal line load at the fairlead under hurricane conditions

| Water Depth (ft) | Mooring Condition | Nominal Line Load (kips) |
|---|---|---|
| 3,000 | Intact | 1609 |
| | Damage | 2314 |
| 6,000 | Intact | 897 |
| | Damage | 1052 |
| 10,000 | Intact | 1046 |
| | Damage | 1214 |

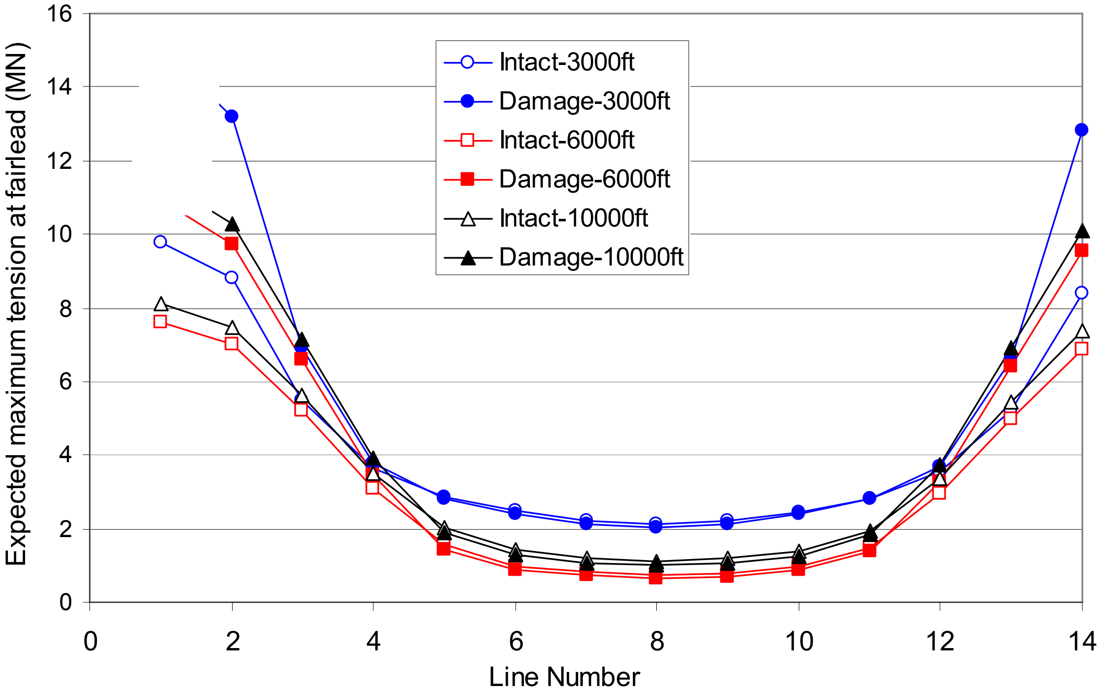

Figure 7.2: Expected maximum line loads in a 3-hour sea state versus line number for design loop current event

Table 7.2: Nominal line load at the fairlead in three water depths under loop current conditions

| Water Depth (ft) | Mooring Condition | Nominal Line Load (kips) |
|---|---|---|
| 3,000 | Intact | 2148 |
| | Damage | 3022 |
| 6,000 | Intact | 1621 |
| | Damage | 2121 |
| 10,000 | Intact | 1739 |
| | Damage | 2242 |

Table 7.3: Comparison of the ratio of median to nominal design line loads in three water depths under different environmental conditions

| Environmental Condition | Water depth (ft) | $\text{load}_{median}/\text{load}_{design}$ |
|---|---|---|
| Hurricane | 3,000 | 0.50 |
| | 6,000 | 0.73 |
| | 10,000 | 0.75 |
| Current (Weibull) | 3,000 | 0.70 |
| | 6,000 | 0.72 |
| | 10,000 | 0.72 |
| Current (Type II) | 3,000 | 0.63 |
| | 6,000 | 0.69 |
| | 10,000 | 0.71 |

The line loads on the most heavily loaded line and corresponding angles at the mudline during the hurricane event with the same sea states as for Figure 7.1 in three different water depths are compared and plotted in Figure 7.3. The different behaviors between the semi-taut system in 3,000 ft of water and the taut systems in 6,000 ft and 10,000 ft of water are well illustrated in this figure. The taut systems have a constant angle at the mudline of about 35° while the semi-taut system has a range from 13° to 26°.

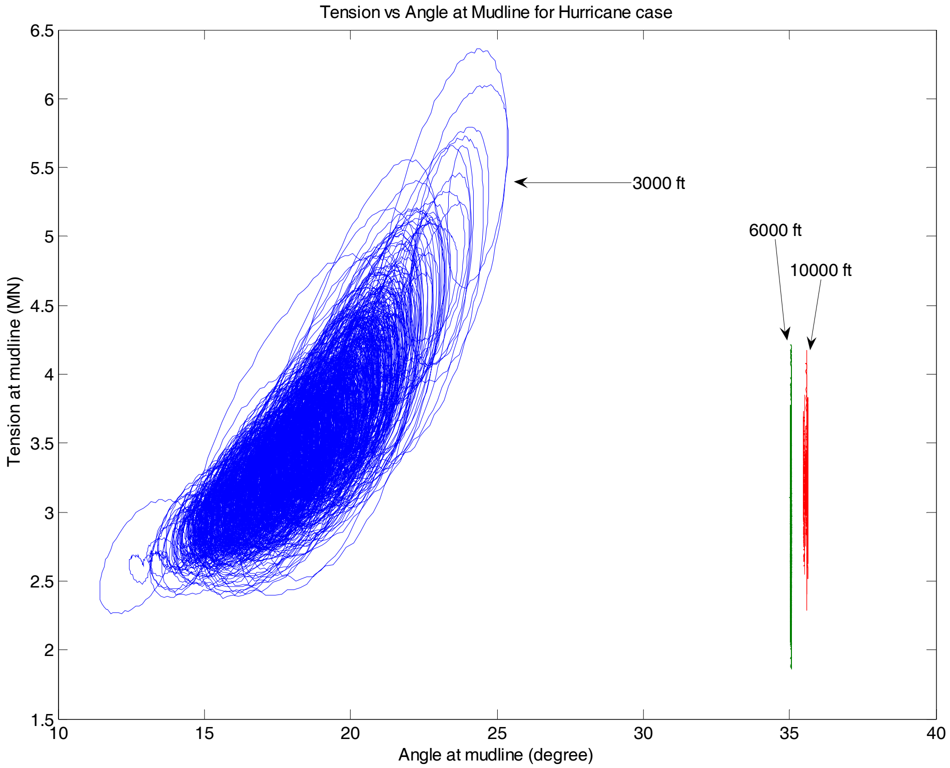

Figure 7.3: Comparison of tensions and angles at mudline in three different water depths for hurricane intact case (with $H_s$=41 ft and $T_p$=14.4 sec).

The time-varying loads and the corresponding angles at the mudline during a loop current event are shown in Figure 7.4. Note that during a loop current event the most heavily loaded mooring line is line #1. The variation in the line load is also smaller for the loop current event than that for the hurricane event. Since the change in the angle and load on line #1 is negligible, the load at the mudline may be considered as a static load. This behavior is also reflected in the time variation in the angle and loads at the mudline (Figure 7.5), and in the relationship between tension and angle (Figure 7.6).

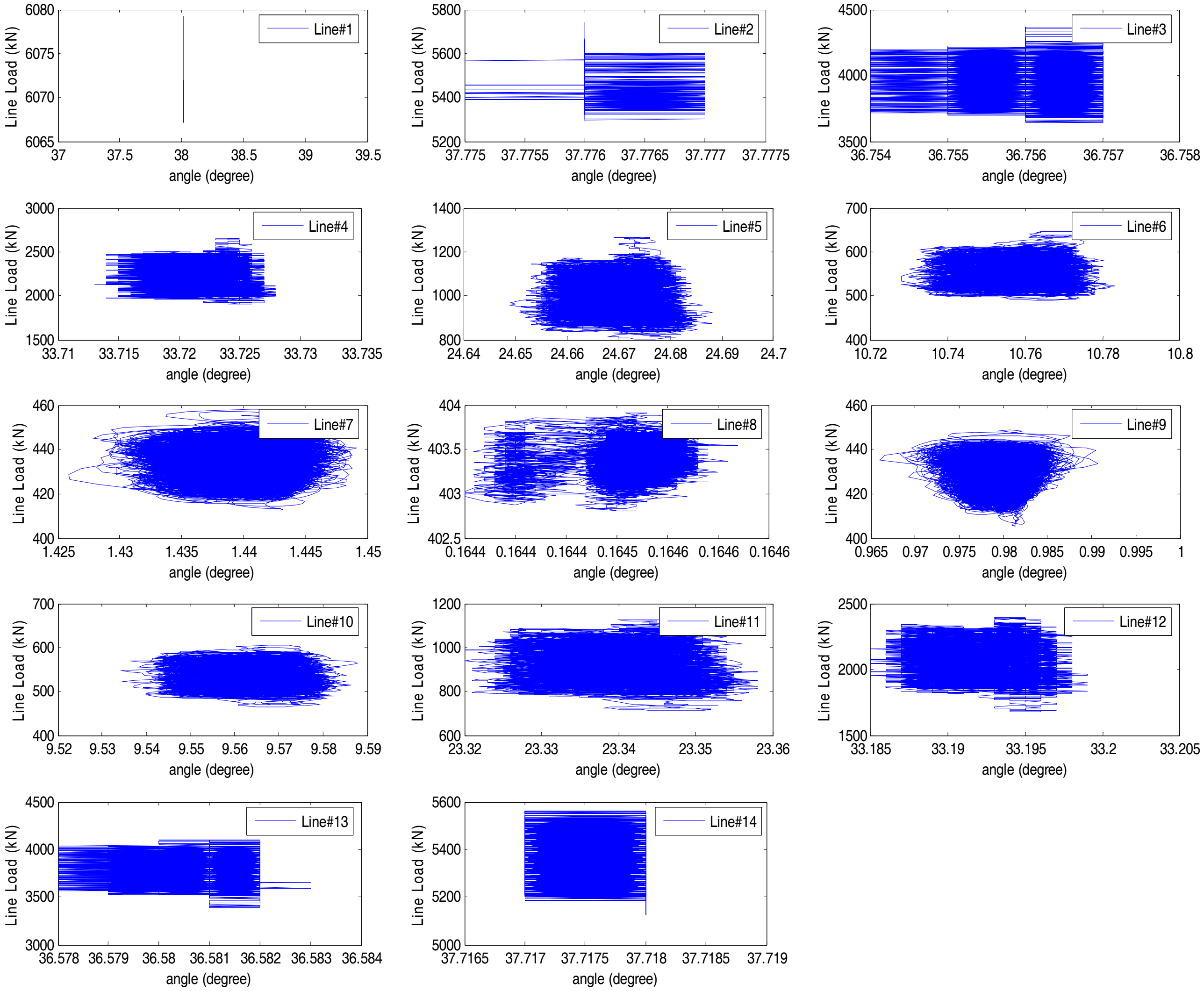

Figure 7.4: Time varying line load vs. angle at the mudline (with Vmax =6.63 ft/s in a 6000-ft water depth)

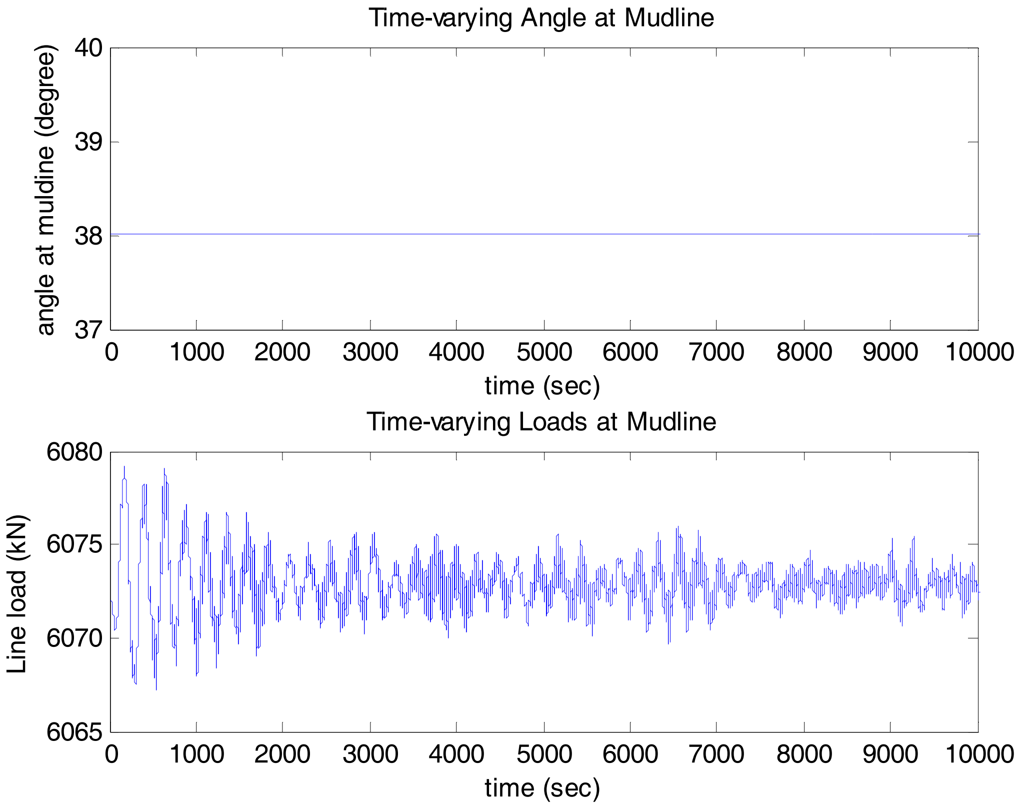

Figure 7.5: Time-varying load and angle in line #1 at the mudline (with $V_{max}$ = 6.63 fps in a 6000-ft water depth)

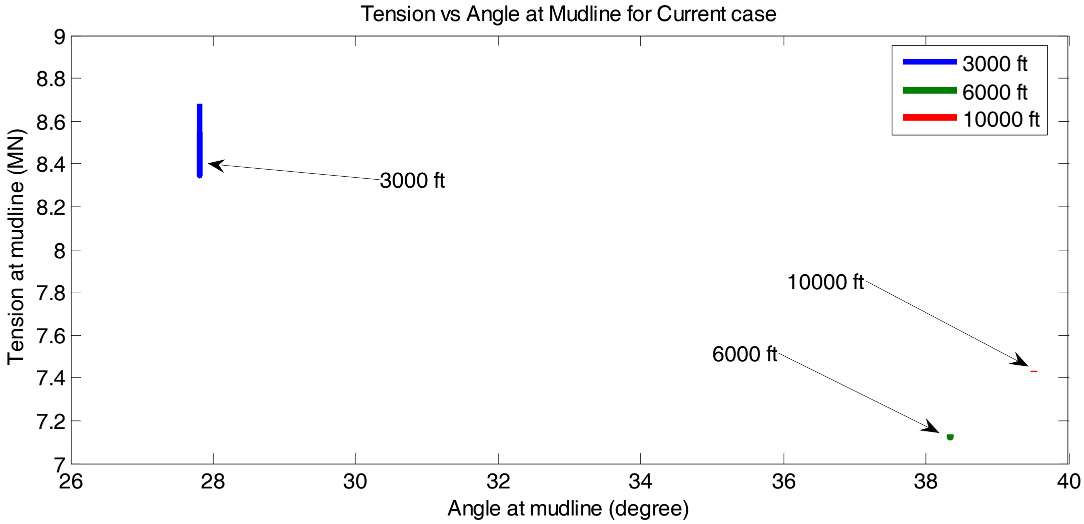

Figure 7.6: Comparison of tensions and angles in three different water depths for current intact case (with $V_{max}$ = 7.2 fps)

### 7.2 Foundation Load

The foundation for each mooring line is a suction caisson with a length-to-diameter ratio of 6 and a padeye that is located at two-thirds of the penetration depth below the mudline. The size of a suction caisson can be determined based on the factored foundation design load which is affected by mooring line loads in the extreme environmental conditions.

#### 7.2.1 Generic Soil Profile in the GOM

Figure 7.7 shows a generic soil profile from the Gulf of Mexico consisting of soft clay deposits. Typical clays in the Gulf of Mexico are normally and slightly overconsolidated, with plastic limit (PL) of about 25 and liquid limit (LL) of approximately 70 (Gilbert and Murff 2001b). Since this is representative of conditions currently being encountered for deepwater application in the GOM, this generic soil profile and soil type have been used for designing suction caissons subjected to extreme environmental loadings and identifying uncertainties in the suction caisson loads in later sections of this report.

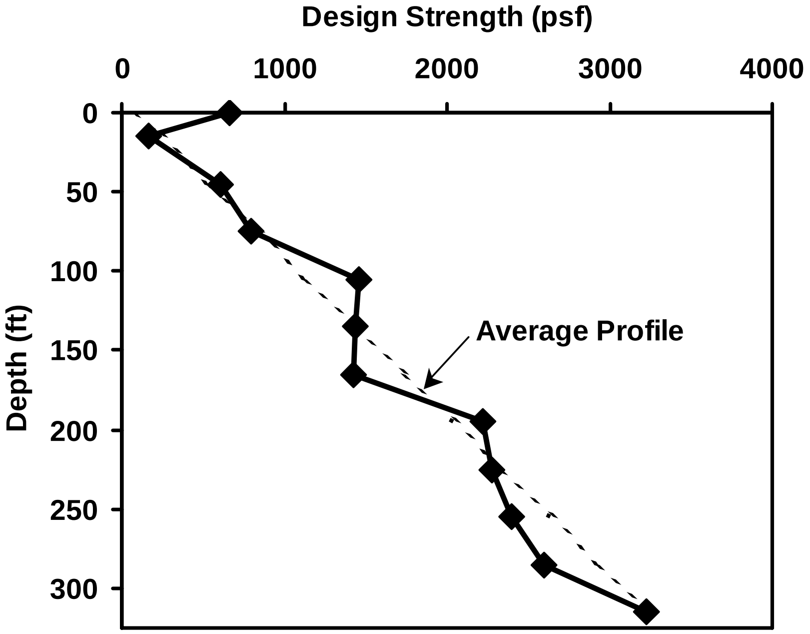

Figure 7.7: Generic Soil Profile in the Gulf of Mexico

#### 7.2.2 Interaction among Mooring Lines, Caisson and Seabed Soils

Figure 7.8 shows conceptually how the line angle varies below the mudline. The foundation loads at the padeye are different in both magnitude and direction from the loads of the corresponding mooring line at the mudline. The foundation loads are smaller than the mooring line loads, and the loading angle at the padeye is larger than the loading angle at the mudline. This discrepancy is due to soil resistance, resulting in inverse-catenary mooring line shapes as shown in Figure 7.8 (Degenkamp and Dutta 1989; Gault and Cox 1974; Neubecker and Randolph 1995; Reese 1973; Vivatrat et al. 1982).

This change in shape and load is due to soil-chain friction acting tangentially to the chain and bearing resistance acting normally to the chain. The soil around the chain is assumed to fail similarly to a strip footing with a loading direction perpendicular to the chain (Degenkamp and Dutta 1989). Gault and Cox (1974) observed that the soil resistance normal to the chain has little influence on the total load transferred to the padeye but has a greater influence on the direction of a line.

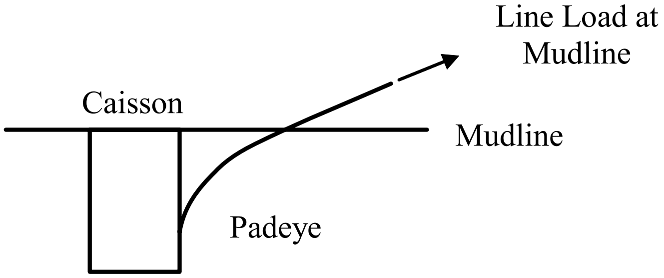

Figure 7.8: Line catenary below mudline

Vivatrat et al. (1982) derived a governing differential equation for the padeye load considering both chain self weight and the tangential soil resistance. The use of a self-weight term in the differential equation made the solution more complicated, so numerical integration of the equation was needed. Accordingly iteration was needed to meet the boundary conditions for the solution to the governing differential equation.

Neubecker and Randolph (1995) proposed an analytical solution for the tension and loading angle at the padeye by neglecting the chain self weight, as the effect of the chain self weight was significant only at shallow embedment depth. The analytical equations are expressed by:

$$\frac{T_a}{2}(\theta_a^2-\theta_o^2)=DQ_{avg} \text{ and } \qquad \frac{T_o}{T_a}=\exp(f*\theta_a) \qquad (7.1)$$

where $T_a$ and $T_o$ are tensions at the padeye and mudline, $\theta_a$ and $\theta_o$ are angles at the padeye and mudline respectively, D is a depth of padeye from mudline, $Q_{avg}$ is the average normal force to the chain below mudline, and f is a friction coefficient for seabed soils.

Although Equation 7.1 also requires iteration to estimate $T_a$ and $\theta_a$, the analytical solution is preferred to the differential solution because there is no need to integrate the governing equation along the length of chain below the mudline. The analytical solution also provides direct insight into chain performance, as discussed in the next section. Once $T_a$ and $\theta_a$ are calculated using Equation 7.1 with the load and angle at the mudline, the vertical and horizontal components of $T_a$ can be determined.

### 7.2.3 Parametric Study on Padeye Loads

A sensitivity analysis was performed to obtain direct insight into the padeye load. Four parameters affect loads at the padeye: (1) the undrained shear strength $S_{uo}$ of soil at the mudline; (2) the rate of strength increase with depth $S_{u1}$; (3) the friction coefficient between soil and chain *f*; and (4) the soil bearing factor $N_c$. The sensitivities of the chain solution for the transferred tension load ($T_a$) and corresponding angle ($\theta_a$) at the padeye, vertical component load ($T_{av}$) and horizontal component load ($T_{ah}$) of $T_a$ to these four variables are shown in Figure 7.9. The sensitivity study was performed by varying one of the parameters while holding the other three constant.

The effect of the parameters on the loads and corresponding angle at the padeye can be seen from Figure 7.9. A positive increase means that an increase in the parameter under consideration causes an increase in the solution value. For example, as $N_c$ increases, the transferred tension load ($T_a$) at the padeye decreases. The transferred tension load at the padeye is most sensitive to the friction coefficient, *f*. $N_c$ is also an important factor because the bearing resistance also affects the angle resulting in change in the vertical and horizontal load at the padeye. Both $N_c$ and $S_{u1}$ have an effect because they are related to the undrained capacity of the strip loading. It is also observed from Figure 7.9 that the friction coefficient has a negative effect on both the vertical component and the horizontal component and all four parameters have a negative effect on $T_a$ and $T_{ah}$.

$N_c$ and $S_{u1}$ have a greater effect on the angle at the padeye, while the friction coefficient has less of an impact on the angle. In a semi-taut mooring system, a general range of angles at mudline is between 25° and 35°. The angles will increase by 4° to 8° as the mooring chain is getting deeper due mainly to the $N_c$, resulting in an increase in $T_{av}$ but a decrease in $T_{ah}$.

With Equation 7.1 and the generic soil properties, the effect of an angle at the mudline on the vertical component of the load at the padeye was investigated, as shown in Figure 7.10. The load at the mudline is varied with a constant angle of either 0° or 35° at the mudline, and the vertical component at the padeye is calculated using Equation 7.1. For the semi-taut and taut systems in which the angles at the mudline range from 25° to 38° (see Figures 7.3 and 7.6), the vertical component becomes more important for suction caisson design. Figure 7.11 shows an example calculation for $T_{av}$ plotted with tension at the mudline.

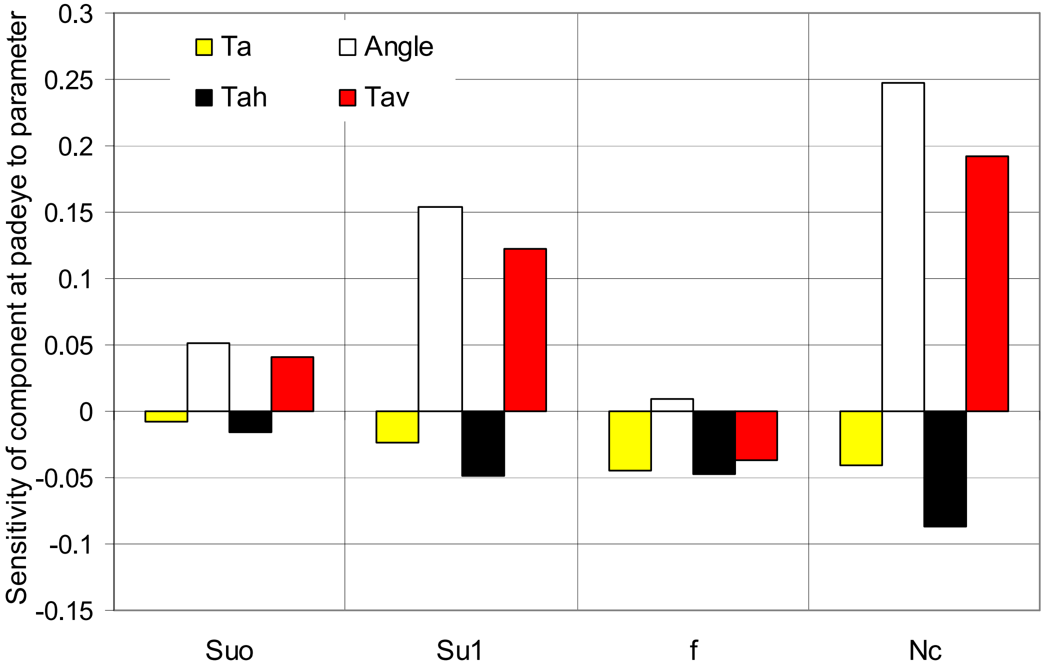

Figure 7.9: Parametric study for loads and angle at the padeye

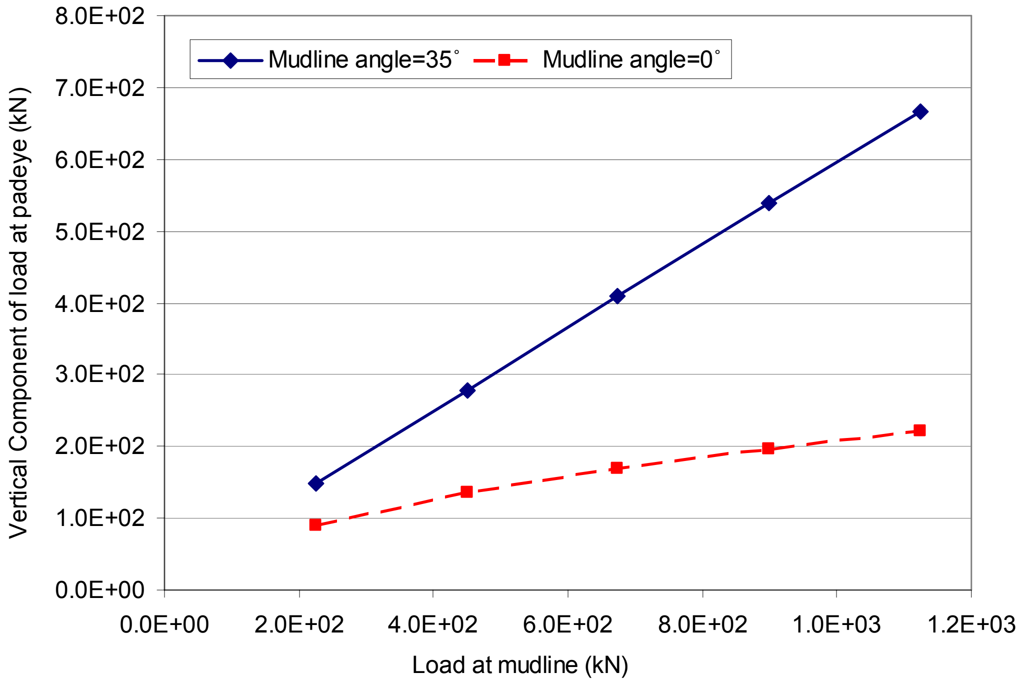

Figure 7.10: Comparison of vertical components of loads at padeye given two different mudline angles

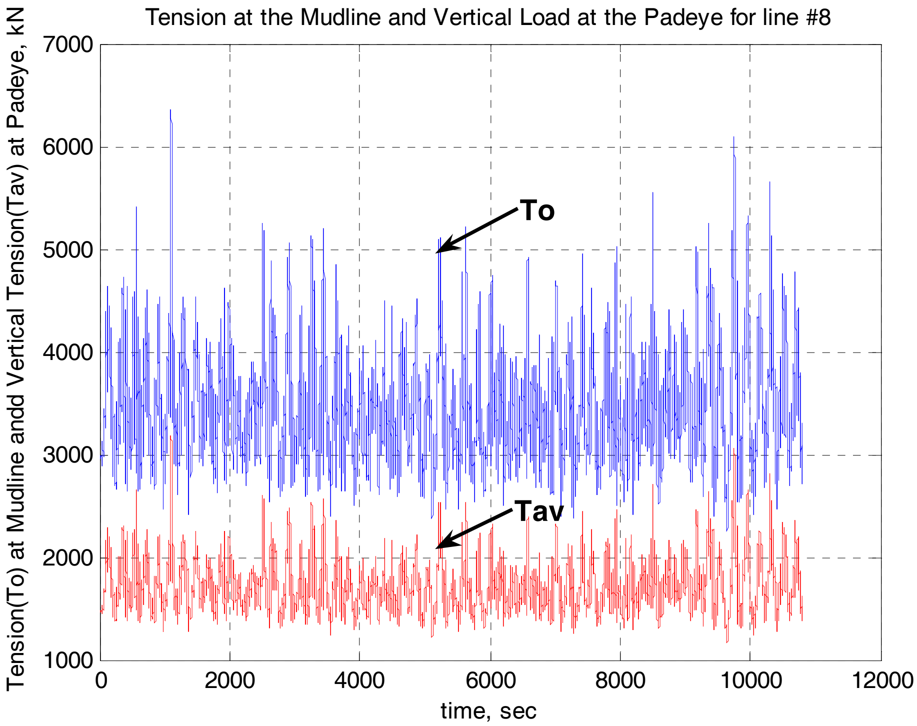

Figure 7.11: Comparison of tension at mudline and vertical component at padeye for line #8 in 3000-ft water depth during a 3-hr storm event

### 7.2.4 Nominal foundation loads

Using the above information, the foundation loads at the padeye can be estimated and summarized in Tables 7.4 and 7.5 for the design hurricane event and the design loop current event, respectively. Table 7.6 provides a summary of the design loads for the most heavily loaded foundations compared to the median loads in a 20-year design life due to hurricanes or loop currents.

Table 7.4: Nominal foundation load at the padeye in three water depths under hurricane conditions

| Water Depth (ft) | Mooring Condition | Nominal Foundation Load (kips) |
|---|---|---|
| 3,000 | Intact | 675 |
| | Damage | 1086 |
| 6,000 | Intact | 519 |
| | Damage | 622 |
| 10,000 | Intact | 590 |
| | Damage | 704 |

Table 7.5: Nominal foundation load at the padeye in three water depths under loop current conditions

| Water Depth (ft) | Mooring Condition | Nominal Foundation Load (kips) |
|---|---|---|
| 3,000 | Intact | 978 |
| | Damage | 1444 |
| 6,000 | Intact | 1000 |
| | Damage | 1322 |
| 10,000 | Intact | 1063 |
| | Damage | 1399 |

Table 7.6: Comparison of the ratio of median to design foundation loads in three water depths under different environmental conditions for the case of $FS_{intact} = 2.5$

| Environmental Condition | Water depth (ft) | $load_{median}/load_{design}$ |
|---|---|---|
| Hurricane | 3,000 | 0.41 |
| | 6,000 | 0.70 |
| | 10,000 | 0.71 |
| Current (Weibull) | 3,000 | 0.60 |
| | 6,000 | 0.69 |
| | 10,000 | 0.70 |
| Current (Type II) | 3,000 | 0.59 |
| | 6,000 | 0.68 |
| | 10,000 | 0.69 |

# 8. Line and Foundation Capacities

## 8.1 Line Capacity

### 8.1.1 Factored Loads for Design

Using the design cases for intact and damaged conditions, the nominal (design) line capacity can be calculated with a factor of safety of 1.67 (for intact conditions) and 1.25 (for damaged conditions). These factors of safety are prescribed by the API code. Of the two factored line loads, the larger factored line load was considered as the nominal line capacity. Note that the design sea state is $H_s$ =12.5 m and $T_p$ = 14.4 sec for a hurricane event and $V_{max}$ = 7.0 fps at water surface for a loop current event. It should also be noted that a range of factors of safety has been used in practice as shown in Table 8.1. For example, in the semi-taut system where a mooring line composes of top and bottom chains and wire rope, the intact factor of safety ranges from 1.5 to 2.0 while the damaged factor of safety ranges from 1.1 to 1.65. For the taut systems consisting of top and bottom chains and polyester rope, the factor of safety is typically increased by 0 to 20 % in practice because of the lack of field and laboratory experience and as it is a recently adopted technique. For this study, API's factors of safety were used in the semi-taut and taut mooring systems.

Table 8.1: Comparison of factors of safety for mooring line design for intact and damaged conditions used in different design codes

| Material | Factor of Safety | | Comment | Reference |
|---|---|---|---|---|
| | Design Condition | Equivalent FS | | |
| Wire | Intact | 1.67 | API RP 2SK | API (1997b) |
| | Damaged | 1.25 | | |
| | Intact | 1.67 | API RP-2FPS | Bruen et al. (1991) |
| | Damaged | 1.33 | | |
| | Intact | 1.7 | Calibrated FS based on a target reliablity | Goodwin et al. (2000) |
| | Damaged | 1.65 | | |
| | Intact | 1.5 | Intact only (p354) | Larsen (1996) |
| | Damaged | N/A | | |
| | Intact | 1.6 | Calibrated FS based on a target reliablity | Ahilan et al. (1996) |
| | Damaged | 1.35 | | |
| | Intact | 1.5 | DNV POSMOOR | |
| | Damaged | 1.1 | | |
| | Intact | 1.85 | Lloyds FPS | |
| | Damaged | 1.35 | | |
| | Intact | 1.65 | NMD FPS | |
| | Damaged | 1.25 | | |
| | Intact | 2 | Norwegian Petroleum Directorate (NPD) | |
| | Damaged | 1.4 | | |
| | Intact | 1.8 | IACS | |
| | Damaged | 1.25 | | |
| Polyester | Intact Damaged | Increase FSs by ~9 % | American Bureau of Shipping (ABS) | Bhat et al. (2002) |
| | | Increase FSs by 10 % | Det Norske Veritas (DNV) | |
| | | Increase FSs by 20 % | Bureau Veritas (BV) | |
| | | Increase FSs by 0 % | American Petroleum Institute (API) | |
| | | 20 % increase | Used for the Mad Dog project (practical example) | Petruska et al. (2005) |

The required line capacity was determined using factors of safety of 1.67 (intact) and 1.25 (damaged) for the hurricane (Table 8.2) and the loop current (Table 8.3). The required nominal capacity is equal to the factor of safety multiplied by the nominal load. The governing design condition is then determined by choosing the larger nominal capacity between the two cases, intact and damaged system, in each water depth. The governing condition is indicated in Table 8.2 for each spar design.

Table 8.2: Nominal line capacity and design governing case under hurricane conditions

| Water Depth (ft) | Mooring Condition | Factor of Safety | Nominal Line Load (kips) | Nominal Line Capacity (kips) | Governing Condition |
|---|---|---|---|---|---|
| 3,000 | Intact | 1.67 | 1609 | 2687 | |
| | **Damage** | **1.25** | **2314** | **2892** | √ |
| 6,000 | **Intact** | **1.67** | **897** | **1498** | √ |
| | Damage | 1.25 | 1052 | 1314 | |
| 10,000 | **Intact** | **1.67** | **1046** | **1747** | √ |
| | Damage | 1.25 | 1214 | 1518 | |

Table 8.3: Nominal line capacity and design governing case under loop current conditions

| Water Depth (ft) | Mooring Condition | Factor of Safety | Nominal Line Load (kips) | Nominal Line Capacity (kips) | Governing Condition |
|---|---|---|---|---|---|

| | | | | | |
|---|---|---|---|---|---|
| 3,000 | Intact | 1.67 | 2148 | 3587 | |
| | **Damage** | **1.25** | **3022** | **3777** | √ |
| 6,000 | **Intact** | **1.67** | **1621** | **2708** | √ |
| | Damage | 1.25 | 2121 | 2651 | |
| 10,000 | **Intact** | **1.67** | **1739** | **2905** | √ |
| | Damage | 1.25 | 2242 | 2802 | |

Note that the original spar design developed by Deepstar did not include loop current loading. For the purposes of the reliability analyses, we have assumed that either the hurricane loading or the loop current loading governs the design. Specifically, we first assumed that hurricane loading governs the design and evaluate the reliability considering only the occurrence of hurricanes. We then repeat the reliability analysis by assuming that the loop current loading governs the design and evaluate the reliability considering only the occurrence of loop currents. This approach is reasonable providing that the governing loading condition is dominant. Since greater capacities are required for this spar design with loop current loading, we assumed that the line capacity could be scaled up without significantly affecting the hydrodynamic response (that is, the larger line weights and diameters needed for the loop current do not affect the load response).

### 8.1.2 Models for Line Capacity

Individual lines consist of an upper chain segment, a wire or polyester rope segment and then a lower chain segment.

#### 8.1.2.1 Model for Chains

The final strength of a typical mooring chain depends on the strength of the weakest link among the links (Bush et al. 1992). For practical purposes, the mooring analysis and design may be performed based on a test break strength specified by manufactures (Luo and Ahilan 1992). A chain strength model proposed by Luo and Ahilan (1992) and Bush et al. (1992) is incorporated in this study as follows:

1. Assuming that the strength of individual links is statistically independent and follows the normal distribution, the probability distribution function of the strength of the weakest link out of n links is given by:

   $$F(y) = 1 - [1 - F_i(y)]^n \tag{9.6}$$

   Where $F(y)$ is the cumulative distribution function of y; $F_i(y)$ is the cumulative distribution function of the strength of individual link; and n is the number of links.
2. As n increases infinitely, Equation 9.6 converges to the asymptotic extreme value distribution (Type I smallest), which may be considered to be accurate as long as n is large enough. For more details for the asymptotic distribution and parameters such as mean and variance, refer to (Ang and Tang 1975b).

3. Based on limited breaking test data, the mean breaking strength ($\mu_{link}$) of links is 1.25 times larger than the nominal break load (BTL), which is set equal to the required nominal capacity of the mooring line.
4. Assuming that the material used in mooring systems of high quality under good quality control, use of a 10% coefficient of variation ($\delta_{link}$) is considered reasonable given the limited full-scale test data (Bruen et al. 1991; Bush et al. 1992; Luo and Ahilan 1992).
5. All links are loaded to the chain proof load of 70% of BTL during manufacturing certification processes. Therefore, in the calculation of the reliability, the proof load can be considered as a minimum capacity of the chain segments. If variations in the chain capacity have more to do with handling before and during installation but after testing, then this proof load is not necessarily an appropriate lower bound. While it has been included in these reliability analyses, it does not have a significant effect on the overall results.
6. During manufacturing of the chain, it is recommended that a test specimen consisting of at least four links is loaded to perform break tests (API 1997a). Based on this recommendation, the total number of links of the chain segments, n in Equation 9.6, is divided by 4 to reflect that systems of 4 links are actually tested and essentially comprise a single link for the purpose of reliability.

#### 8.1.2.2 Model for Wire and Polyester Ropes

The model for the capacity of the wire and polyester ropes was based on the work of Bruen et al. (1991), Ahilan et al. (1996), Goodwin et al. (1999) and Snell et al. (1999) and Goodwin et al. (2000). The required nominal design capacity is set equal to the Catalog Break Strength (CBS). The capacity is assumed to have a lognormal distribution, with a mean value that is 1.1 times the CBS value and a coefficient of variation equal to 0.15. The same model is assumed for both the polyester and the wire rope.

## 8.2 Foundation Capacity

### 8.2.1 Factored Loads for Design

Based on the nominal foundation loads, the nominal foundation capacities can be determined with a typical factor of safety ranging from 2 to 3 for intact conditions and 1.5 to 2.5 for damaged conditions while there are variations in design practice for suction caisson. These required nominal capacities are summarized in Tables 8.4 to 8.6 for hurricane conditions and Tables 8.7 to 8.9 for loop current conditions.

Table 8.4: Nominal foundation capacity and design governing case under hurricane conditions with an intact factor of safety of 2.0

| Water Depth (ft) | Mooring Condition | Factor of Safety | Nominal Foundation Load (kips) | Nominal Foundation Capacity (kips) | Governing Condition |
|---|---|---|---|---|---|
| 3,000 | Intact | 2.0 | 675 | 1349 | |
| | **Damage** | **1.5** | **1086** | **1630** | √ |
| 6,000 | **Intact** | **2.0** | **519** | **1039** | √ |
| | Damage | 1.5 | 622 | 933 | |
| 10,000 | **Intact** | **2.0** | **590** | **1180** | √ |
| | Damage | 1.5 | 704 | 1056 | |

Table 8.5: Nominal foundation capacity and design governing case under hurricane conditions with an intact factor of safety of 2.5

| Water Depth (ft) | Mooring Condition | Factor of Safety | Nominal Foundation Load (kips) | Nominal Foundation Capacity (kips) | Governing Condition |
|---|---|---|---|---|---|
| 3,000 | Intact | 2.5 | 675 | 1687 | |
| | **Damage** | **2.0** | **1086** | **2173** | √ |
| 6,000 | **Intact** | **2.5** | **519** | **1298** | √ |
| | Damage | 2.0 | 622 | 1245 | |
| 10,000 | **Intact** | **2.5** | **590** | **1475** | √ |
| | Damage | 2.0 | 704 | 1408 | |

Table 8.6: Nominal foundation capacity and design governing case under hurricane conditions with an intact factor of safety of 3.0

| Water Depth (ft) | Mooring Condition | Factor of Safety | Nominal Foundation Load (kips) | Nominal Foundation Capacity (kips) | Governing Condition |
|---|---|---|---|---|---|
| 3,000 | Intact | 3.0 | 675 | 2024 | |
| | **Damage** | **2.5** | **1086** | **2716** | √ |
| 6,000 | **Intact** | **3.0** | **519** | **1558** | √ |
| | Damage | 2.5 | 622 | 1556 | |
| 10,000 | **Intact** | **3.0** | **590** | **1770** | √ |
| | Damage | 2.5 | 704 | 1760 | |

Table 8.7 : Nominal foundation capacity and design governing case under loop current conditions with an intact factor of safety of 2.0

| Water Depth (ft) | Mooring Condition | Factor of Safety | Nominal Foundation Load (kips) | Nominal Foundation Capacity (kips) | Governing Condition |
|---|---|---|---|---|---|
| 3,000 | Intact | 2.0 | 978 | 1955 | |
| | **Damage** | **1.5** | **1444** | **2166** | √ |
| 6,000 | **Intact** | **2.0** | **1000** | **2000** | √ |
| | Damage | 1.5 | 1322 | 1984 | |
| 10,000 | **Intact** | **2.0** | **1063** | **2126** | √ |
| | Damage | 1.5 | 1399 | 2099 | |

Table 8.8: Nominal foundation capacity and design governing case under loop current conditions with an intact factor of safety of 2.5

| Water Depth (ft) | Mooring Condition | Factor of Safety | Nominal Foundation Load (kips) | Nominal Foundation Capacity (kips) | Governing Condition |
|---|---|---|---|---|---|
| 3,000 | Intact | 2.5 | 978 | 2444 | |
| | **Damage** | **2.0** | **1444** | **2888** | √ |
| 6,000 | Intact | 2.5 | 1000 | 2501 | |
| | **Damage** | **2.0** | **1322** | **2645** | √ |
| 10,000 | Intact | 2.5 | 1063 | 2658 | |
| | **Damage** | **2.0** | **1399** | **2798** | √ |

Table 8.9: Nominal foundation capacity and design governing case under loop current conditions with an intact factor of safety of 3.0

| Water Depth (ft) | Mooring Condition | Factor of Safety | Nominal Foundation Load (kips) | Nominal Foundation Capacity (kips) | Governing Condition |
|---|---|---|---|---|---|
| 3,000 | Intact | 3.0 | 978 | 2933 | |
| | **Damage** | **2.5** | **1444** | **3611** | √ |
| 6,000 | Intact | 3.0 | 1000 | 3001 | |
| | **Damage** | **2.5** | **1322** | **3306** | √ |
| 10,000 | Intact | 3.0 | 1063 | 3190 | |
| | **Damage** | **2.5** | **1399** | **3498** | √ |

### 8.2.2 Model for Foundation Capacity

#### 8.2.2.1 Predicted Foundation Capacity

Foundation capacity depends on the soil profile, caisson geometry, loading angle at padeye, and the location of the attachment point (i.e., the depth of padeye below mudline).

Due to these factors, failure mechanisms for a suction caisson can be different depending on various combinations of these factors from pure vertical failure mechanism and pure horizontal failure mechanism to interaction failure mechanism (Clukey et al. 2003).

Axial capacity of a suction caisson anchor is equal to the sum of caisson weight ($W_c$), soil plug weight ($W_p$), external side friction ($Q_f$), reverse end bearing ($R_c$) and overburden ($Q_o$) as shown in Equation 8.1.

$$R = W_c + W_p + Q_f + R_c - Q_o \tag{8.1}$$

The method of estimating the axial capacity of a suction caisson with a given geometry and soil profile can be found more detail in Luke (2002). In driven pile foundations, the skin friction component along the embedded depth of the piles provides most of the axial pile capacity (API 1993), whereas, for the suction caisson foundations, both the skin friction and the end bearing components provide most of the total caisson capacity (Clukey et al. 2000). However, it should be noted that, for the suction caisson foundation, the direction of the skin friction is opposite the direction of load. For the driven piles, the end bearing resistance acts upward but is a negligible value; however, for the suction caisson foundations, it acts downward. The end bearing resistance is an important value in addition to skin friction resistance for the suction caisson foundations (Gilbert and Murff 2001a). The submerged self-weight of the suction caisson also affects a small part of the total axial capacity. Plug weight and overburden weight are usually assumed to cancel one another.

The lateral capacity was estimated using the method developed by Murff and Hamilton (1993) and assuming a gap on the back side and a rough interface with the caisson wall.

Interaction between vertical and horizontal capacity for a suction caisson anchor has been studied using the upper bound method of plasticity theorem (Aubeny et al. 2003a, b and Clukey et al. 2003). Using SAIL (Suction caisson Analysis Under Inclined Load) program developed by Aubeny et al (2003a, b), an optimum attachment-depth ratio with a general range of load angles at the padeye is shown in Figure 8.1. Denoting $L_i$ as the depth of the padeye and $L_f$ as the embedded length of a suction caisson, the optimum attachment depth ratio is approximtaly two thirds of the length of a suction caisson. This finding is similar to that of other researchers (Clukey et al. 2003; Aubeny et al. 2003a, b). Accordingly, a padeye depth ratio of 0.65 has been used in this study. The friction coefficient, $\alpha$, used in Figure 8.1 is 0.9, which is less than unity. The interaction curve for combined loading conditions with $L_f/B=6$ and three different diameters of the suction caisson, B=12 ft, 13 ft and 14 ft is shown in Figure 8.2. B is the diameter of the suction caisson and $L_f$ is the embedded length of the caisson. From Figure 8.2, the design values of the ultimate combined capacity can be obtained. For the case where the diameter of the suction caisson is 13 ft, the pure vertical capacity is about 2050 kips and the pure horizontal capacity is about 4600 kips. This is more than 2 times greater than the pure vertical capacity. El-Sherbiny et al. (2005) reveals that suction caissons subjected to inclined loads fail only by uplift, as long as the angle at the padeye is greater than about 35 degrees. For the study systems including the semi-taut system under hurricane and loop current conditions, the angle at the mudline ranges from 28 and 38 degrees (Figures 7.3 and 7.6) and the padeye angles have a range of 35 to 45 degrees. For the study spar, foundation design is governed by vertical capacity.

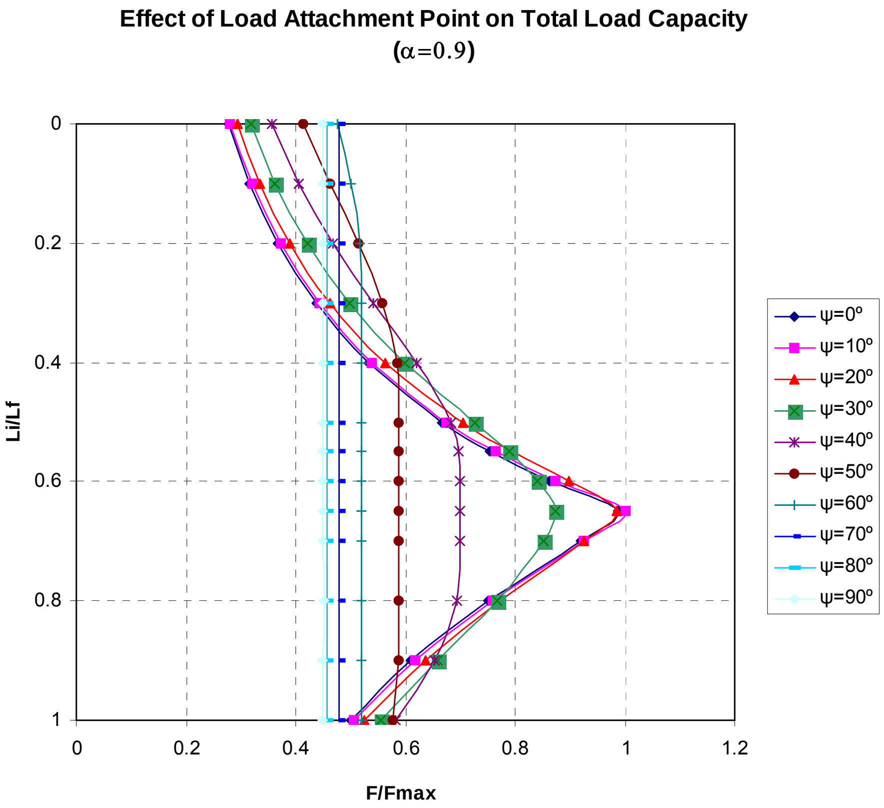

Figure 8.1: Effect of load attachment point (padeye) on total load capacity

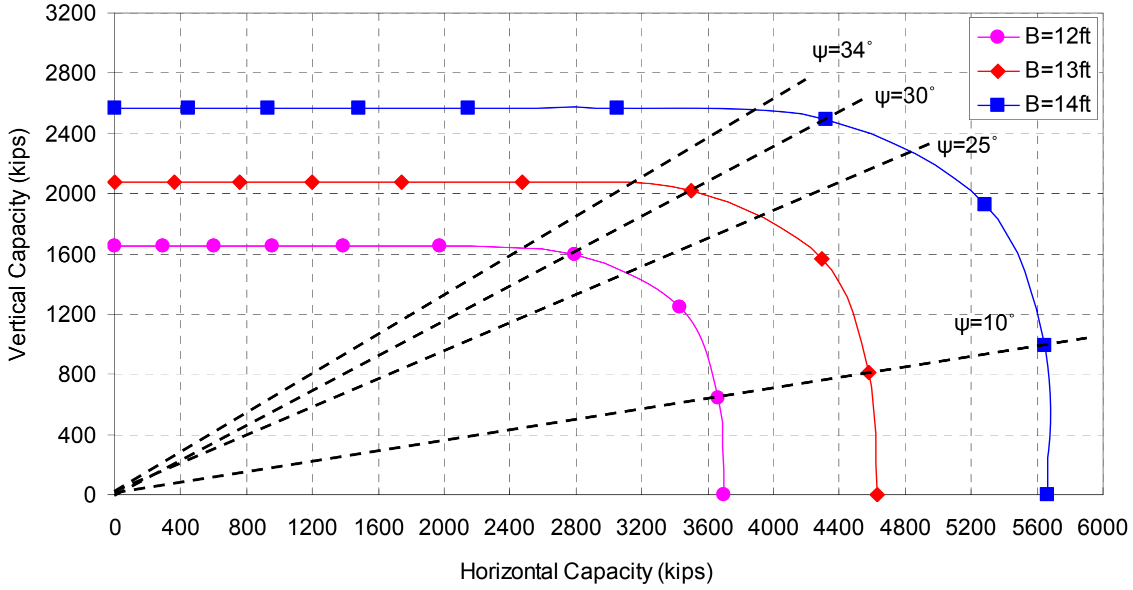

Figure 8.2: Interaction curve for capacity of suction caissons

### 8.2.2.2 Bias and c.o.v. Values for Predicted Foundation Capacity

A database comprised of published load tests was assembled and used to evaluate biases and uncertainties in models for predicting the uplift capacity of suction caissons in normally consolidated clays. This database of 25 tests taken includes the following: laboratory-scale model tests (Luke et al. 2003), centrifuge tests (Clukey et al. 2003; Clukey and Morrison 1993; Clukey and Phillips 2002; House and Randolph 2001; Randolph and House 2002), and full-scale field tests (Cho et al. 2003).

For the purposes of a preliminary analysis, the predicted capacities in each test were calculated using the model developed by Aubeny et al. (2003a, b) with an $\alpha$ value of 1.0 for side friction and a bearing capacity factor of 9.0 for the reverse end bearing. Shear strengths reported by each investigator were used directly. Refer to Najjar (2005) for details of this analysis. Ratios of measured to predicted capacities for the 25 tests in the database are plotted on Figure 8.3.

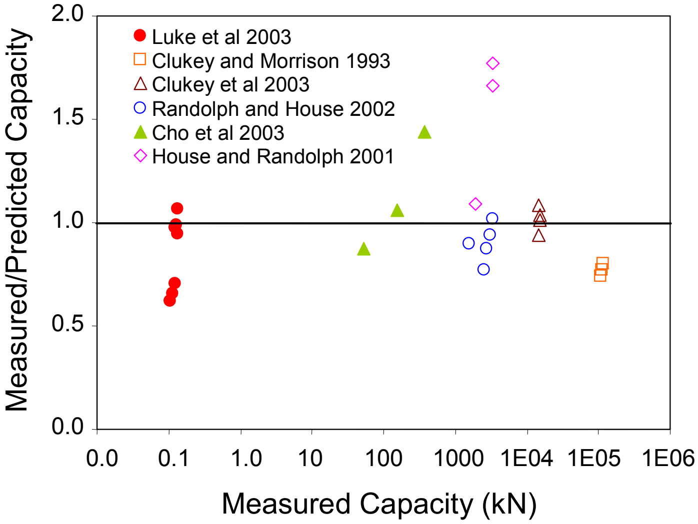

Figure 8.3: Measured versus predicted axial capacity for model tests on suction caissons in normally consolidated clays (from Shadi (2005)).

The average value for the ratio of measured to predicted capacity on Figure 8.3 is 0.99, indicating an unbiased prediction model. A more careful analysis was performed on a set of laboratory-scale model tests that were conducted on a suction caisson with a range of loading angles (El-Sherbiny et al. 2005). The results of this analysis support the use of an $\alpha$ value of 1.0 and a bearing capacity factor of 9.0 to produce unbiased predictions for capacity. More recent work (El-Sherbiny 2005) has indicated that the mobilized value for $\alpha$ may be smaller 1.0 and that for the bearing capacity factor may be higher than 9.0, but the net result for a typical geometry (length to diameter of 6 in a normally consolidated clay) is to produce the nearly the same total capacity.

While there are variations in the design practice for suction caissons, typical values in practice for α are 0.6 to 0.8, while typical values for the bearing capacity factor in practice are 7 to 9, respectively. Therefore, there is a conservative bias that is introduced with these nominal values. To quantify this bias, the suction caisson design was considered for the study spar. The side friction contributes about 50 percent of the total capacity, and the reverse end bearing contributes about 35 percent of the total capacity. As an example, if there is a bias of 1.0/0.7 on the side friction and a bias of 9.0/7.0 on the end bearing, the composite bias on the total capacity is 1.3. For typical designs, the bias will range from about 1.2 to 1.4. Coincidentally, the design bias for pile foundations on jacket platforms is also about 1.3 (Tang and Gilbert 1993).

The coefficient of variation in the ratio of measured to predicted capacity about the average on Figure 8.3 is 0.28. This value is very similar to the value of 0.3 that is typically used for pile foundations on jacket platforms (Tang and Gilbert 1993). In this study, the coefficient of variation in the vertical capacity of a suction caisson was assumed to be 0.3 based on these findings.

#### 8.2.2.3 Lower-Bound Foundation Capacity

One consequence of the relatively large median factors of safety and small coefficients of variation in the applied loads for spar foundations is that the presence of a minimum or lower-bound capacity can have a large effect on the reliability (Gilbert et al. 2005). A simple estimate of the lower-bound capacity for a suction caisson in normally consolidated clay can be obtained using the remolded strength of the clay to calculate side friction and end bearing.

The database of load tests (Figure 8.3) was used to investigate the existence of a lower-bound capacity. For each test, a predicted lower-bound capacity was calculated using the remolded undrained shear strength with an α value of 1.0 and a bearing capacity factor of 9.0. Details for how the lower-bound capacity was calculated in each test and a discussion of relevant assumptions are provided in Najjar (2005). The ratio of the calculated lower-bound capacity to the measured capacity is shown on Figure 8.4.

For all tests analyzed, the ratio of the calculated lower-bound capacity to the measured capacity is less than or equal to 1.0, providing compelling evidence for the existence of a lower-bound axial capacity. The ratio of lower-bound capacities to measured capacities ranges from 0.25 to 1.0 with an average value of 0.6.

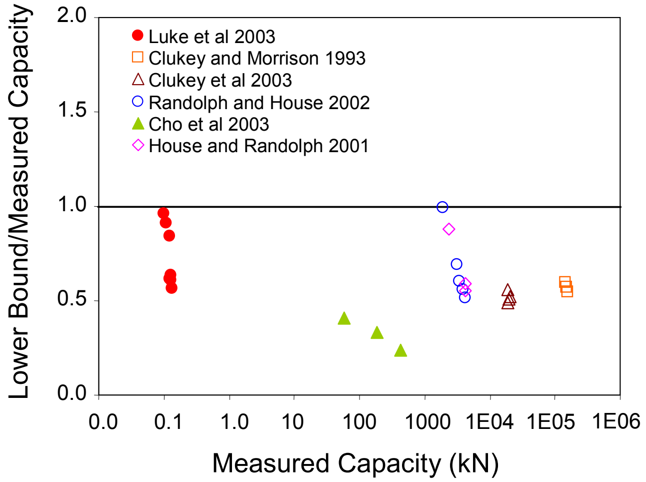

Figure 8.4: Calculated lower-bound versus measured axial capacity for suction caissons in normally consolidated clays (from Shadi 2005)

Najjar (2005) found that mixed lognormal probability distributions, as shown on Figure 8.5, adequately represented the effect of a lower bound on the uncertainty in axial capacity for driven piles. This same form of a probability distribution was used to model the lower bound capacity for the suction caisson anchors.

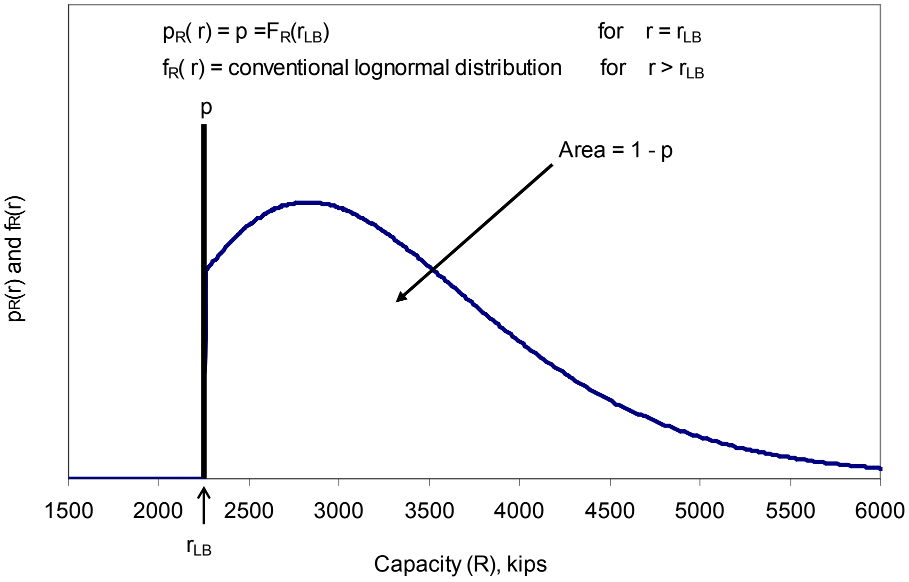

Figure 8.5: Mixed lognormal distribution for foundation capacity with a lower-bound

# 9. Reliability Framework

## 9.1 Component Reliability Calculation

When the load is denoted as S and the capacity (or strength) is denoted as R, and both are considered as random variables, the probability of failure can be calculated as (e.g., Ang and Tang 1984):

$$P_F = P(R < S) = \iint_{R<S} f_{RS}(r,s)drds \tag{9.1}$$

in which $f_{RS}(r,s)$=the joint density function of R and S. If R and S are statistically independent, Equation 9.1 becomes:

$$P_F = \int_0^{\infty} F_R(s)\, f_S(s)ds \tag{9.2}$$

where $F_R(s)$ is the cumulative distribution function of the capacity evaluated at the load s; and $f_S(s)$ is the probability density function of the load. In cases where the load and capacity are both lognormally distributed, which is a common assumption in typical reliability analyses for offshore applications (Tang and Gilbert 1993), a generalized mathematical form for the probability of failure from Equation 9.2 can be obtained:

$$\mathrm{P}\left(\mathrm{Load} > \mathrm{Capacity}\right) \cong \Phi\left(-\frac{\ln\left(\mathrm{FS}_{\mathrm{median}}\right)}{\sqrt{\delta_{\mathrm{load}}^2 + \delta_{\mathrm{capacity}}^2}}\right) = \Phi(-\beta) \tag{9.3}$$

where P(Load > Capacity) is the probability that the load exceeds the capacity in the design life (also referred to as the lifetime probability of failure), $\Phi(\cdot)$ is the normal cumulative distribution function; $\mathrm{FS}_{\mathrm{median}}$ is the median factor of safety, which is defined as the ratio of the median capacity to the median load; $\delta$ is the coefficient of variation (c.o.v.), which is defined as the standard deviation divided by the mean value for that variable; and $\beta$ is the reliability index.

The median factor of safety in Equation 9.3 can be related to the factor of safety used in design:

$$\mathrm{FS}_{\mathrm{median}} = \mathrm{FS}_{\mathrm{design}} \times \frac{\left(\dfrac{\mathrm{capacity}_{\mathrm{median}}}{\mathrm{capacity}_{\mathrm{design}}}\right)}{\left(\dfrac{\mathrm{load}_{\mathrm{median}}}{\mathrm{load}_{\mathrm{design}}}\right)} \tag{9.4}$$

where the subscript "design" indicates the value used to design the line or the foundation. The ratios of the median to design values represent biases between the median or most likely value in the design life and the value that is used in the design check with the factor of safety.

The coefficients of variation in Equation 9.3 represent uncertainty in the load and the capacity. For an offshore foundation, the uncertainty in the load is generally due to variations in the occurrence and strength of hurricanes at the platform site over the design life. The uncertainty in the capacity is due primarily to variations between the actual capacity in a storm load compared to the capacity predicted using the design method. The denominator in Equation 9.3 is referred to as the total coefficient of variation:

$$\delta_{\text{total}} = \sqrt{\delta_{\text{load}}^2 + \delta_{\text{capacity}}^2} \tag{9.5}$$

Figure 9.1 shows how the probability failure varies with the median factor of safety and the total coefficient of variation.

Tables 9.1 and 9.2 summarize the bias and c.o.v values for the mooring line and foundation, respectively. The conservative bias in the median load versus the design load is greater for these spar foundations than for a pile in a typical jacket platform, where the ratio of the median to the design load is between 0.7 and 0.8 (Tang and Gilbert 1993). This conservative bias is especially significant for the semi-taut mooring system (3,000-ft water depth) due to the effect of removing a line in establishing the design load. The loads are shared more evenly between the lines in the taut mooring systems, which minimizes the impact on each line when one line is removed. The difference between the bias values for the semi-taut versus taut mooring systems is smaller for a loop current event than that for a hurricane event. This result is mainly due to the characteristics of a loop current event in terms of loads along time histories. During a current event, loads on the most loaded mooring line (i.e., #1, compared with #8 in the hurricane case) are considered as relatively constant compared to loads in the hurricane case.

Due to the geometry of the structure and the metocean environment in deepwater, the uncertainty in the load is relatively small compare to c.o.v. values for a jacket in shallow water, which are generally between 0.3 and 0.5 (Tang and Gilbert 1993). There are several reasons for smaller uncertainty in the loads on the spar. First, the line loads are less sensitive to wave height for a spar mooring system in deep water compared to a fixed jacket in shallow water (e.g., Banon and Harding 1989). Therefore, variations in the sea states over the design life are less significant for the spar mooring system. Second, the mooring system is simpler to model than a jacket, meaning that there is less uncertainty in the loads predicted by the model. Finally, the spar line loads are dominated by pre-tension versus environmental loads; variations in the load due to variations in the sea states therefore have a smaller effect on the total line load. This effect of pre-tension is particularly significant for the taut mooring systems (6,000-ft and 10,000-ft water depths), which consequently have the smallest c.o.v. values (Tables 9.1 and 9.2).

For the loop current condition, the coefficients of variation in the foundation and line loads, regardless of the type of the mooring systems, are nearly the same. Also, the coefficients of variation in the foundation and line loads for the taut mooring systems are relatively independent of the environmental conditions. Note that the coefficient of variation in the foundation load is slightly greater than in the line load because of additional uncertainty in the soil properties.

Table 9.1: Bias and c.o.v. values for mooring line in study spar in hurricane and current conditions

| Environmental Condition | Hurricane | | | Current (Weibull) | | | Current (Type II) | | |
|---|---|---|---|---|---|---|---|---|---|
| Water Depth (ft) | 3,000 | 6,000 | 10,000 | 3,000 | 6,000 | 10,000 | 3,000 | 6,000 | 10,000 |
| $load_{median}/load_{design}$ | 0.50 | 0.73 | 0.75 | 0.70 | 0.72 | 0.72 | 0.63 | 0.69 | 0.71 |
| $capacity_{median}/capacity_{design}$ | 1.0 – 1.2 | 1.0 – 1.2 | 1.0 – 1.2 | 1.0 – 1.2 | 1.0 – 1.2 | 1.0 – 1.2 | 1.0 – 1.2 | 1.0 – 1.2 | 1.0 – 1.2 |
| $FS_{design(damage)}$ | 1.25 | 1.25-1.5 | 1.25-1.5 | 1.25 | 1.25-1.5 | 1.25-1.5 | 1.25 | 1.25-1.5 | 1.25-1.5 |
| $FS_{median}$ | 2.5 – 3 | 2 – 2.5 | 2 – 2.5 | 2 – 2.5 | 2 – 3 | 2 – 3 | 2 – 2.5 | 2 – 3 | 2 – 3 |
| $\delta_{load}$ | 0.25 | 0.13 | 0.10 | 0.09 | 0.10 | 0.09 | 0.11 | 0.12 | 0.11 |
| $\delta_{capacity}$ | 0.15 | 0.15 | 0.15 | 0.15 | 0.15 | 0.15 | 0.15 | 0.15 | 0.15 |
| $\delta_{total}$ | 0.29 | 0.20 | 0.18 | 0.18 | 0.18 | 0.18 | 0.19 | 0.19 | 0.19 |

Table 9.2: Bias and c.o.v. values for foundation for the study spar during hurricane and loop current conditions

| Environmental Condition | Hurricane | | | Current (Weibull) | | | Current (Type II) | | |
|---|---|---|---|---|---|---|---|---|---|
| Water Depth (ft) | 3,000 | 6,000 | 10,000 | 3,000 | 6,000 | 10,000 | 3,000 | 6,000 | 10,000 |
| $load_{median}/load_{design}$ | 0.41 | 0.70 | 0.71 | 0.60 | 0.69 | 0.70 | 0.59 | 0.68 | 0.69 |
| $capacity_{median}/capacity_{design}$ | 1.2 – 1.4 | 1.2 – 1.4 | 1.2 – 1.4 | 1.2 – 1.4 | 1.2 – 1.4 | 1.2 – 1.4 | 1.2 – 1.4 | 1.2 – 1.4 | 1.2 – 1.4 |
| $FS_{design(damage)}$ | 1.5 - 2.5 | 1.5 - 2.5 | 1.5 - 2.5 | 1.5 - 2.5 | 1.5 - 2.5 | 1.5 - 2.5 | 1.5 - 2.5 | 1.5 - 2.5 | 1.5 - 2.5 |
| $FS_{median}$ | 4 – 8 | 3 – 5 | 3 – 5 | 3 – 6 | 3 – 5 | 3 – 5 | 3 – 6 | 3 – 5 | 3 – 5 |
| $\delta_{load}$ | 0.32 | 0.14 | 0.11 | 0.11 | 0.10 | 0.10 | 0.14 | 0.13 | 0.13 |
| $\delta_{capacity}$ | 0.3 | 0.3 | 0.3 | 0.3 | 0.3 | 0.3 | 0.3 | 0.3 | 0.3 |
| $\delta_{total}$ | 0.44 | 0.33 | 0.32 | 0.32 | 0.32 | 0.32 | 0.33 | 0.33 | 0.33 |

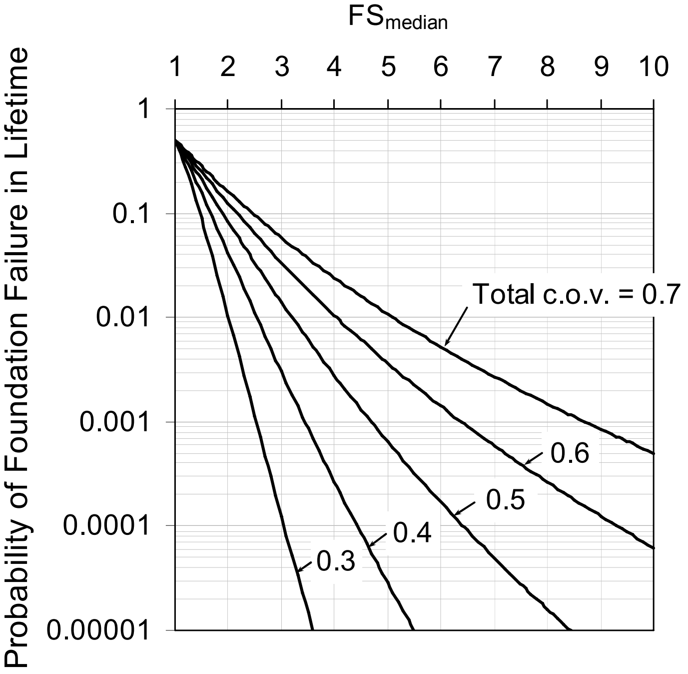

Figure 9.1: Component reliability from Equation 9.3

One additional consideration in the reliability analysis of the foundation and the chain is the effect of a minimum or lower-bound capacity. In order to account for a lower bound in the probability distribution of the capacity, numerical integration is used to evaluate Equation 9.2.

An example of the effect of a lower-bound capacity on the reliability of the foundation is shown on Figure 9.2 for the study spar in 6,000 ft water depth. The results on Figure 9.2 show the significant role that a lower-bound capacity can have on the reliability. For the average lower-bound capacity from Figure 9.2, 0.6 times the median capacity, the probability of failure is more than 1,000 times smaller with the lower-bound than without it for a design factor of safety of 1.5 in the damage case. Furthermore, for design factors of safety of 2 or 2.5 in the damage case, the probability of failure for a lower-bound capacity that is 0.6 times the median capacity is essentially zero.

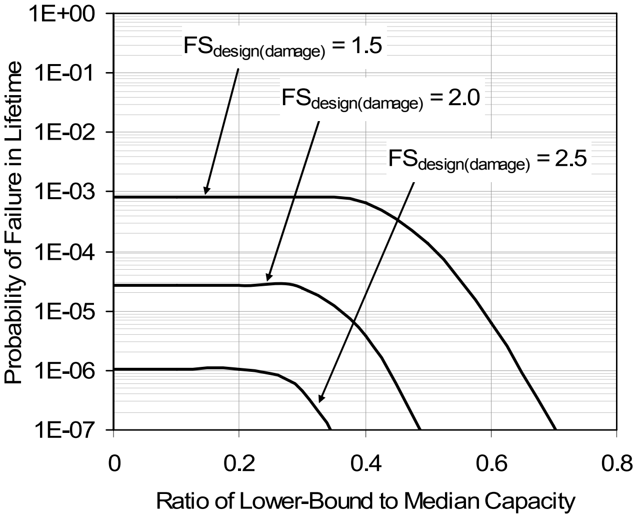

Figure 9.2: Illustration of effect of lower-bound capacity on probability of failure (study spar in 6,000 ft water depth)

## 9.2 Reliability Calculation of a Single Mooring Line System

In this section, the component reliability calculation is extended to a complete line system consisting of the three line segments (i.e., steel chain-wire rope-chain in 3,000 ft water and steel chain-polyester rope-chain in 6,000 ft and 10,000 ft water) and the corresponding anchor. The probability of failure of the line system can be expressed as follows:

$$\begin{aligned} \mathrm{P(Line)} &= \mathrm{P(Top \cup Middle \cup Bottom \cup Anchor)} \\ &= 1 - \mathrm{P(\overline{Top} \cap \overline{Middle} \cap \overline{Bottom} \cap \overline{Anchor})} \end{aligned} \tag{9.6}$$

where P(Line) is the probability of failure of a line system; P(Top), P(Middle), P(Bottom) and P(Anchor) are the probabilities of failure of the top chain, wire rope (or polyester rope), bottom chain and anchor, respectively; and $\mathrm{P(\overline{Top})}$, $\mathrm{P(\overline{Middle})}$, $\mathrm{P(\overline{Bottom})}$, and $\mathrm{P(\overline{Anchor})}$ are the reliabilities of the top chain, wire rope (or polyester rope), bottom chain and anchor, respectively.

Equation 9.6 describes the probability of a union of events, which signifies that a line breakage may occur anywhere along the mooring line. Denoting Top, Middle, Bottom and Anchor as T, M, B and A, respectively, Equation 9.6 can be calculated using probability theory as follows:

$$\begin{aligned} P(\text{Line}) = {} & [P(T\bar{M}\bar{B})+P(\bar{T}M\bar{A})+P(\bar{M}\bar{B}A)+P(\bar{T}B\bar{A})] \\ & +[P(T\bar{M}B\bar{A})+P(TM\bar{B}\bar{A})+P(\bar{T}M\bar{B}A)+P(\bar{T}\bar{M}BA)] \\ & +[P(MB\bar{A})+P(T\bar{B}A)+P(\bar{T}MB)+P(T\bar{M}A)] \\ & +P(TMBA) \end{aligned} \tag{9.7}$$

In evaluating the reliability of the system of components, the capacities of the individual components are assumed to be statistically independent.

## 9.3 System Reliability Calculation

The reliability of the mooring system is defined as the probability that the station will be maintained in full use over the 20-year design life. It is assumed that the loss of two mooring lines (either in the line itself or in the anchor) will lead to a loss of station use. Therefore, the probability for a loss of station keeping is given by

$$P(\text{Second Line Fails})=P(\text{Second Line Fails}|\text{First Line Fails})P(\text{First Line Fails}) \tag{9.8}$$

The methodology to evaluate the system reliability involves updating the distribution for $H_s$ given that one of the lines has failed during the storm. Since the maximum load is expected on line #8, the distribution for $H_s$ is updated given that line #8 has failed. Figure 9.3 shows this approach. The blue curve on Figure 9.3 is the original (before knowing that line #8 has failed) probability distribution for $H_s$. The pink curve on Figure 9.3 is the probability that line #8 will fail as a function of $H_s$. These two curves are multiplied together to produce the updated probability distribution for $H_s$ given that line #8 has failed (the green curve on Figure 9.3). Note that the updated probability distribution for $H_s$ is shifted to the right to reflect the greater likelihood that a severe storm has occurred if line #8 has failed.

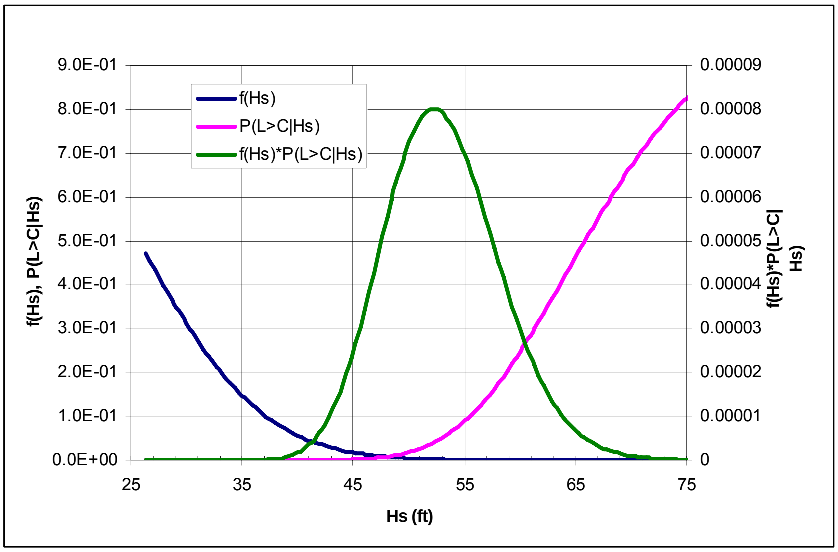

Figure 9.3: Probabilities of sea state and failure for mooring line #8

The next step in the methodology is to establish the load on the next-most heavily loaded line, which after line #8 is line #9 (Figure 9.4).

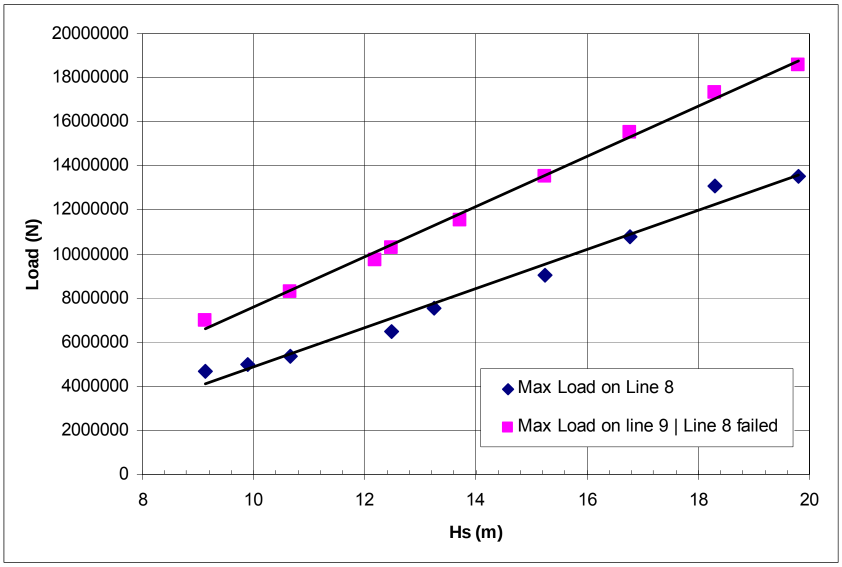

Figure 9.4: Expected maximum load at fairlead for mooring lines #8 and #9 plotted against the significant wave height

Combining the information shown in Figures 9.3 and 9.4, the updated probability distribution for the maximum load on line #9, given that line #8 has failed, can be obtained. With this updated distribution for the maximum load on line #9, the probability that line #9 fails, given that line #8 has failed, can be calculated. This probability provides an indication of the redundancy that is available in the mooring system. If it is equal to 1.0, then there is no redundancy because line #9 will fail if line #8 fails and the spar will lose station keeping.

A redundancy factor, defined as the inverse of this conditional probability, is used to measure the system redundancy. This redundancy factor is shown on Figure 9.5 for illustrative purposes (the curve labeled “System Redundancy”) as a function of the factor of safety used to design each individual mooring line. Also as an upper bound, the redundancy factor is shown on Figure 9.5 for a hypothetical system where the most heavily loaded line is duplicated, so that if one fails then a second line is still present at that location (the curve labeled “Redundancy in Line 8”). This upper bound reflects the redundancy in the system when the affect of load redistribution due to line failure is neglected.

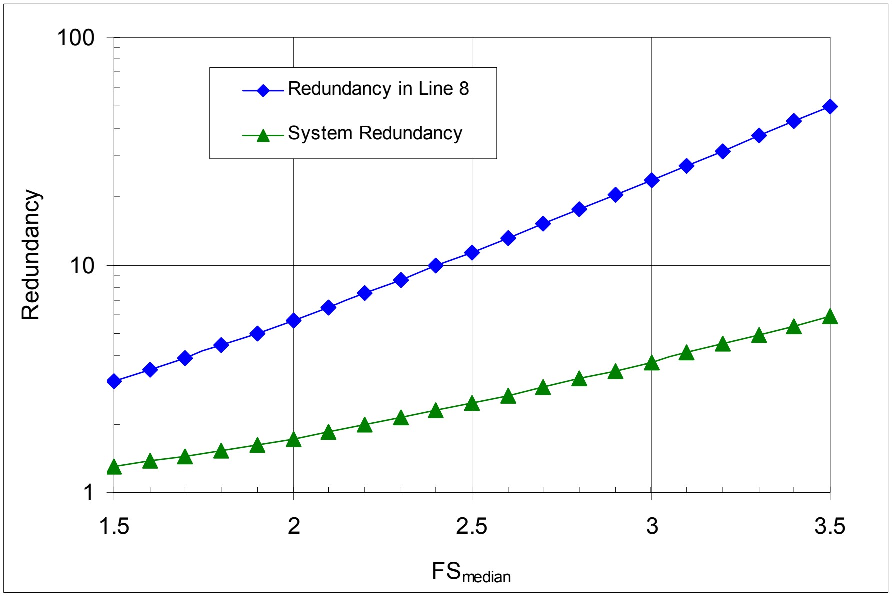

Figure 9.5: Mooring system redundancy factor

# 10. Results of Reliability Analysis for Mooring Systems in Hurricane Condition

## 10.1 Component Reliability

Figure 10.1 shows the component reliabilities for the mostly loaded mooring line for the hurricane condition. The probability that the component load will exceed the capacity of the component during a 20-year design life has a decreasing trend with greater water depth because a decrease in the total c.o.v with the water depth affects the probability. The decrease in the c.o.v arises from greater pretension and less variance in the dynamic loading in the taut systems. In the taut systems, the levels of the reliability of the upper and lower chain are almost on the same order of magnitude whereas the level is not the same in the semi-taut system. The length of the bottom chain is greater in the semi-taut system than that in the taut systems, which affects the number of links for the asymptotic extreme value problem (Type I smallest). Note that the proof load tests for the upper and bottom chains and the lower bound capacity of the foundation were considered in the calculation of the reliability as explained in the previous section.

The total line reliability including the reliability of the anchor was calculated using Equation 9.5 and is shown in Figures 10.1 and 10.2. The contribution of the anchor to the total line reliability can be found in Figure 10.2. For comparison, this anchor failure probability is more than two orders of magnitude smaller than that for any of the line components in all mooring systems. The difference between the total line and anchor probabilities becomes larger in 10,000-ft water depth. The total line reliability is affected mainly by the line components not by the anchor as shown in Figure 10.2. Note that 1) a general range of 2 to 3 for factors of safety for the case where all mooring lines are intact has been studied; 2) for Figures 10.1 and 10.2, an intact factor of safety of 2.5 for the anchor design was used; and 3) factors of safety of 1.67 (intact) and 1.25 (damaged) for the line reliability were implemented.

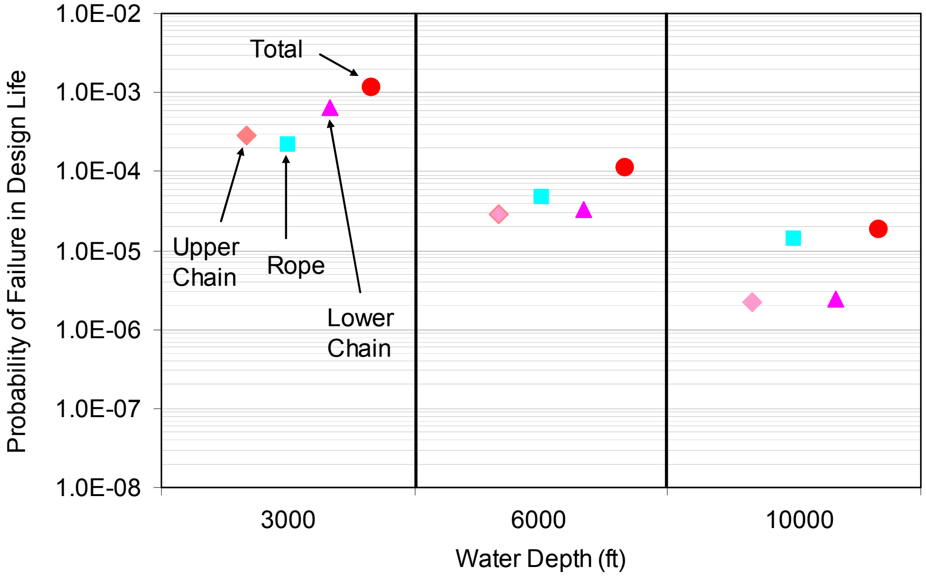

Figure 10.1: Reliability of components for mostly loaded line during a hurricane event

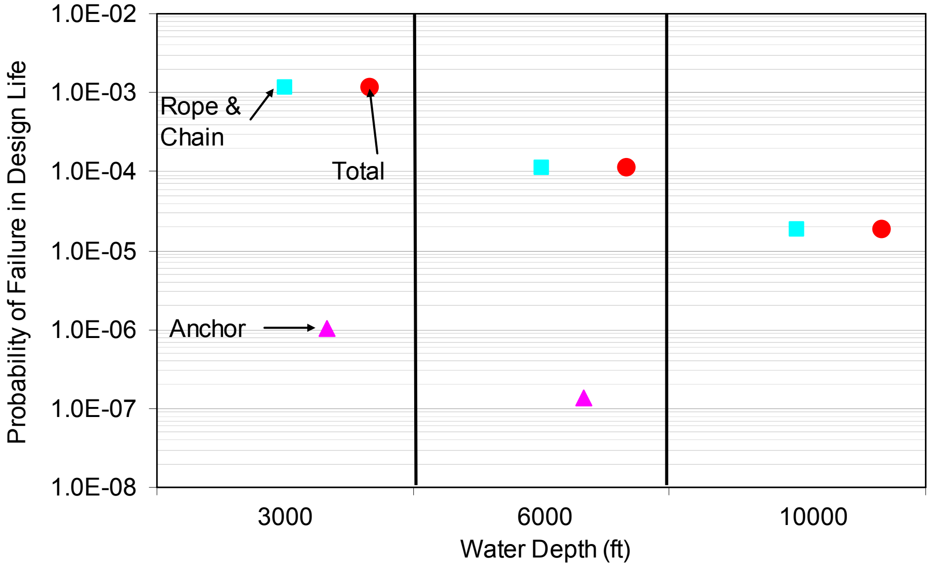

Figure 10.2: Total line reliability of mostly loaded mooring line with an intact factor of safety of 2.5 for the anchor

The component reliabilities under the loop current condition are greater than those for the hurricane condition (Figure 10.3). This result occurs because the total c.o.v. values are smaller for the loop current condition based on the Type II and Weibull distributions than for the hurricane condition. As for the hurricane condition, the levels of the reliability are not consistent among the components in the case of loop current condition.

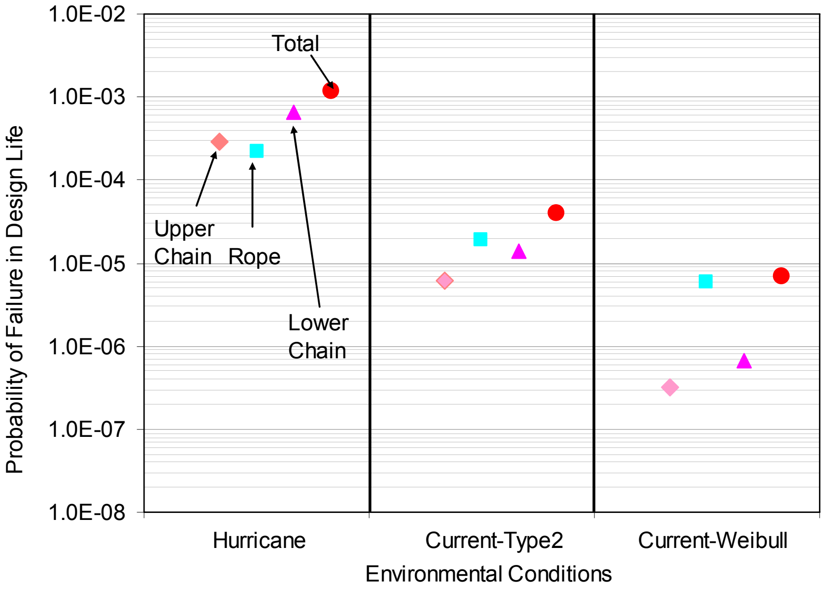

Figure 10.3: Comparison of failure probability of the components of the study spar under hurricane vs. loop current conditions in 3000-ft water depth

Figure 10.4 shows that the total line reliability of the mostly loaded line (i.e., line #8 for hurricane and line #1 for loop current) is affected mainly by the line components not by the anchor.

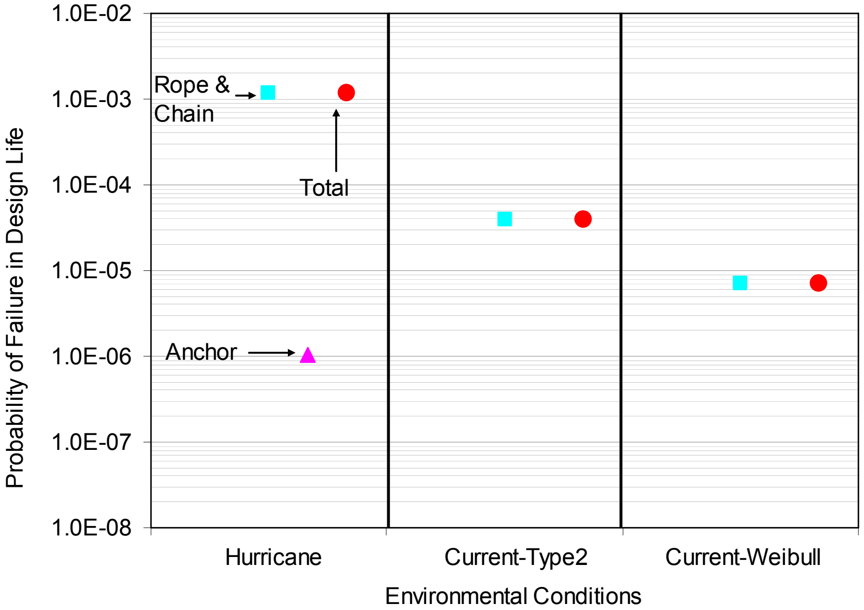

Figure 10.4: Comparison of total line and anchor reliability of the study spar under hurricane vs. loop current conditions in 3000-ft water depth

Results from reliability analyses are generally presented in terms of the annual probability of an event in offshore applications. For example, Goodwin et al. (2000) recommend a target probability of failure of $2 \times 10^{-4}$ per year for a single mooring line. The motivation for using annual probabilities is that many events in offshore applications, such as hurricanes and explosions, occur randomly with time. These annual probabilities of failure represent the rate of occurrence for high-consequence events.

In contrast to an event that is dominated by a time varying load, the uncertainty in the failure of an offshore foundation is dominated by uncertainty in the capacity. This capacity does not vary randomly with time. Therefore, it is not appropriate to consider the probability of failure as a rate of failure. If the actual capacity is higher than expected, then the annual rate of failure due to storm loading may be very small. If the actual capacity is lower than expected, then the annual rate of failure may be larger.

A more appropriate measure of the reliability for a system is the probability of failure during the lifetime of the structure. This probability was calculated in Figures 10.1 to 10.4 by considering the time-varying component of the load to determine the distribution of the maximum load applied to the foundation over its lifetime.

In order to compare failure probabilities in a design life with target probabilities of failure that are expressed as annual rates, the target probabilities should be converted to a probability of failure in a lifetime. Since it is implicit in published failure rates that event occurrences are statistically independent with time, the probability of failure in a lifetime, T, can be obtained from the following:

$$\begin{aligned} P(\text{Load} > \text{Capacity in T years}) &= 1-(1-p_{\text{annual}})^{T} \\ &\cong Tp_{\text{annual}} \end{aligned} \qquad (10.2)$$

where $p_{\text{annual}}$ is the annual failure rate.

A typical value for the target failure rate is $2\text{x}10^{-4}$ per year for a single mooring line. This value was specifically recommended by Goodwin et al. (2000), but is used widely. This target reliability level corresponds to a target probability of failure of 0.004 in a 20-year design life. Note that all of the component failure probabilities for the design spar, both for design governed by hurricanes or loop currents, are below this target value. Furthermore, the designs governed by loop currents have probabilities of failure that are several orders of magnitude below the target value for all three water depths. Also, all of the taut designs (6,000 and 10,000 foot water depths) have probabilities of failure that are several orders of magnitude below the target value for designs governed both by hurricane and loop currents.

The primary reason that the probabilities of failure are small is due to the relatively small coefficients of variation in the line load (Tables 9.1 and 9.2). A secondary reason is that the median factors of safety are relatively high, particularly for the anchors (Table 9.2). The result of these two effects is shown on Figure 10.5.

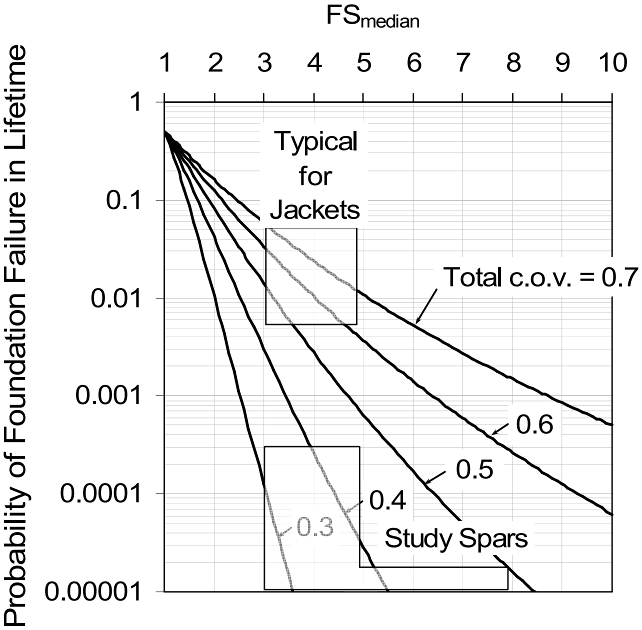

Figure 10.5: Comparison of reliability levels versus median factor of safety and total coefficient of variation

The relationship between the probability of failure for line #8 and the factor of safety for foundation in 6,000-ft water depth is shown in Figure 10.6 for hurricane loading. The motivation for considering this factor of safety is that it is not yet well-established in practice (that is a range of values are being used for the anchor factor of safety at present). The factor of safety for foundation has a great impact on the reliability of the anchor whereas the total line reliability is insensitive to this factor of safety. This insensitivity is observed because that the probability of failure of the line system (i.e., total line) is governed by the probability of failure of the line components instead of the probability of failure of the anchor. In these calculations, the lower-bound capacity was calculated to be about 0.43 times the median capacity given the geometry of the suction caisson and the soil profile.

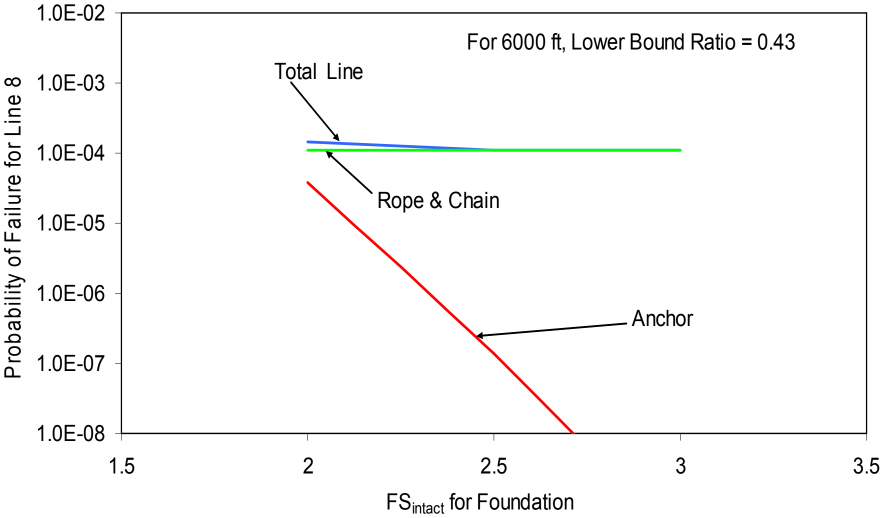

Figure 10.6: Relationship between the probabilities of failure of the total line and its components and the intact factor of safety for foundation in 6000-ft water depth with hurricane loading

The probabilities of failure of the mostly loaded line system for two additional water depths are shown in Figure 10.7. Figure 10.7 indicates that the total line reliability is relatively insensitive to the factor of safety for foundation.

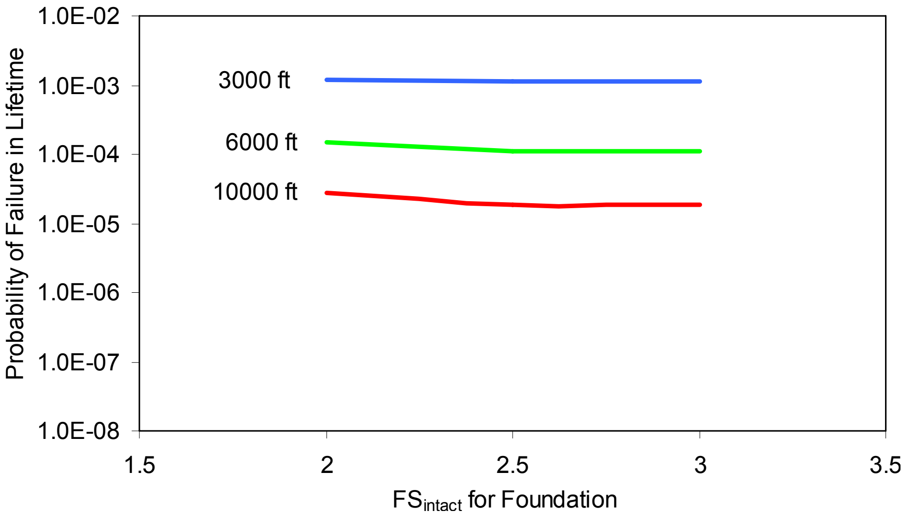

Figure 10.7: Relationship between the probability of failure of the total line and the intact factor of safety for foundation in three water depths for hurricane loading

Figure 10.8 shows the relationship between the factor of safety for the suction caisson foundation #8 and its probability of failure in three water depths for hurricane loading. The slopes of the three curves increase with increasing water depth as the total c.o.v decreases with water depth. From Equation 9.3, a reciprocal of the total c.o.v value is approximately proportional to the level of the slope of each line.

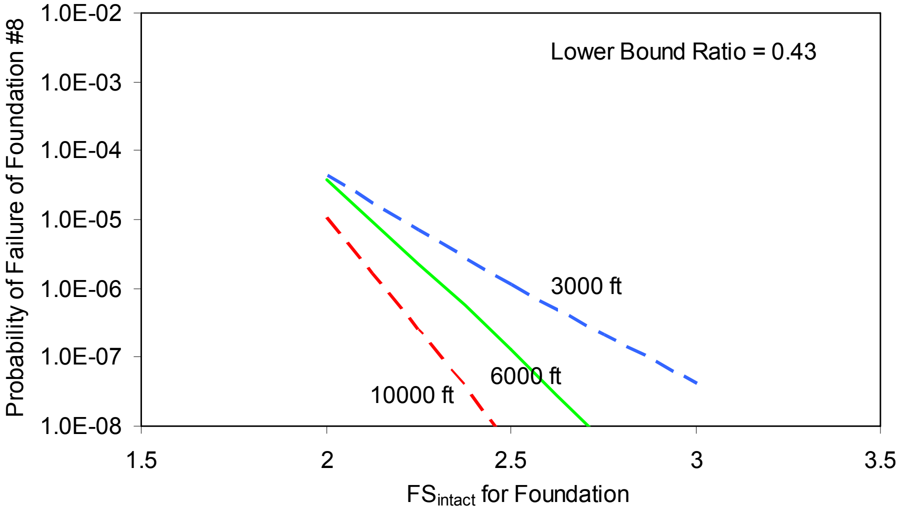

Figure 10.8: Variation in the probability of failure of foundation #8 with a lower bound ratio of 0.43 for hurricane loading

The effect of a lower bound capacity ratio of the foundation on the probability of failure is emphasized in Figure 10.9. If there is no lower bound capacity of foundation, the lower-bound to median capacity ratio of zero applies. The effect on the probability of failure of the foundation is significantly larger in the taut mooring systems than in the semi-taut mooring system. For comparison, these probabilities for the lower-bound ratio of 0.43 in 6,000 and 10,000-ft water depths are both more than two orders of magnitude smaller than that for a ratio of zero.

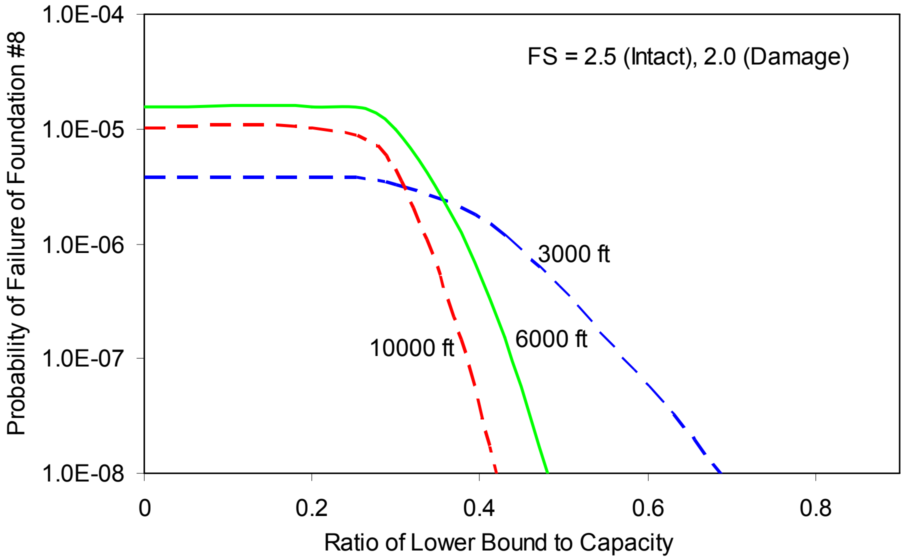

Figure 10.9 Effect of lower bound capacity of foundation on the probability of failure of foundation #8 in three water depths for the case of $FS_{intact}$=2.5 and $FS_{damage}$=2.0 for hurricane loading

One reason that the lower-bound capacity for the anchor is so significant is that the coefficient of variation in the foundation load is so small. The effect of the coefficient of variation of the line load on the reliability of the total line under the hurricane and current conditions is shown in Figure 10.10. If the line load has a coefficient of variation of smaller than about 0.25, the effect of lower-bound on the reliability of the study spar increases significantly.

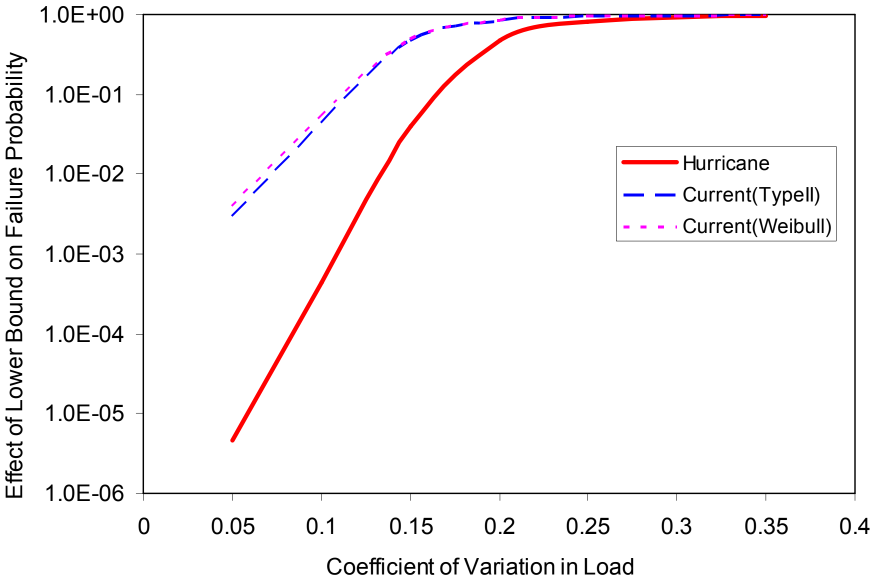

Figure 10.10: Effect of coefficient of variation in line load on reliability of total line

## 10.2 System Reliability

Figures 10.11 and 10.12 show how the probability of failure for the most heavily loaded line contributes to the total probability of failure for at least one line in the system. The reliability for a single line is dominated by that for the most heavily-loaded line.

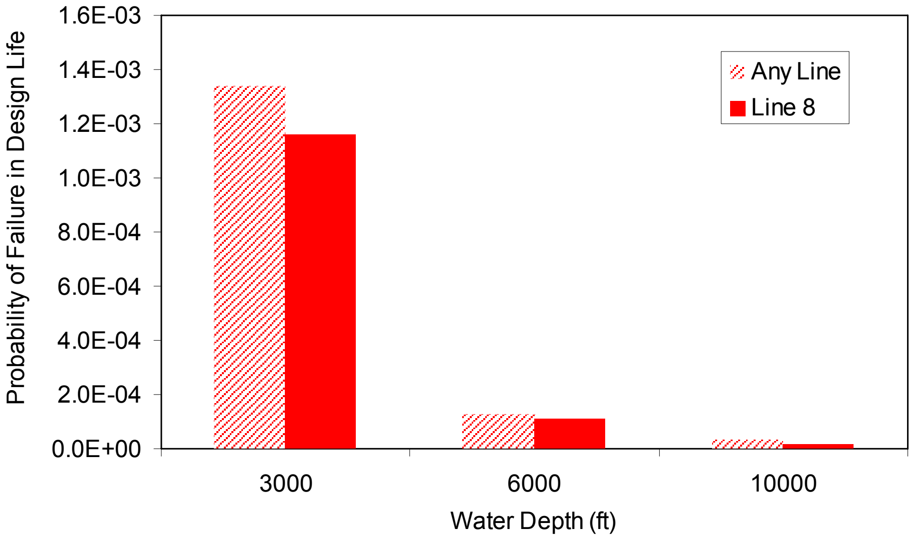

Figure 10.11: Comparisons of probabilities of failure of any line and the mostly loaded line in design life for three water depths under hurricane loading

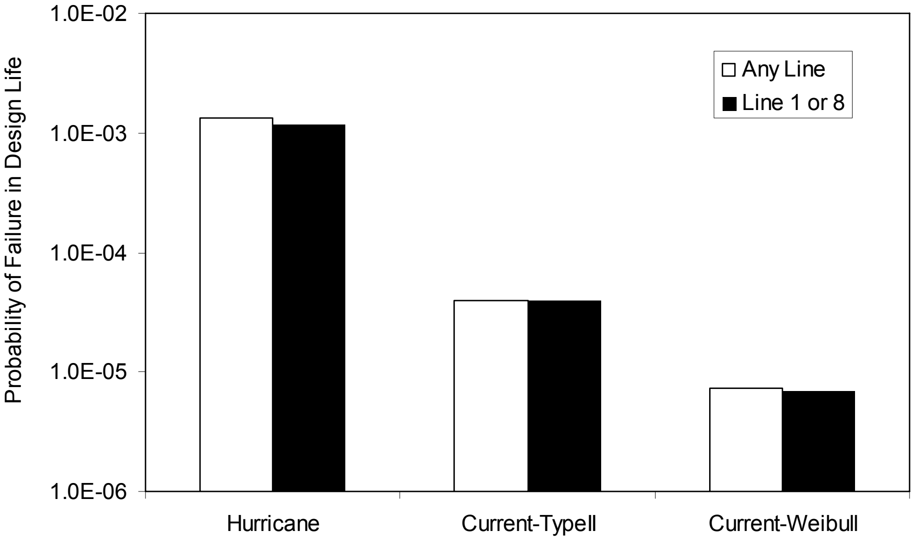

Figure 10.12: Comparisons of probabilities of failure of any line and the most heavily-loaded line in design life under hurricane versus loop current loading (note Line 8 is most heavily loaded for hurricane loading and Line 1 is most heavily loaded for loop current loading)

The conditional probabilities that the second-most loaded line (i.e., line #9) fails given that the mostly loaded line (i.e., line #8) has failed for different water depths are shown in Figure 10.13 for hurricane loading. Three assumptions were made in this analysis: 1) the line load should be large enough to fail line #8 (i.e., storm must have big waves); 2) line 9 will be the most heavily loaded line if line #8 has failed; and 3) when line #8 fails, the failure point may be anywhere along the line (including the anchor). It should be noted that the failure of the anchor is very unlikely compared to that of the line due to reasons such as the lower-bound capacity of the soil and the setup effect.

Using the conditional probability as shown in Figure 10.13, the redundancy factor can be calculated by reciprocal of the probability. The calculated redundancy factor is shown in Figures 10.14 through 10.17. For comparison, a general range for the redundancy factor for conventional steel jacket systems is between 10 and 100 (e.g., Tang and Gilbert 1993).

The smallest level of redundancy is for the semi-taut system (3,000 feet of water) under hurricane loading. In this case, the redundancy factor is about 2. For the taut system (6,000 and 10,000 feet of water), the redundancy factors are greater than 10 and similar to those for jackets. Also, the redundancy factors of loop current loading are greater than 10 for all water depths.

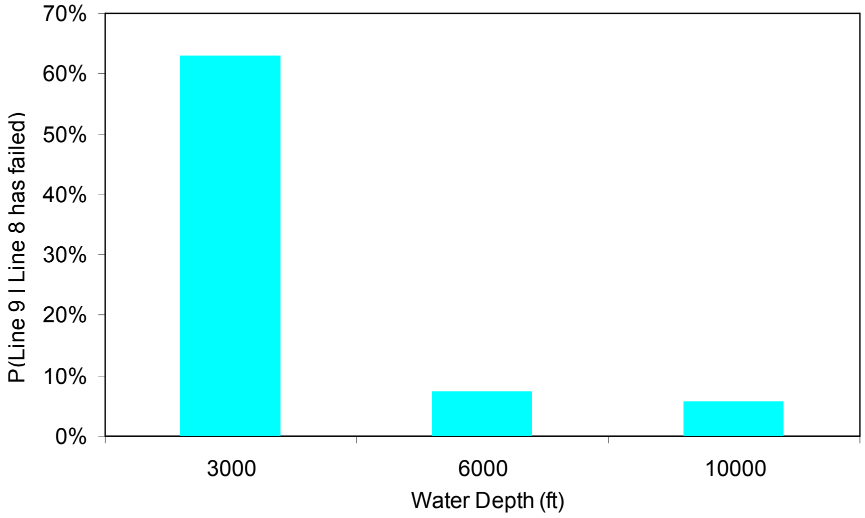

Figure 10.13: Conditional probability of failure of line #9 given that line#8 has failed at three water depths under hurricane loading

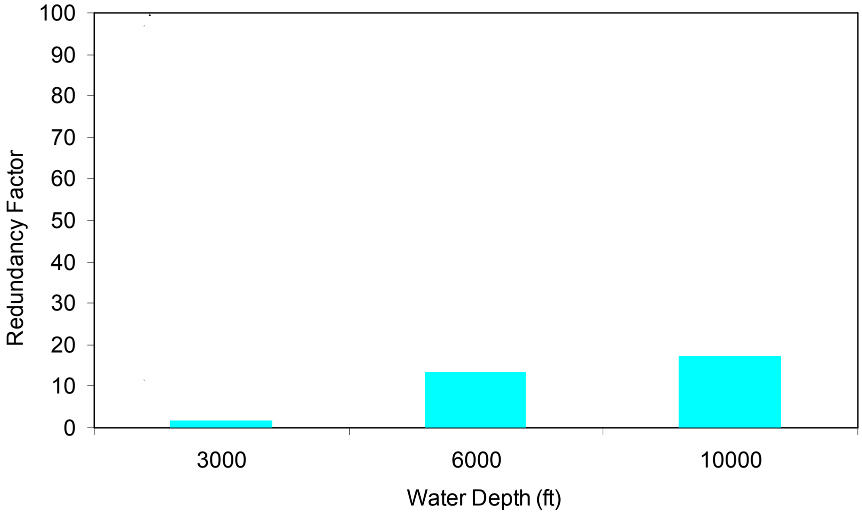

Figure 10.14: Redundancy factor for the study systems at three water depths for hurricane loading

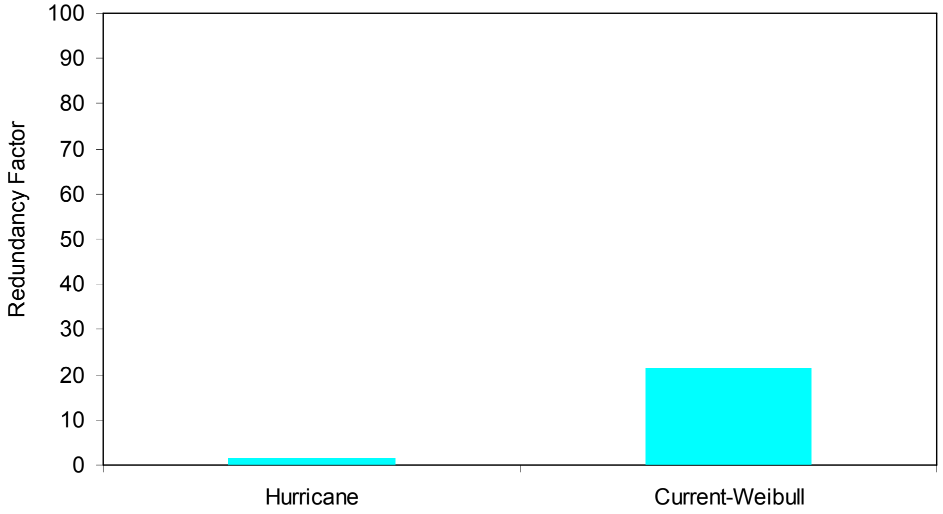

Figure 10.15: Redundancy factor for the study systems in 3000 ft of water under hurricane and current conditions

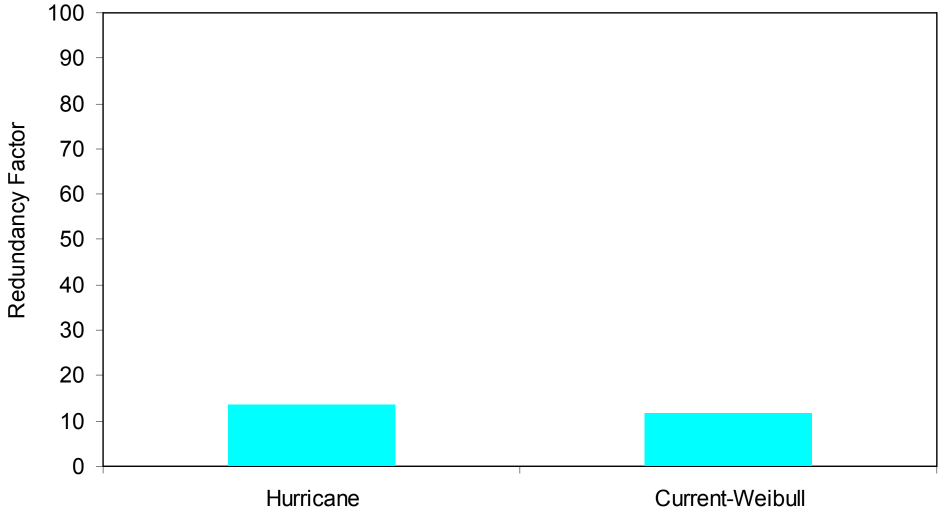

Figure 10.16: Redundancy factor for the study systems in 6000 ft of water under hurricane and current conditions

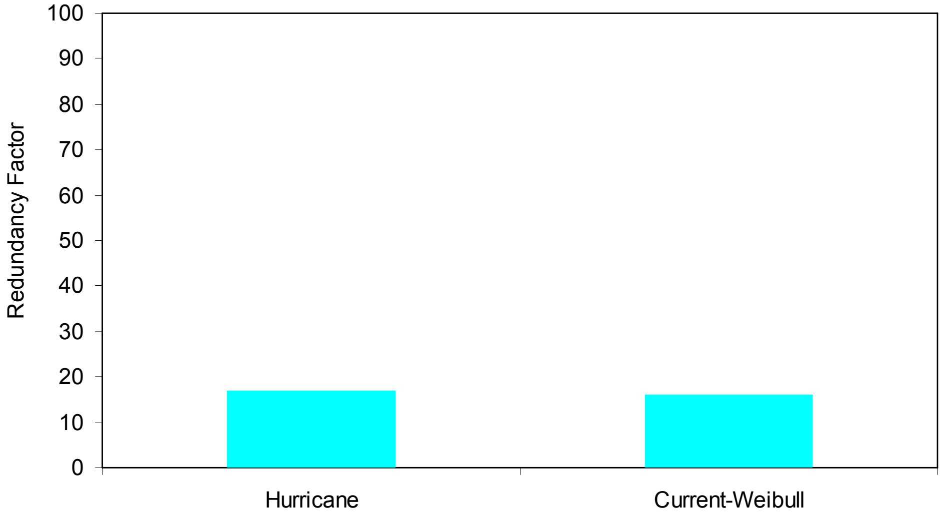

Figure 10.17: Redundancy factor for the study systems in 10000 ft of water under hurricane and current conditions

The total system reliability is shown on Figure 10.18 for the hurricane loading condition. The system reliability is greater for the taut versus the semi-taut designs.

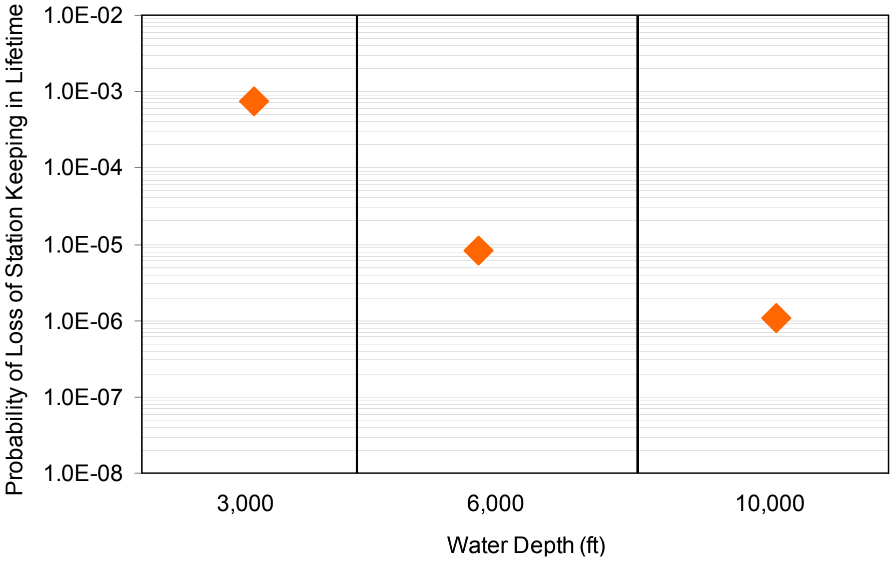

Figure 10.18: System reliability of station keeping in 20-yr design life at three water depths under hurricane loading

One final consideration with system reliability is that a single line could be missing for reasons other than failure during an extreme environmental event (e.g., maintenance or installation damage). Figure 10.19 shows how the system reliability is affected by the probability that the most heavily loaded line is missing. Assuming that the possibility that the most heavily-loaded line is missing when the extreme environmental event occurs is remote (say less than 1 in 1,000), then this possibility does not have a significant effect on the overall system reliability.

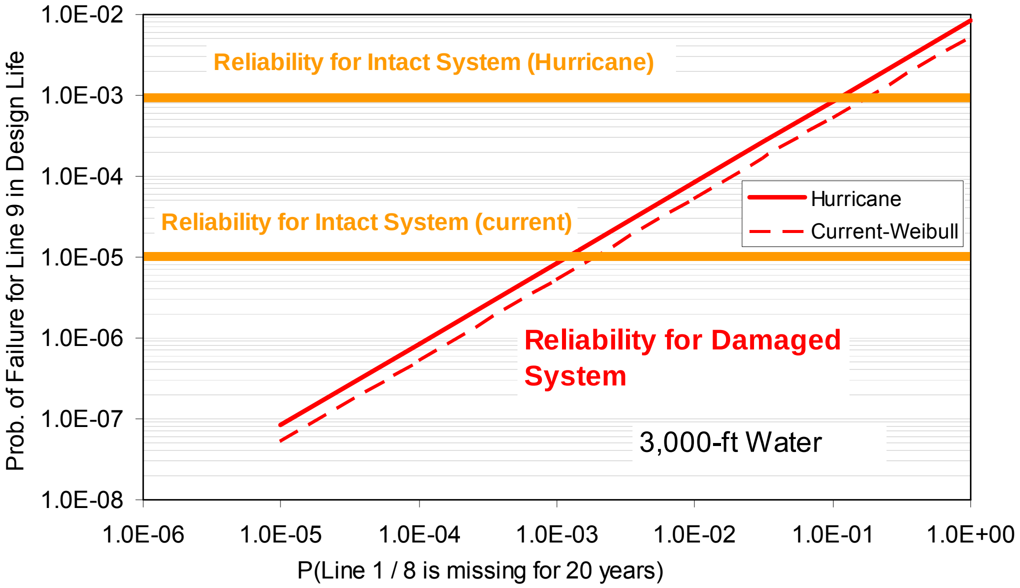

Figure 10.19: Effect of probability of one line missing on system reliability of station keeping in 20-yr design life in 3000-ft water depth under hurricane and loop current loading conditions

## 11 Conclusions

A reliability analysis for the theme spar under extreme environmental loading conditions was conducted for all three water depths. Both component and system reliabilities were addressed in this analysis. The major conclusions found in this study are:

1. Existing design guidelines provide for levels of system and component reliability against extreme loading that are above typical target levels that have been proposed by industry.
2. Levels of reliability between mooring lines and anchors are not necessarily consistent; anchors have failure probabilities that are more than an order of magnitude smaller than those for lines under extreme loading.
3. Mooring systems exhibit redundancy in that failure of the most heavily-loaded component during an extreme event does not necessarily lead to failure of the system. The redundancy is greater for the taut versus semi-taut systems and is greater during loop current events versus hurricane events.
4. The reliability for the taut systems is higher than that for the semi-taut system due to the relatively small contribution of environmental loading versus pre-tension for the taut systems.
5. The reliability for a design that is governed by loop current events is greater than one that is governed by hurricane events due to smaller uncertainty in the environmental loading conditions during loop currents compared to hurricanes.

## References

Ahilan, R. V., Cummins, I., Dyer, R. C., and Morris, W. D. M. (1996). "Reliability analysis of FPSO mooring systems and the interaction with risers." Florence, Italy, 287-302.

Ang, A. H. S., and Tang, W. H. (1975a). *Probability Concepts in Engineering Planning and Design, Volume 1 - Basic Principles*, John Wiley & Sons, Inc.

Ang, A. H. S., and Tang, W. H. (1975b). *Probability Concepts in Engineering Planning and Design, Volume 2 - Decision, Risk, and Reliability*, John Wiley & Sons, Inc.

API (1997a). "API Spec. 2F: Specification for Mooring Chain." American Petroleum Institute, 6th Ed.

API (1997b). "RP 2SK: Recommended Practice for Design and Analysis of Stationkeeping Systems for Floating Structures." American Petroleum Institute, 2nd Ed.

API (1997c). "RP 2A: Recommended Practice for Planning, Designing and Constructing Fixed Offshore Platform." American Petroleum Institute, Washington, DC.

Aubeny, C. P., Han, S., and Murff, J. D. (2003a). "Refined model for inclined load capacity of suction caissons." *Proceedings of the International Conference on Offshore Mechanics and Arctic Engineering*, OMAE03-37502, Cancun, Mexico, 883-887.

Aubeny, C. P., Han, S. W., and Murff, J. D. (2003b). "Inclined load capacity of suction caissons." *International Journal for Numerical and Analytical Methods in Geomechanics*, 27(14), 1235-1254.

Bhat, S. S., Cermelli, C. A., and Lo, K. H. (2002). "Polyester mooring for ultra-deepwater applications." *Proceedings of the International Conference on Offshore Mechanics and Arctic Engineering*, Oslo, Norway, 513-518.

Bosman, R. L. M., and Hooker, J. (1999). Elastic modulus characteristics of polyester mooring ropes. Proceedings of the Annual Offshore Technology Conference, v3, 139-143

Bruen, F. J., Gordon, R. B., and Vyas, Y. K. (1991). "RELIABILITY OF A DEEPWATER GULF OF MEXICO FPS SPREAD MOORING." *Proceedings of the International Conference on Offshore Mechanics and Arctic Engineering* 179-186.

Bush, R. B., Luo, Y., and Jack, R. L. (1992). "How chain cable reliability affects mooring system design, Part 2: A mathematical model of mooring chain strength provides a useful start toward evaluating the effects of various chain cable quality control, certification and IRM procedures." *Ocean Industry*, 27(4), 35-37.

Cao, P.M. and Zhang, J. (1997). Slow motion responses of compliant offshore structures. International Journal of Offshore and Polar Engineering 7(2), 119-126.

Chen, X.H., Zhang, J. and Ma, W. (1999). Coupled Analysis of a JIP Spar and Its Mooring System. Proceedings of the International Offshore and Polar Engineering Conference (ISOPE) Vol. I, 293-300

Chen, X.H., Zhang, J., Johnson, P. and Irani, M. (2001a). Studies on the dynamics of truncated mooring line. Proceedings of the International Offshore and Polar Engineering Conference (ISOPE), Vol.2, pp. 94-101.

Chen, X.H., Zhang, J, and Ma, W. (2001b). On dynamic coupling effects between a spar and its mooring lines. Ocean Engineering 28, pp. 863-887

Chen, X., zhang, J., Liagre, P., Niedzwecki, J. and Teigen. P. (2002) Coupled Dynamic Analysis of A Mini TLP: Comparison with Measurements. 21st International Conference on Offshore Mechanics and arctic Engineering, paper number OMAE 02-8536.

Cho, Y., Lee, T. H., Chung, E. S., and Bang, S. (2003). "Field tests on pullout loading capacity of suction piles in clay." *Proceedings of the International Conference on Offshore Mechanics and Arctic Engineering*, OMAE 2003-37016, Cancun, Mexico, 693-699.

Clukey, E. C., Aubeny, C. P., and Murff, J. D. (2003). "Comparison of analytical and centrifuge model tests for suction caissons subjected to combined loads." *Proceedings of the International Conference on Offshore Mechanics and Arctic Engineering* Cancun, Mexico, 889-894.

Clukey, E. C., and Morrison, M. J. (1993). "Centrifuge and analytical study to evaluate suction caissons for TLP applications in the Gulf of Mexico." ASCE Geotech. Special Pub. (38), Publ by ASCE, New York, NY, USA, Dallas, TX, USA, 141-156.

Clukey, E. C., and Phillips, R. (2002). "Centrifuge Model Tests to Verify Suction Caisson Capacities for Taut and Semi-Taut Legged Mooring Systems." *Proceedings of International Conference on Deepwater Offshore Technology*.

Dangayach, S. (2004). "Reliability Analysis for Mooring System of a Spar in Deepwater Gulf of Mexico." *M.S. Thesis*, The University of Texas at Austin: 85 pp.

Degenkamp, G., and Dutta, A. (1989). "Soil resistances to embedded anchor chain in soft clay." *Journal of Geotechnical Engineering*, 115(10), 1420-1438.

Del Vecchio, C.J.M. (1992). Light weight material for deep water mooring. Ph D. thesis, University of Reading, UK.

Ding, Y., Kim, M. S., Chen, X., and Zhang, J. (2003). "Coupled Aanlysis of Floating Production System." *Deepwater Mooring Systems Concepts, Design, Analysis, and Material*, Houston, TX, 152-167.

El-Sherbiny, R. M., Olson, R. E., Gilbert, R. B., and Vanka, S. K. (2005). "Capacity of Suction Caissons Under Inclined Loading in Normally Consolidated Clay." *Proceedings of Frontiers in Offshore Geotechnics*, Perth, Australia.

El-Sherbiny, R. M. (2005), “Performance of Suction Caisson Anchors in Normally Consolidated Clay”, Ph.D. dissertation, The University of Texas, Austin.

Garrett, D.L., (1982). "Dynamic analysis of slender rods." Journal of Energy Resources Technology, Transaction of ASME 104, 302-307.

Gault, J. A., and Cox, W. R. (1974). "Method for Predicting Geometry and Load Distribution in an Anchor Chain from a Single Point Mooring Buoy to a Buried Anchorage." *Offshore Technology Conference*, OTC 2062, Houston, TX, 309-318.

Gilbert, R. B., and Murff, J. D. (2001a). “Identifying uncertainties in the design of suction caisson foundations.” *Proc., Int. Conf. on Geotechnical, Geological and Geophysical Properties of Deepwater Sediments Honoring Wayne A. Dunlap*, OTRC, Houston, Tex., 231-242.

Gilbert, R. B., and Murff, J. D. (2001b). “Design methodologies and criteria for suction caissons for deepwater mooring applications.” *Workshop Report*, Offshore Technology Research Center, June.

Gilbert, R. B., Najjar, S. S., and Choi, Y. J. (2005). "Incorporating lower-bound capacities into LRFD codes for pile foundations." *Geo-Frontiers*, Austin, TX, 361-377.

Goodwin, P., Ahilan, R. V., Kavanagh, K., and Connaire, A. (1999). "Integrated Mooring and Riser Design: Reliability Analysis Methodology and Preliminary Results." *Proceedings of the Offshore Technology Conference,* OTC 10812, Houston, TX, USA, 341-353.

Goodwin, P., Ahilan, R. V., Kavanagh, K., and Connaire, A. (2000). "Integrated mooring and riser design: target reliabilities and safety factors." *Proceedings of the International Conference on Offshore Mechanics and Arctic Engineering* New Orleans, LA, USA.

House, A. R., and Randolph, M. F. (2001). "Installation and Pullout Capacity of Stiffened Suction Caissons in Cohesive Sediments." *Proceedings of International Offshore and Polar Engineering Conference*.

Larsen, K. (1996). "Efficient reliability-based design of mooring systems." *Proceedings of the International Conference on Offshore Mechanics and Arctic Engineering* 349-359.

Lee, C.H. (1995). WAMIT Theory Manual. Report No. 95-2, Massachusetts Institute of Technology, Cambridge, Massachusetts.

Luke, A. M. (2002). "Axial Capacity of Suction Caissons in Normally Consolidated Kaolinite. " *M.S. Thesis*, The University of Texas at Austin: 227 pp.

Luke, A. M., Rauch, A. F., Olson, R. E., and Meacham, E. C. (2003). "Components of Suction Caisson Capacity Measured in Axial Pullout Tests." *Proceedings of International Symposium on Deepwater Mooring Systems, Concepts, Design, Analysis, and Materials*, 1-12.

Luo, Y., and Ahilan, R. V. (1992). "Probabilistic Chain Cable Strength and Mooring Reliability." *Offshore Technology Conference*, OTC 6973, Houston, TX, 249-256.

Ma, W. and Webster, W.C. (1994). An Analytical Approach to cable Dynamics: Theory and User Manual. SEA GRANT PROJECT R/OE-26.

Murff, J. D., and Hamilton, J. M. (1993). "P-Ultimate for Undrained Analysis of Laterally Loaded Piles." *J. Geotech. Engrg.*, ASCE, 119(1), 91-107

Najjar, S. S. (2005). "The Importance of Lower-Bound Capacities in Geotechnical Reliability Assessments." *Ph.D. Dissertation*, The University of Texas at Austin: 347 pp.

Neubecker, S. R., and Randolph, M. F. (1995). "Performance of Embedded Anchor Chains and Consequences for Anchor Design." *Offshore Technology Conference*, OTC 7712, Houston, TX, 191-200.

Petruska, D., Geyer, J., Macon, R., Craig, M., Ran, A., and Schulz, N. (2005). "Polyester mooring for the Mad Dog spar-design issues and other considerations." *Ocean Engineering*, 32(7 SPEC ISS), 767-782.

Randolph, M. F., and House, A. R. (2002). "Analysis of Suction Caisson Capacity in Clay." Houston, TX, United States, 2145-2155.

Reese, L. C. (1973). "A Design Method for an Anchor Pile in a Mooring System." *Offshore Technology Conference*, OTC 1745, Houston, TX, 209-218.

Sarpkaya, T. and Isaacson, M., (1981). Mechanics of Wave Forces on Offshore Structures. Van Nostrand Reinhold Company Inc., New York.

Smith, D. W. (2005), personal communication on DeepStar CTR 4404 project.

Snell, R., Ahilan, R. B. and Versavel, T. (1999), "Reliability of Mooring Systems: Application to Polyester Moorings," *Proceedings of Annual Offshore Technology Conference*, OTC 10777, Houston, TX, USA, 125-130.

Tang, W. H., and Gilbert, R. B. (1993). "Case study of offshore pile system reliability." *Proceedings of Annual Offshore Technology Conference*, OTC 7196, Houston, TX, USA, 677-683.

Tuah, H. and Hudspeth, R.T. (1982). Comparison of numerical random sea simulations, Journal of Waterway, Port, Coastal and Ocean Divisions, ASCE, 108, (WW4), Proceedings Paper 17488, pp. 569-584

Vivatrat, V., Valent, P. J., and Ponterio, A. A. (1982). "The Influence of Chain Friction on Anchor Pile Design." *Offshore Technology Conference*, OTC 4178, Houston, TX, 153-163.

Ward, E. G. (2005), personal communication on loop current characteristics and models.

Winterstein, S. R. and Kumar, S. (1995). “Reliability of Floating Structures: Extreme Response and Load Factor Design.” *Proc., Offshore Technology Conf.*, OTC 7758, Houston, Tex.,569~578

Zhang, J., Chen, L., Ye, M. and Randall, R.E. 1996. Hybrid Wave Model for Unidirectional Irregular Waves. Part I. Theory and Numerical Scheme, Applied Ocean Research, Vol. 18, 77-92.

Zhang, J., Yang, J., Prislin, I., Wen, J., and Hong, K. 1999. Deterministic Wave Model for Short Crested Ocean Waves, Part I. Theory and Numerical Scheme. applied ocean Research, Vol. 21, 167-188.

## Unit Conversion Table

| **Conversion Factors for Different Units of Measurements** | | | |
|---|---|---|---|
| **Quantity** | **SI Unit** | **Other Unit** | **Inverse Factor** |
| Length | 1m | 3.281 feet (ft) | 0.3048 m |
| | 1 km | 0.540 nautical miles | 1.852 km |
| | 1 km | 0.6213712 mile | 1.609344 km |
| Area | 1 m$^2$ | 10.764 ft$^2$ | 0.0929m$^2$ |
| Volume | 1 m$^3$ | 35.315 ft$^3$ | 0.0283 m$^3$ |
| | 1 m$^3$ | 264.2 gallon (US) | 0.00379 m$^3$ |
| | 1 m$^3$ | 220.0 gallon (UK) | 0.00455 m$^3$ |
| | 1 m$^3$ | 6.29 barrel (US Petroleum) | 0.1589 m$^3$ |
| Velocity | 1 m/s | 3.281 ft/s | 0.305 m/s |
| | 1 m/s | 1.943 knot | 0.515 m/s |
| | 1 m/s | 2.2369 mph | 0.44704 m/s |
| | 1 km/hr | 0.62137 mph | 1.6093 km/hr |
| Mass | 1 kg | 2.205 pound | 0.454 kg |
| | 1 Mg | 0.984 ton (long) | 1.016 Mg |
| | 1 Mg | 1 tonne (metric) | 1 Mg |
| Force | 1 N | 0.225 pound force | 4.448 N |
| | 1 MN | 100.4 ton force | 9964 N |
| | 1 MN | 224.81 kip | 4448 N |
| | 1 kg-force | 0.0022046 kip | 453.592 kg-force |
| Pressure | 1 N/m$^2$ | 0.000145 psi | 6895 N/m$^2$ |
| | 1 kg-force/cm$^2$ | 0.01422 ksi | 70.307 kg-force/cm$^2$ |
| | 1 MN/m$^2$ | 20.885 kip/ft$^2$ | 47880 N/m$^2$ |
| Energy | 1 J | 0.738 foot pounds | 1.356 J |
| Power | 1 W | 0.00134 horsepower | 745.7 W |
| Temperature | 0$^0$ Celsius | 32$^0$ Fahrenheit | -17.78$^0$ Celsius |
| Frequency | 1 cycle/s | 1 hertz | 1 cycle/second |
| Flow Rates | 1 m$^3$/day | 6.289 barrel/day | 0.1589 m$^3$/day |
| | 1 m$^3$/day | 35.3146 ft$^3$/day | 0.0283 m$^3$/day |
| Density | 1 g/cm$^3$ | 0.578 oz./inch$^3$ | 1.73 g/cm$^3$ |